Decay spectroscopy of nuclei near the proton drip line and the N=82 shell closure

Thesis submitted in accordance with the requirements of the University of Liverpool for the degree of Doctor in Philosophy

by

Laura Bianco

Oliver Lodge Laboratory

November 2008

Abstract

In this thesis the outcomes of several experiments performed at the Accelerator Laboratory at the University of Jyväskylä, Finland are presented. The nuclide ^{161}Os has been observed through its α decay for the first time. The measured α-decay energy and half-life were 6890 $\pm$ 12 keV and 570 $\pm$ 50 μs, respectively. This α decay populated ^{157}W, which decayed by β-particle emission. The half-life of the β decay was inferred to be 280 $\pm$ 25 ms. The reduced α-decay width measured for ^{161}Os is compatible with s-wave α-particle emission, implying that its ground state is also a $\nu f_{7/2}$ state. Few counts at excitation energy of 318 $\pm$ 30 keV in ^{157}W have been identified and assigned as the fine structure in ^{161}Os α decay populating the $9/2^-$ state in ^{157}W, confirming the $\nu f_{7/2}$ ground state assignment. The α decay of ^{159}Re has been observed for the first time. The α decay emanates from the proton-emitting $\pi h_{11/2}$ state in ^{159}Re with an energy of E_α = 6776 $\pm$ 26 keV and a branching ratio of 7.5 $\pm$ 3.5 %. This α decay populates a state in the closed neutron shell nucleus ^{155}Ta, which decays by emitting 1444 $\pm$ 15 keV protons with a half-life of $2.9^{+1.5}_{-1.1}$ ms. These values are consistent with the emission of the proton from a $\pi h_{11/2}$ orbital. In a separate experiment at the Accelerator Laboratory at the University of Jyväskylä the nuclides $^{168-170}$Pt were produced and prompt γ rays were detected at the target position providing a selection criterion for the $^{168-170}$Pt nuclei. This technique enables the problem of the background from higher-energy α decays in the spectrum to be circumvented. The α-decay branching ratios of $^{164-166}$Os were deduced from the fraction of selected $^{168-170}$Pt nuclei correlated with α decays of $^{164-166}$Os. The resulting branching ratios agree with the literature values but can have improved precision.

Acknowledgements

I would like to thank all the people that helped me feeling welcome during the last three and a half years in Britain.

First of all I would like to thank my supervisor Prof. Robert Page for being a valuable and supportive guide. Many thanks to Dr. Dave Joss for collaborating and sharing his enthusiasm. A big thank to Prof. John Simpson for the encouragement and advice. Prof. Rodi Herzberg, Paul Nolan and Eddie Paul for sharing with me and other students their kowledge. Thanks to all the collaborators in Jyväskylä, in Daresbury and to A.Andreyev for letting me participate and lern from many of his experiments.

I would like to thank all the people at the Physics department in Liverpool, all the students and a special thank to Danielle, Jimmy, Ben and Alex. Thanks to all the post-doc and in particular to Beatrice, Tuomas, Janne, Dan and Marcus for reading this thesis.

Contents

List of Figures

List of Tables

Chapter 1

Introduction

The limit of nuclear existence is one of the major topics being addressed in nuclear physics. For proton-rich nuclei, the proton drip line defines the limit beyond which the nucleus will no longer bind extra protons and represents a perfect region to study exotic systems and test current theories and aspects of nuclear structure. By measuring the Q value is possible to test mass models and gain information about the location of the proton drip line, and hence the experimental limit to nuclear existence, and by measuring the ground or isomeric state decays one can assign single-particle levels.

This thesis focuses on nuclei near the intersection of the proton drip line and the N = 82 shell closure. In the last couple of decades a lot of effort has been invested in mapping the region of proton radioactivity in between the Z = 50 and Z = 82 shell closures (see fig. 1.1). In particular in the early 1990s the combination of recoil separators and double sided silicon strip detectors at their focal planes represented a new powerful tool for the discovery of new proton emitters and vigorous research programmes were established at Daresbury laboratory, Oak Ridge National Laboratory and Argonne National Laboratory. Up to date around thirty nuclei have been identified that emit protons from their ground state and 20 from long-lived excited states [Bla08].

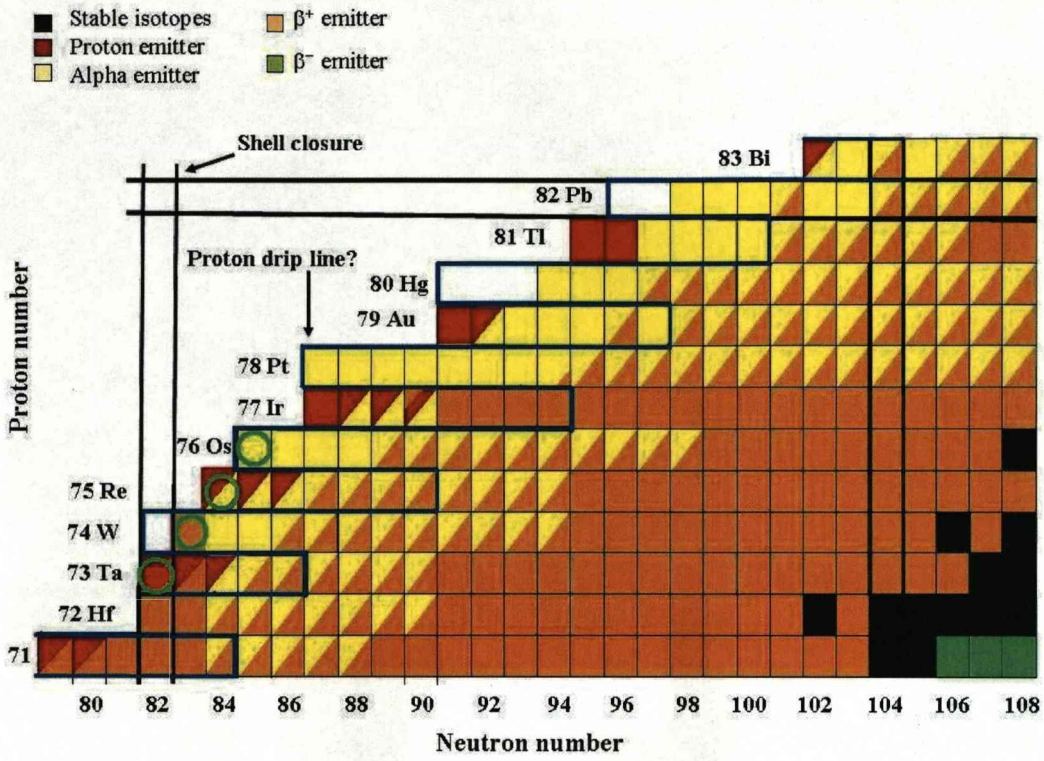

Figure 1.1: Region of the chart of nuclide studied in this work. The shell closure at Z = 82 and N = 82 and the neutron mid-shell at N = 104 are indicated by the bold lines, while the proton drip line is shown in blue. The nuclei studied in the work are highlighted with green circles.

More experimental data are needed for regions near the drip lines since it is here that nuclear models can be tested at their extremes. In particular the nuclear shell model, which is one of the most successful and widely used models to describe nuclear structure, predicts a sequence of single particle orbitals that is well reproduced near the valley of stability, but becomes less accurate when moving from stable to exotic nuclei. The orbitals relevant for the region studied in this work can bee seen in Fig. 1.2.

In this extreme region new factors may have to be included in the model to reproduce the observed single particle levels, such as the spin-isospin dependent

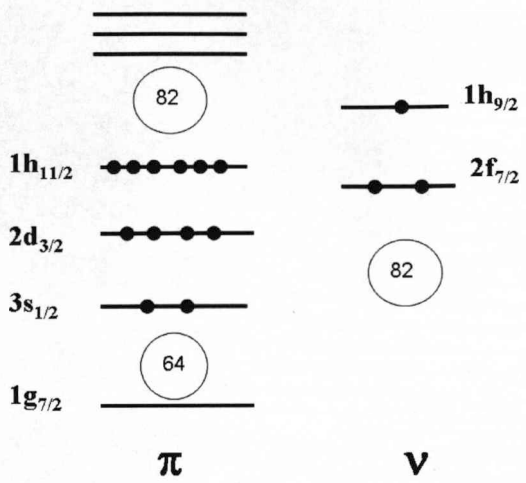

Figure 1.2: Energy levels of the orbitals in the ^{161}Os case. Particulary relevant for nuclei studied in this work is the variation in the energy gaps between orbitals as the neutron and proton numbers change. For N = 85 and N = 83 isotones interactions between nucleons occupying the $h_{11/2}$ and $h_{9/2}$ orbitals would lower the energies of these orbitals.

part of the nucleon-nucleon interaction. Different nuclear decay modes are a powerful tool to investigate the structure of nuclei far from the valley of beta stability with extreme proton or neutron numbers. Particles and radiations emitted after a nucleus has been excited can be detected with the appropriate device allowing important spectroscopic information to be extracted.

The theoretical background necessary to understand the data analysed in this work is presented in Chapter 2. The experimental data were collected from several experiments performed at the Accelerator Laboratory of the University of Jyväskylä in Finland and the general technique and experimental set up are described in Chapter 3, together with the specific data analysis procedures described

in Chapter 4. In Chapter 5 ground-state structures of the new nuclides ^{161}Os and ^{157}W are described together with α-decay fine structure in ^{161}Os and Hartree-Fock calculations, where the inclusion of a tensor component better reproduces experimental energy difference trends for the N = 83 and N = 85 isotones. ^{159}Re was previously known only to proton decay [DJoss06]. In Chapter 6 the first observation of the α decay of ^{159}Re is presented as well as the subsequent proton emission from ^{155}Ta. All nuclei described in these chapters have been considered to be spherical, since they lie very close to the N = 82 shell closure and calculations by Möller and Nix [Moll95] indicate a negligible ($\epsilon_2 < 0.1$) deformation for ^{161}Os, ^{159}Re and ^{155}Ta. Chapter 7 describes branching ratio measurements for Os isotopes using a new γ-ray tagging technique and Chapter 8 presents a summary of the outcomes of this work and some prospects for the future.

Chapter 2

Physics background

2.1 Shell model

Nucleons in the nucleus interact with each other through many-body nucleon nucleon forces. These forces do not have a complete theoretical basis and in the nuclear shell model are described by a mean-field approximation in which each nucleon is seen as an independent particle moving in a central potential created by all the other nucleons. The application of the shell model was extended from atomic physics, with the assumption that nucleons are free from collision, allowing them to move in almost unperturbed single-particle orbits within the nucleus, and being fermions they will occupy orbits according to the Pauli principle. The system can be described by an Hamiltonian H defined as

$$H = \sum_{i=1}^{A} -\frac{\hbar^2}{2m}\nabla_i^2 + \sum_{ij}^{A} V\left(r_{ij}\right), \tag{2.1}$$

where the first term represents the sum of the individual nucleon kinetic energies and the second term represents the potential felt by all of the nucleons.

This may be rewritten as the sum of a central and a residual interaction parts,

so that one can treat the two parts separately:

$$H = \sum_{i=1}^{A} \left[-\frac{\hbar^2}{2m} \nabla_i^2 + V_i(r_i) \right] + \left[\sum_{ij} v(r_{ij}) - \sum_i V_i(r_i) \right], \tag{2.2}$$

where the first term is the independent single particle Hamiltonian, $V_i(r_i)$ is the average potential and $v(r_{ij})$ is the interaction potential between two nucleons. The assumption made by the shell model is that the central interaction is larger than the residual interaction and therefore as a first approximation the latter can be neglected.

The problem of choosing the form of the potential is a crucial one and several answers have been given through the years (see fig. 2.1), starting from a simple square well, to the harmonic oscillator potential to the more realistic "'Woods-Saxon"' potential [Woods54] which is described as:

$$V_{woods-saxon}(r) = \frac{-V_0}{1 + exp[(r - R_0)/a]}, \tag{2.3}$$

where V_0~50 MeV, R_0~1.2 $A^{1/3}$ fm and a~0.6 fm.

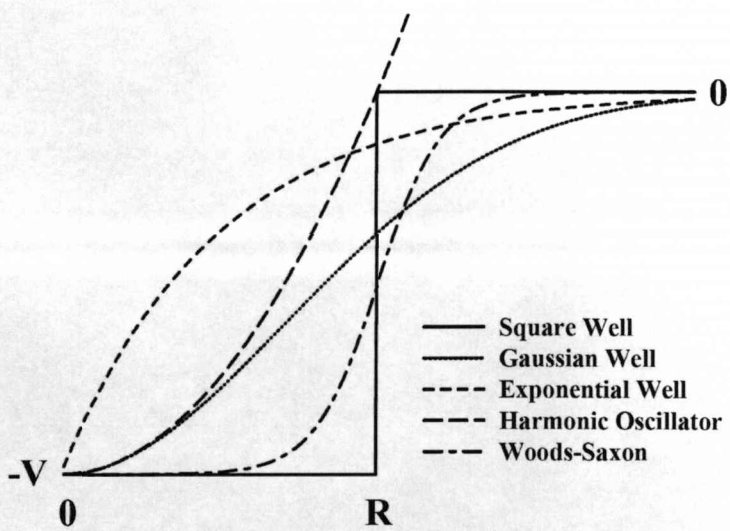

Figure 2.1: Several potentials used to approximate the nuclear potential.

The Schrödinger equation associated with a particle in the Woods-Saxon potential is:

$$\left[\frac{-\hbar^2}{2M}\nabla^2 + V_{ws}(r)\right]\Psi = E\Psi, \tag{2.4}$$

It was realized that when solving eq. 2.4 the calculated single particle levels did not represent the experimental levels and the observed magic numbers.

Mayer [Mayer49] and Haxel, Jensen and Suess [Haxel49] pointed out that the average field felt by each individual nucleon should contain a spin-orbit term. The spin-orbit term includes a scalar product of the orbital angular momentum l and the intrinsic spin operator s. Application of the Schrödinger equation plus the spin-orbit coupling yields the correct single particle energies and the observed magic numbers, see Fig.2.2. The effect of the spin-orbit coupling is also to break the degeneracy in the j= $l\pm1/2$ orbitals. In particular the potential is more attractive for the parallel j = l+1/2 orientation, relative to the anti-parallel situation. The result is a lowering of the j = l+1/2 orbital for a given large N shell, which is lowered into the orbits of the N-1 shell, accounting for the shell-closure numbers at 28, 50, 82, 126.

2.1.1 Pairing

In the shell model the central interaction was considered the most important, being much larger than the residual interactions. This approximation has several limitations; for example it does not take into account a major component of the residual interaction caused by the pairing force.

The pairing interaction is defined to be an attractive interaction acting on two identical nucleons in the same j orbit in a total angular momentum $I^\pi = 0^+$ state. The maximum effect of this interaction would manifest at the greatest spatial overlap between two nucleons, however this is forbidden by the Pauli exclusion principle, which forbids two nucleon from occupying the same orbit.

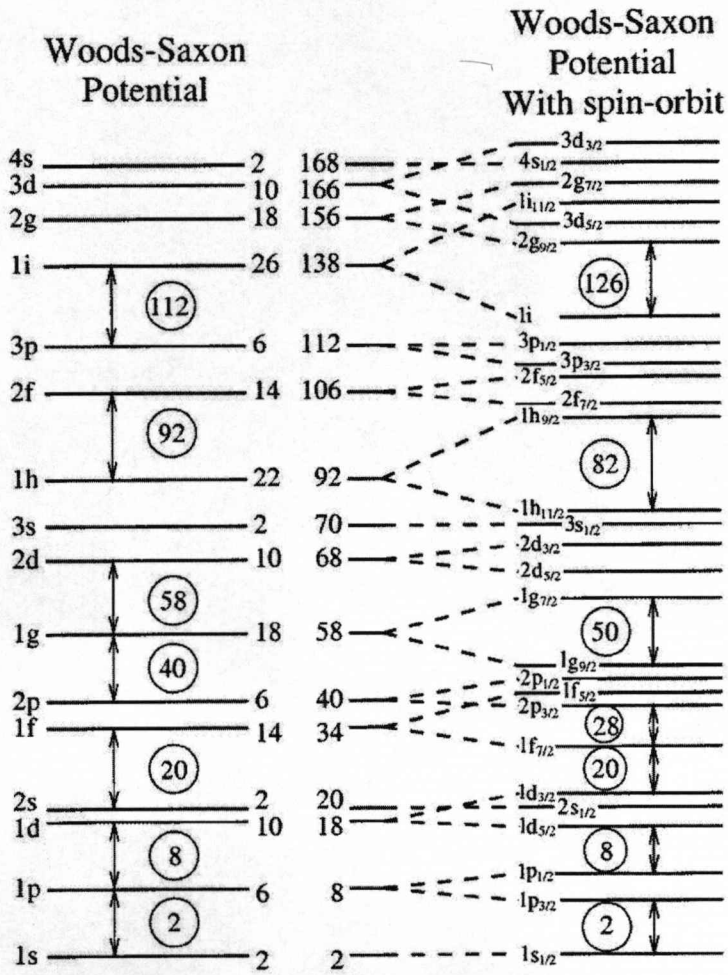

Figure 2.2: Energy levels calculated using the Woods-Saxon potential (left) and the effect of the spin-orbit interaction (right) in the level ordering. Figure taken from Ref.[Kran88]

The next configuration which generates the greatest overlap is found when the two nucleons occupy so called time reversed orbits. This are orbits for which the nucleons have the same n, l and j quantum numbers, with m quantum numbers equal but opposite in sign. When a pair of nucleons collide they will occupy new time reversal orbits of different energy, and therefore this scattering is possible

only where there are free orbitals, which are near to the Fermi level. This leads to a smearing of the Fermi surface. The energy required to break a pair, the pair gap parameter, denoted by Δ, is large enought to justify the approximation that two paired nucleons are inert. Evidence for the concept of pairing [Cast00] exists in a number of experimental observables: the ground states of all even-even nuclei have spin $0\hbar$ because the nucleons are coupled pairwise so that their angular momenta cancel, even-even nuclei are more bound. Furthermore experimentally determined moments of inertia are less than the rigid body values, suggesting a superfluid behaviour of the nucleus.

2.1.2 Coupling rules

The total spin of the nucleus is defined as the superposition of the total spin **J=L+S** of all nucleons:

$$J = \sum_{i=1}^{A} j_i \tag{2.5}$$

Coupled nucleons do not contribute to generate total spin J, forming a J_{coup}=0 state. A shell j can contain (2j+1) particles that constitute a fully coupled shell thus again forming a J_{coup}=0 state. The only remaining "valence" nucleons will determine the actual nuclear spin J. One can distinguish between several situations in order to obtain the total nuclear spin J.

Even Z even N nuclei: neutrons and protons independently of each other couple their angular momentum to zero. In all the other cases one has to consider how the valence nucleons spin couple together. For odd N and even Z, protons couple their spins to zero, in nearly all cases the neutrons in the incompletely filled j levels couple their angular momenta to a resulting total J which is equal to j. The same rule applies for even N and odd Z with the words neutron and proton interchanged. For odd-odd nuclei many cases are covered by Nordheim's rule [Nord50], who hypothesised that the ground state spins of many odd-odd

nuclei could be accounted for on the basis of a j - j coupling model plus certain simple rules governing the angular momentum coupling of the last odd proton and neutron [Gall58]. The hypotheses were:

- if for one of the two odd nucleons spin and angular momentum are parallel, and for the other antiparallel, i.e.:
  if $j_p = l_p \pm 1/2$ and $j_n = l_n \mp 1/2$ then $I = |j_p - j_n|$ the total ground state spin is the lowest possible one, the rule is often referred to as the "Nordheim strong rule".

- if for both odd nucleons spin and orbital angular momenta are either both parallel or both antiparallel, i.e.:
  if $j_p = l_p \pm 1/2$ and $j_n = l_n \pm 1/2$ then $I = j_p + j_n$ the total angular momenta j_p and j_n tend to add, although not necessarily to the highest possible value $J = j_p + j_n$. This rule is often referred to as the "Nordheim weak rule".

The weak rule appears to fail in several experimental cases [Gall58] where the tendency to couple the orbital angular momenta antiparallel is stronger than would be expected on the basis of the simple shell model.

2.2 Stability

The nuclear limit of stability is one of the main subjects investigated by contemporary nuclear structure. There are 275 known stable nuclei, with 166 even-even, 105 odd-even and 4 odd-odd. Surrounding the stable nuclei there are unstable nuclei that spontaneously break up with a certain half-life. According to the the semi-empirical mass formula developed by C.F. von Weizsäcker [Wei35], the binding energy of a nucleus of mass number A, with Z protons and N neutrons is:

$$B(Z,A) = a_{vol}A - a_{surf}A^{2/3} - a_{coul}\frac{Z^2}{A^{1/3}} - a_{sym}\frac{(N-Z)^2}{A} - \delta(Z,N), \quad (2.6)$$

where δ is the pairing term which is defined as:

$$\delta = \begin{cases} -a_{pair}A^{-2/3} & \text{if N and Z are even;} \\ 0 & \text{if A is odd;} \\ a_{pair}A^{-2/3} & \text{if N and Z are odd.} \end{cases}$$

where the value of the constants are taken from [Kran88]:

$$a_{vol} = 15.5MeV \quad \text{volume term} \tag{2.7}$$

$$a_{surf} = 16.8MeV \quad \text{surface term} \tag{2.8}$$

$$a_{coul} = 0.72MeV \quad \text{Coulomb repulsion term} \tag{2.9}$$

$$a_{sym} = 23.0MeV \quad \text{symmetric term} \tag{2.10}$$

$$a_{pair} = 34.0MeV \quad \text{pairing effect term} \tag{2.11}$$

Using eq. 2.6 the semiempirical mass formula can be expressed as:

$$M(Z,A) = Zm(^1H) + Nm_n - B(Z,A)/c^2, \tag{2.12}$$

If the mass number A is fixed, equation 2.12 will represent a parabola of M vs. Z. The parabola will have a centre about the point where eq. 2.12 has a minimum. Nuclei with a certain mass number that do not have Z corresponding to this minimum can approach stability by β decay, while nuclei further away from stability can decay by emitting an alpha particle, a nucleon or even higher mass systems. The mass formula defines therefore the shape of the valley of nuclear stability.
On the other hand if Z is fixed one can analyse the stability of one element as A varies. As an example fig. 2.3 shows the different decay modes and half-lives for renium isotopes as A varies. The red points indicate proton decay, the yellow points indicate α decay, green and blue points indicate β^+ and β^- decay respectively.
The following sections describe all these decay modes.

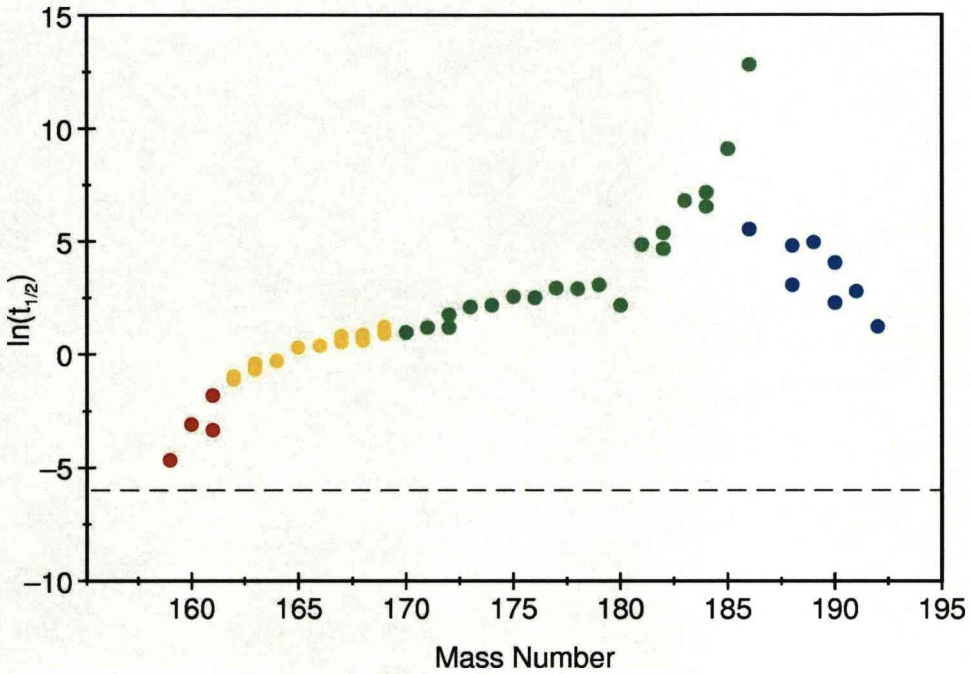

Figure 2.3: Different Re isotopes decay mode and half-lifes. The red points indicate proton decay, the yellow points indicate α decay, green and blue points indicate β^+ and β^- decay respectively.

2.3 Beta decay

Beta decay involves the transition of a neutron into a proton or vice versa with the emission of a electron and an antineutrino, a positron and a neutrino, or the capture of an atomic electron and emission of a neutrino. There are three types of beta decay:

$$n \rightarrow p + e^- + \bar{\nu}, \tag{2.13}$$

$$p \rightarrow n + e^+ + \nu, \tag{2.14}$$

$$p + e^- \rightarrow n + \nu, \tag{2.15}$$

where p indicate a proton, n a neutron, ν a neutrino, $\bar{\nu}$ an antineutrino, e^- and e^+ an electron and a positron respectively. In 1934 Fermi developed [Fermi34] a theory of β decay based on Pauli's neutrino hypothesis. This theory treats the weak interaction causing the decay as a perturbation and is therefore based on perturbation theory. According to Fermi's Golden Rule the decay rate for a transition from an initial (i) to a final (f) state is:

$$\lambda = \frac{2\pi}{\hbar} \mid M_{fi}^2 \mid \frac{dN}{dE}, \tag{2.16}$$

where $\frac{dN}{dE}$ is the density of final states and M_{fi} is the matrix element for the transition between the initial and final state. According to the theory it is possible to calculate the number of final states available for a particle with momentum in the range p to $p+dp$:

$$dn \propto p^2 dp \tag{2.17}$$

The number of final states which have simultaneously an electron and a neutrino with the proper momenta is:

$$dn \propto (p_e^2 dp_e)(p_\nu^2 dp_\nu) \tag{2.18}$$

Knowing that the neutrino mass is either zero or very small compared to the mass of the electron one can express its momentum in terms of the total energy E_0 released during the decay proces:

$$E_0 = E_e + E_\nu = E_e + p_\nu c \tag{2.19}$$

$$p_\nu^2 = \frac{(E_0 - E_e)^2}{c^2} \tag{2.20}$$

If the energy of the electron is fixed $dp_\nu \propto dE_0$ And the density of states can be rewritten as:

$$\frac{dN_f}{dE_0} \propto p_e^2 (E_0 - E_e)^2 dp_e \tag{2.21}$$

Another factor that has to be included in the theory is the effect of the Coulomb forces on the electrons. This effect is corrected for by multplying eq. 2.21 by the so called *Fermi-factor F(Z,E_0)* for which tables and plots are widely available [Enge66]. Inserting the Fermi-factor, the decay rate can be written as:

$$d\lambda \propto p_e^2(E_0 - E_e)^2 F(Z, E_e) dp_e \tag{2.22}$$

The total decay rate λ at which beta decays occur in which the momentum of the emitted electrons is between 0 and p_0 is proportional to the integral of eq. 2.22

$$\lambda \propto f(Z, E_0) = \int_0^{p_0} p_e^2(E_0 - E_e)^2 F(Z, E_e) dp_e \tag{2.23}$$

Thus including 2.23 into 2.16, and substituting $\lambda = 0.693/t_{1/2}$ one can introduce a quantity called the comparative half-life:

$$ft_{1/2} = 0.693 \frac{2\pi^3 \hbar^7}{g^2 m_e^5 c^2 \mid M_{fi} \mid^2}, \tag{2.24}$$

where g is a constant that characterized the β-decay strength. The comparative half-life gives us a way to compare β-decay probabilities in nuclei with different Z and E_0.

2.3.1 Angular momentum and parity selection rules

The emitted electron and neutrino carry away a total angular momentum that is the sum of the orbital angular momentum and the intrinsic angular momentum. The two particles have spins $1/2\hbar$ that can be parallel, giving a total S=$1\hbar$ or antiparallel, giving total S=$0\hbar$. These transitions are known as Gamow-Teller and Fermi transitions, respectively. The initial and final nuclear total angular momentum will therefore follow the rules:

I_f= I_i+ L Fermi transition

I_f= I_i +L+1 Gamow-Teller transition

Conservation of parity requires that the parity of the initial wave functions must

be the same as the final wave function, meaning the wave function of the electron, neutrino and final nucleus. The parity of the electron-neutrino wave function is $(-1)^L$ and this requires:

$$\pi_i = \pi_f(-1)^L \tag{2.25}$$

The hypothesis for the weak interaction responsible for the decay assumes a zero effective range so that the electron and the neutrino can be described as free particles once emitted:

$$\Psi_e = \frac{1}{\Omega^{1/2}} e^{i\frac{p_e r}{\hbar}}, \tag{2.26}$$

$$\Psi_{\bar{\nu}} = \frac{1}{\Omega^{1/2}} e^{i\frac{p_{\bar{\nu}} r}{\hbar}}, \tag{2.27}$$

$$\Psi_e \Psi_{\bar{\nu}} = \frac{1}{\Omega} e^{ikr}, \tag{2.28}$$

where Ω is an arbitrary normalization volume. It is possible to expand the electron and neutrino plane wave in spherical harmonics, assuming (kr< 1):

$$e^{i\mathbf{kr}cos\theta} = \sum_{l=0}^{\infty} i^l \frac{(2l+1)}{(2l+1)!!}(kr)^l P_l(cos\theta) \tag{2.29}$$

The transition matrix element will show the same dependence:

$$M_{if}^l \propto i^l \frac{(2l+1)}{(2l+1)!!}(kr)^l \tag{2.30}$$

One can clearly see that for small values of the argument (kr), which is usually the case in low-energy beta transitions, the matrix element has a maximum for l=0 and rapidly decrease increasing l. One usually refers to l=0 transitions as allowed decays and one speaks of first (l_β=1), second (l_β=2),...l_β forbidden beta transitions with the log fT value increasing by about 4 units in each step.

Selection rules			
Transition type	L	ΔI Fermi	ΔI Gamow-Teller
Allowed	0	0	1
First forbidden	1	1	0,1,2
Second forbidden	2	2	2,3
Third forbidden	3	3	3,4

Table 2.1: Selection rules for Fermi and Gamow-Teller transitions, ΔI indicates the difference in total angular momentum between initial and final state

Transition type	$\log fT_{1/2}$
Allowed	4.4 - 6.0
First forbidden	6 -10
Second forbidden	10 - 13
Third forbidden	$\geq$ 15

Table 2.2: Empirical determinations of $\log fT_{1/2}$

2.4 Alpha decay

Alpha decay is a type of radioactive decay which consists of the spontaneus emission of a ^{4}He nucleus from a parent nucleus. It can be represented by the following process:

$$ {}^{A}_{Z}X_N = {}^{A-4}_{Z-2}X_{N-2} + {}^{4}_{2}He_2. \tag{2.31} $$

In the process energy, linear and angular momentum must be conserved. By measuring spectroscopic properties from the emitted α particle important nuclear structure information can be extracted.

2.4.1 Alpha-decay Q-value

Conservation of energy and linear momentum during the process leads to the definition of the α-decay Q-value,

$$ [M_A - (M_{A-4} + M_\alpha)]c^2 = T_{A-4} + T_\alpha = Q_\alpha, \tag{2.32} $$

where M_A, M_{A-4}, and M_α are the masses of parent, daughter and α particle, respectively, T_{A-4} and T_α are the daughter and α particle kinetic energy.

Spontaneous α decay occurs only when Q_α is bigger than 0 and a net energy relase is produced during the process, though the effect of the Coulumb barrier means that the rate of α emission does not become appreciable until the Q-value is in the MeV range. The experimental α-decay Q-value can be obtained from the measured α particle kinetic energy from:

$$ Q_\alpha = T_{A-4} + T_\alpha = T_\alpha(1 + \frac{M_\alpha}{M_{A-4}}) \approx T_\alpha(1 + \frac{4}{A_d}). \tag{2.33} $$

where A_d is the daughter nucleus mass number.

The Q value derived above does take into account the energy that an alpha particle is losing when passing through the electron cloud that surrounds the

daughter nucleus. When dealing with electron bare nuclei a correction has to be applied. The screening correction E_{sc} is expressed as:

$$E_{sc} = (65.3Z^{\frac{7}{5}} - 80Z^{\frac{2}{5}})eV, \tag{2.34}$$

where Z is the atomic number of the parent. Further details on the screening correction can be found in references [Per57, Ras66]. The total Q value corrected for the electron screening effect can be defined as:

$$Q_{\alpha}^{bare} \approx T_{\alpha}(1 + \frac{4}{A_d}) + E_{sc}. \tag{2.35}$$

2.4.2 Alpha emission

One feature of the alpha decay is the dependence between the energy of the alpha and its half-life , this relationship was first noticed in 1911 by Geiger and Nuttall (Geiger-Nuttall rule,[Geiger11]) who found that for even-even nuclides of the same element:

$$Log_{10}T_{1/2} = a_1(Z)E_{\alpha}^{-1/2} + a_2(Z), \tag{2.36}$$

where a_1(Z) and a_2(Z) are element (atomic number Z) dependent empirical coefficients and E_{α} is the kinetic energy of the α-particle.

The first theory of α-decay was developed in 1928 by Gamow [Gamow28] and by Gurney and Condon [Cond28]. This theory, known as the one body model, assumes that the α particle is preformed inside the nucleus and that it is moving inside a spherical region determined by the daughter nucleus and it is assumed to knock with a frequency f against the walls of the spherical potential barrier V(r).

The potential can be described by an attractive short range component, responsible for the strong interaction between nucleons, and a Coulomb repulsive component. The radius of the nuclear matter is assumed to be uniform with

$R(A)=R_0A^{1/3}$, where $R_0\approx1.2$ fm. Outside this radius the potential is assumed to be:

$$V(r) = \frac{1}{4\pi\epsilon_0}\frac{Z_\alpha Z_{daugh}}{r}, \tag{2.37}$$

where Z_α and Z_{daugh} are the atomic number of the alpha particle and the daughter nucleus. Classically, the particle could not penetrate the barrier, but it could penetrate quantum mechanically through the "tunnel effect" with a penetration probability P, which, according to the WKB approximation can be espressed as:

$$P = exp\left[-2\int_{R_a}^{R_b}\frac{(2m)^{1/2}}{\hbar}[V(r)-Q_\alpha]^{1/2}dr\right], \tag{2.38}$$

where R_a and R_b are the entrance and exit radii of the α particle and m is the reduced mass which is defined as:

$$m = \frac{M_\alpha M_{daugh}}{M_\alpha + M_{daugh}} \approx \frac{4A_{daugh}}{4+A_{daugh}}m_\mu, \tag{2.39}$$

where m_μ is the atomic mass unit. The calculated decay constant $\lambda_{\alpha calc}$ is expressed as the product of the "'knocking frequency"' f, i.e. the number of time the α particle presents itself at the barrier and the penetration probability P:

$$\lambda_{calc} = f \cdot P[1/sec]. \tag{2.40}$$

In this work the experimental α-decay half-lives have been compared to the theoretical ones calculated according to the method developed by Rasmussen [Ras59]. Traditionally the theoretical calculation of barrier-penetration for α emission assumes an abrupt nuclear cut-off to the Coulomb potential at some effective nuclear radius. An optical-model analysis study by Igo [Igo58] derived by elastic scattering of α particles is used to provide a simple exponential expression for the real part of the α-nucleus potential:

$$V(r) = -1100exp\left[-\frac{r-1.17A^{1/3}}{0.574}\right]MeV, \tag{2.41}$$

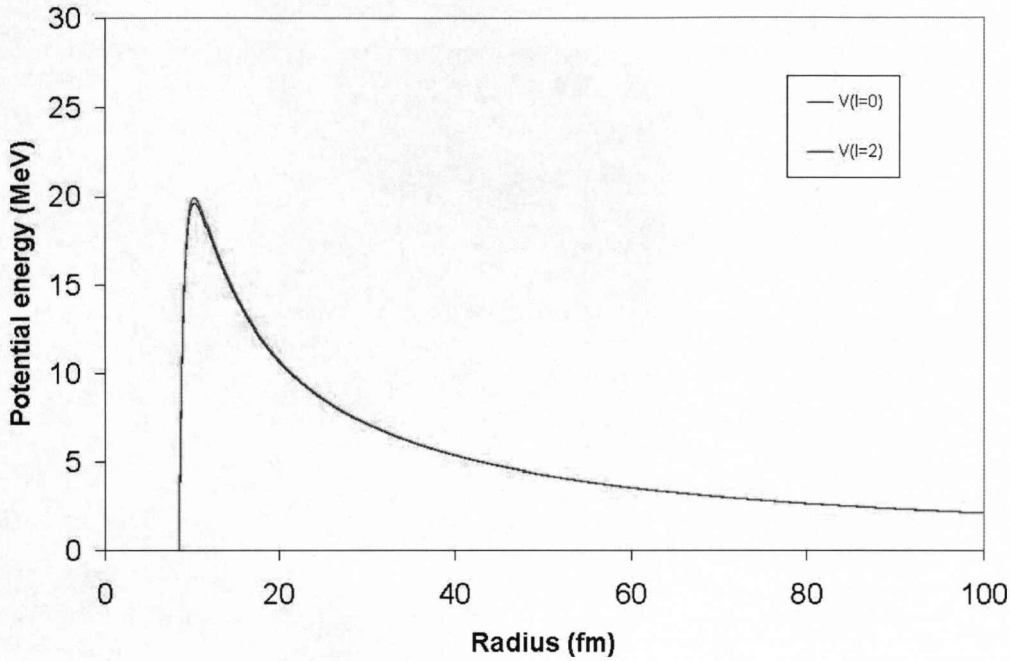

Figure 2.4: Potential energy calculated for ^{161}Os alpha decay assuming a l=0 and a l=2 angular momentum carried away by the emitted alpha.

where r is the radius in fm and A is the mass number. Rasmussen calculated the barrier penetration factor including Igo's potential and a centrifugal component term $V_l(r)=l(l+1)\hbar^2/2mr^2$ which has the effect of increasing the thickness of the penetration barrier, therefore reducing the tunnelling probablity of α particle with non-zero angular momentum. The knocking frequency is taken from normalization from a known unhindered alpha emitter, such as the ground state to ground state of ^{212}Po to the doubly magic ^{208}Pb. The resulting barrier penetration probability is:

$$P = exp\left[-2\int_{R_0}^{R_i}\sqrt{(2m_\alpha/\hbar^2)(V(r)+\frac{\hbar^2}{2mr^2}l(l+1)-E}dr\right], \qquad (2.42)$$

where M is the reduced mass of the α particle, l is the orbital angular momentum of the emitted α particle.

2.4.3 Hindrance factor and Reduced alpha emission width

The alpha emission probability is dependent on two different processes: the formation of an α particle within the nucleus from four nucleons and the penetration and escaping through the barrier. The one body model model assumes that the α particle is preformed inside the nucleus. This implies a complete overlap between the final nuclear wavefuncion describing the daughter nucleus ψ_f(A-4) and the α wavefunction ψ_α and the initial A-particle nuclear wavefunction ψ_i(A). The overlapping between these wavefunctions is highly dependent on nuclear structure factors, and might lead in a reduction of the α decay probability.
Rasmussen defined the reduced α-decay width δ^2 (eV) by using the barrier penetrability calculated with equation 2.42 and the experimental decay rate λ_{exp}:

$$\lambda_{exp} = \frac{P\delta^2}{h}. \tag{2.43}$$

The difference between calculated and measured half-lifes is an indication of the different structure of mother and daughter nuclei. Another typical quantity used to characterize alpha decay is the hindrance factor HF, which is expressed by:

$$HF = \frac{T_{1/2}^{exp}}{T_{1/2}^{calc}} \tag{2.44}$$

When the angular momentum l carried away by the α particle is zero, means that the parent and daughter nucleus have the same angular momentum, thus they have similar configurations and the decay is unhindered. In this case the HF is less than four. When the α particle has $l > 0$, then HF > 4, usually at least a few tens of units.

2.5 Proton decay

The emission of one and two proton from a nucleus was first predicted by Goldansky [Gold60] to occur in nuclei with a positive Q value:

$$ {}^{A}_{Z}X_N = {}^{A-1}_{Z-1}X_N + p. \tag{2.45} $$

$$ Q_p = [M_Z - (M_{Z-1} + M_H)]c^2 = T_p(1 + \frac{M_H}{M_{daugh}}). \tag{2.46} $$

The theory for proton decay is analogous to the α decay. A major difference is the height of the Coulomb potential, which is lower for protons by a factor of two, being linearly proportional to the emitted particle charge. The centrifugal barrier on the other hand is four times higher, being inversely proportional to the reduced mass. The emitted proton is therefore very sensitive to the angular momentum, and this sensitivity can be exploited to obtain spectroscopic informations on the structure from which the proton was emitted. As an example fig. 2.5 illustrates the potential energy for proton emission in ^{155}Ta and how the centrifugal barrier height varies as the angular momentum of the proton increases.

The selection rules for proton decay are:

$$ I_i = I_f + l_p \pm \frac{1}{2}, \tag{2.47} $$

$$ \mid I_i - I_f \mid \pm\frac{1}{2} < l_p < (I_i + I_f) \pm \frac{1}{2}, \tag{2.48} $$

$$ \pi_f = \pi_i(-1)^l_p \tag{2.49} $$

where I_i and I_f are the initial and final spin of the nucleus and π indicates the parity of a state.

2.6 Proton and neutron drip lines

The knowledge of nucleon emission from the ground state of spherical as well as deformed nuclei provides information on the limits of nuclear existence. The

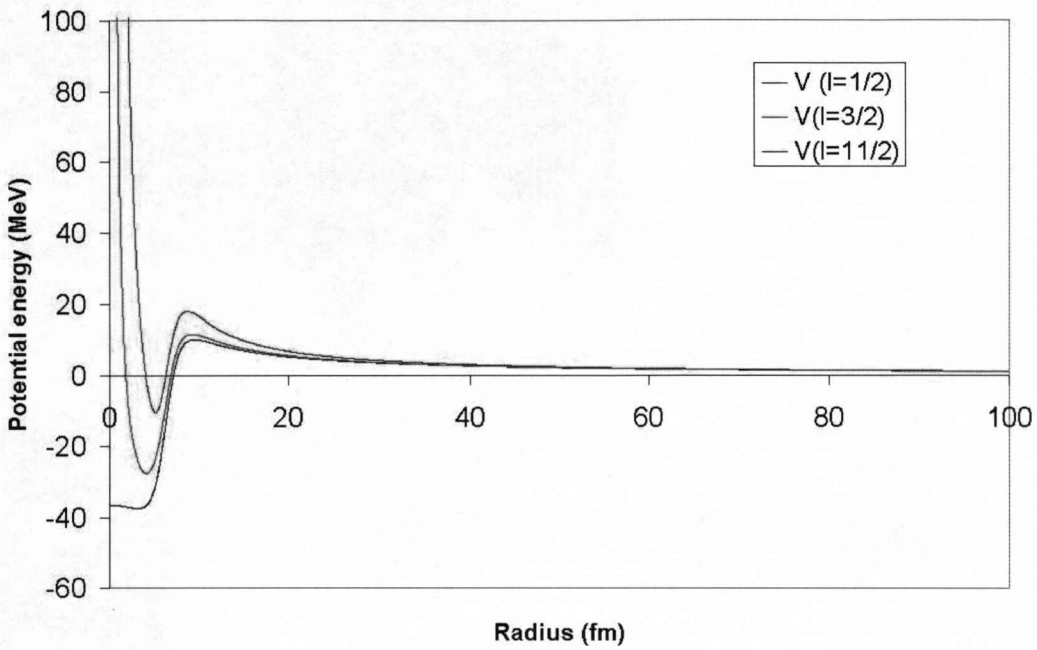

Figure 2.5: Representation of the potential for the emission of a proton in ^{155}Ta assuming various angular momentum for the emitted proton.

Coulomb repulsive force limits the number of isotopes with an excess of proton compared to the number of isotopes with an excess of neutrons. One can define the separation energy for a neutron or a proton as the energy required to separate a nucleon from a nucleus in its ground state, or:

$$S_p = [M(Z-1,N) + M_p - M(Z,N)]c^2, \tag{2.50}$$

in case of proton emission, the same is valid for the neutron separation energy S_n. Fig. 2.6 shows the proton separation energy for even Z nuclei taken from [MNK]. The condition to have neutron or proton emission is $S_n<0$ or $S_p<0$, which can also be expressed in terms of binding energy as:

$$B(Z-1,N) - B(Z,N) > 0. \tag{2.51}$$

One can see that the different terms in the binding energy B(Z,A) play key roles

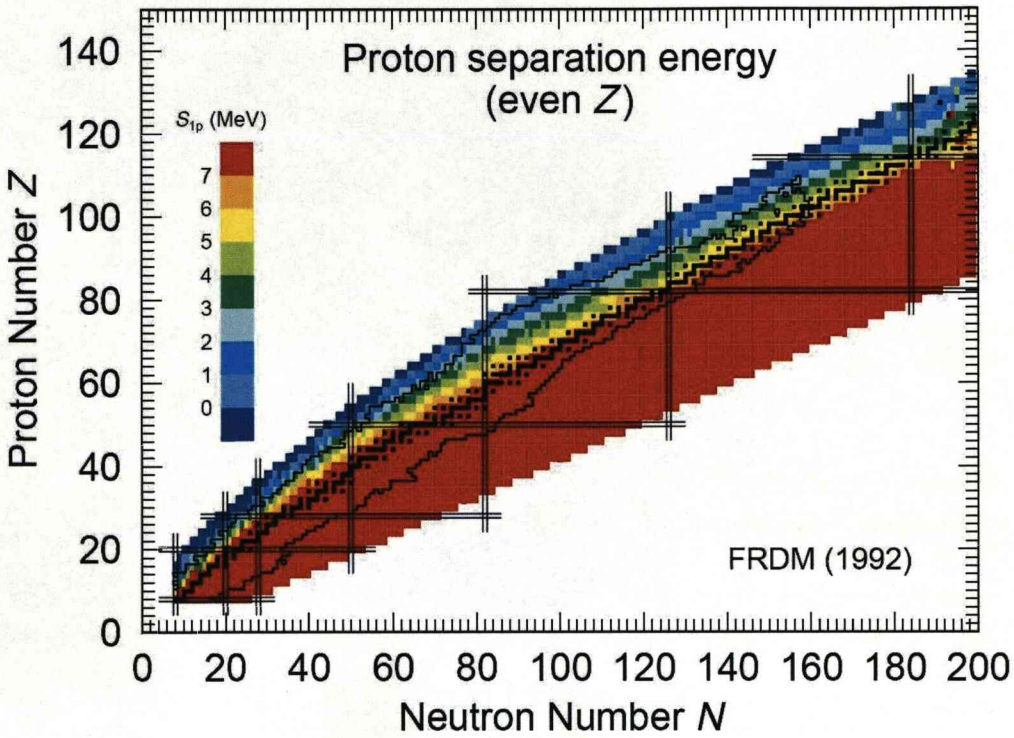

Figure 2.6: Proton separation energy for even-Z nuclei from [MNK].

in determining whether the separation energy of a nucleon is negative and the nucleus become proton or neutron unbound. Neutron rich nuclei become neutron unbound when the loss in binding energy caused by the symmetry term overcomes the gain due to the volume term when adding a neutron to the nucleus. The same effect is present for neutron-deficient nuclei only for Z<50. The proton drip line crosses the proton-neutron symmetry line (N=Z) at Z=50 so above Z=50 the symmetry term results in an increase in binding energy. For these nuclei the Coulomb repulsion between protons is responsible for proton emission, and causes the proton drip line to lie much closer to the valley of beta stability compared to the neutron drip line.

In the calculation of the drip lines the semi-empirical mass formula does not include several nuclear shell structural effects that are included in more sophis-

ticated mass model formulas such as in [Moll95]. Taking a look at the location

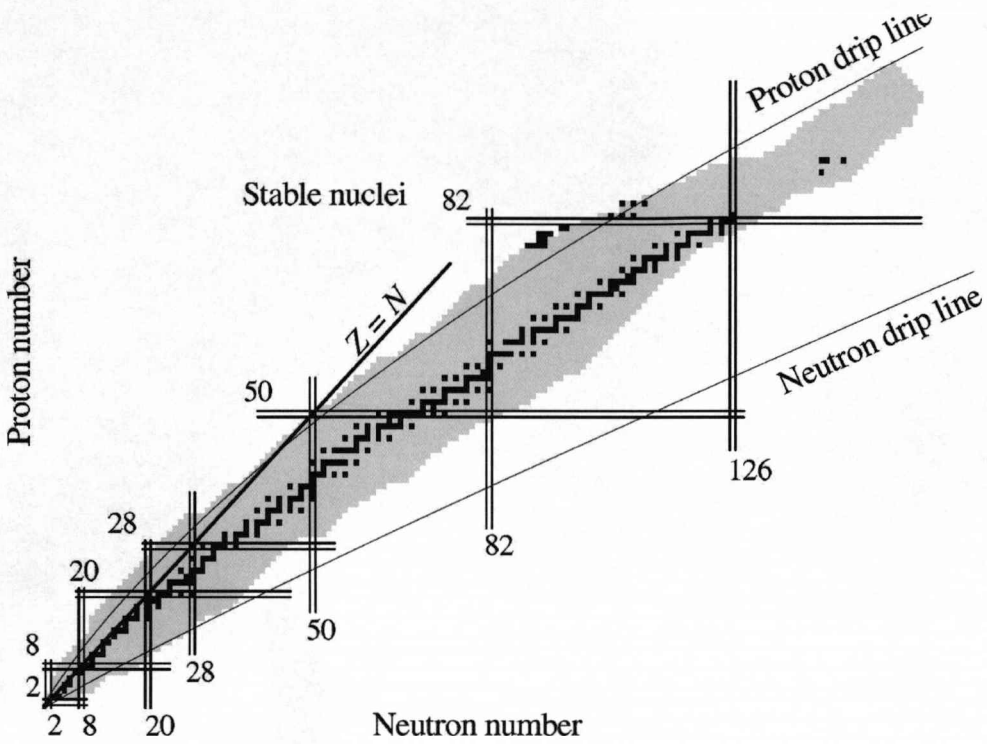

Figure 2.7: Chart of nuclides showing the valley of nuclear stability, proton and neutron drip line and the proton-neutron (N=Z) symmetry line.

of the proton drip line one can notice that for even-Z nuclei the proton drip line is shifted approximately 10 neutrons away from the stability line compared with odd-Z nuclei. This effect is due to the large gain in binding energy caused by the proton pairing. Another interesting aspect of proton emission is the effect of the Coulomb force. In addition to the effect of Coulomb repulsion on proton emission, the Coulomb barrier that protons have to go through before escaping from the nucleus also has to be considered. This delay effect causes the emission of unbound protons to have a much longer half-life as compared to the half-life proton unbound resonances which are of the order of 10^{-18}s. For nuclei with Z<20 the Coulomb barrier is not high enough to delay proton emission significantly, and

only short-lived proton unbound resonances can be expected. In heavier nuclei (especially above Z=50) the Coulomb barrier becomes high enough to have an effect on the proton emission half-life. The Coulomb effect smears out the proton drip line so that more than one proton emitting isotope can be observed for a particular element.

Chapter 3

Experimental Methods and Set-up

3.1 Introduction

As we extend our research towards regions such as the proton drip line, the production of nuclei with such an extreme N/Z ratio becomes increasingly difficult, and several factors must be taken into account. The reaction chosen to produce such nuclei is usually a fusion-evaporation reaction with a low cross section (few μb or less), which is swamped by background from fissioning compound nuclei and competing reaction channels. The beam and the target should be proton rich to maximize the yield. The experimental set-up should be capable of discriminating the nuclei of interest, and uniquely identifying nuclei and their radioactivity.

A good experimental set-up which fulfils all these requirements is the facility at the University of Jyväskylä. The data analysed in this work were indeed produced via heavy ion fusion reactions during experiments at the University of Jyväskylä accelerator laboratory. The fusion evaporation residues were separated in flight from primary beam particles and other products recoiling out of the target using the gas-filled recoil separator RITU [Lei97]. After separation, the fusion products

were focused and implanted into a position sensitive silicon detector which is the main component in the focal plane detector system. The final identification of the implanted fusion-evaporation residues was based on the method of position and time correlation [Schmidt84, Schmidt00] with the subsequent proton and alpha decays being identified in the silicon detector.

The decreasing production rates of more neutron-deficient isotopes in heavy-ion induced fusion reactions hinders in-beam gamma-ray spectroscopic measurements. Thus, proton emission and alpha decay provide often the only viable tools to obtain spectroscopic information about these most neutron-deficient heavy nuclei. The region of interest close to the N = 82, Z = 82 intersection is the heaviest in which in-beam spectroscopy measurements have been performed on nuclei beyond the proton drip line. The method used to investigate this region is the selective technique of recoil decay tagging (RDT). The set-up for RDT experiments used in this work includes the JUROGAM γ-ray spectrometer, the gas-filled recoil separator RITU and the multi-detector focal plane spectrometer GREAT. A brief description of the reaction mechanism and the experimental method is presented in the next sections.

3.2 Heavy-Ion fusion evaporation reactions

When studying proton-rich heavy nuclei, the fusion mechanism is the most suitable production method. When an accelerated heavy-ion projectile is fused with a target nucleus a compound nucleus is produced. Just by fusing two nuclei one will automatically obtain a neutron-deficient compound nucleus since the Coulomb repulsion between protons affects the line of stable nuclei, bending it to the neutron rich side. The compound nucleus is an unstable excited system and will deexcite within 10^{-19} s by undergoing fission or by emitting nucleons and/or alpha particles and finally γ radiation. By detecting the emitted particles we can

extract some important information about the nuclear structure of the emitting nucleus such as angular momentum and excitation energy. In order to have a fusion reaction the projectile nucleus should overcome the repulsive barrier V_{Coul} caused by the Coulomb field of the target nucleus.

$$V_{Coul}(MeV) = \frac{Z_1 Z_2 e^2}{4\pi\epsilon_0 R_{Coul}} = 1.44 \frac{Z_1 Z_2}{R_{Coul}(fm)} \tag{3.1}$$

where $Z_1$and Z_2 are the atomic numbers of the target and projectile nuclei and $R_{Coul} = R_i + R_t$ is the Coulomb radius again of the target and projectile nuclei.

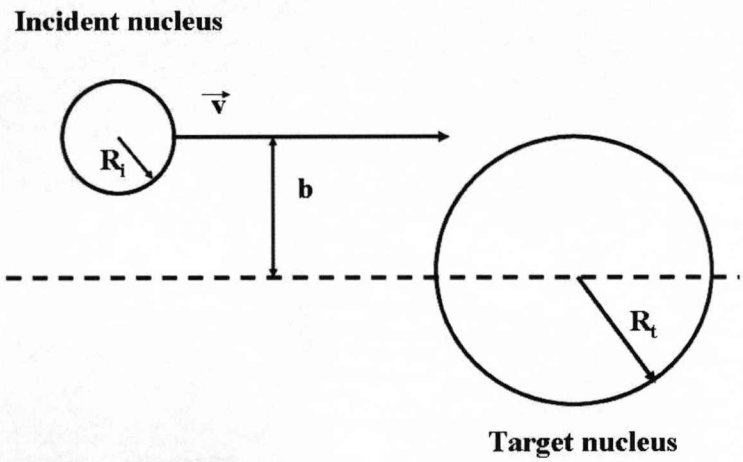

Figure 3.1: Schematic draw of an incident nucleus impacting on a target nucleus with an impact parameter b. R_i and R_t are the radii of the incoming projectile nucleus and target nucleus.

The excitation energy of the compound nucleus can be expressed as the sum of the kinetic energy E_{CM} of the nuclei in the centre of mass frame with the Q value of the reaction.

$$E^* = E_{CM} + Q = \frac{M_t}{M_i + M_t} E_i + (M_i + M_t - M_c)c^2 \tag{3.2}$$

Here the subscripts i, t and c denote the incident, target and compound nucleus, and E_i is the beam energy in the laboratory frame. As the impact parame-

ter b changes different types of reactions take place: when the two nuclei overlap completely the fusion reaction can take place and a compound nucleus formed; when they overlap partially, inelastic nuclear reactions occur; and when they are far apart and b is large, Coulomb excitation can occur. After the compound nucleus is formed it can undergo fission or decay via the mechanism described in the next section. Fission is a major competing process and it is important that the experimental set-up is able to separate fission from fusion products.

3.2.1 Compound nucleus decay

If the intermediate system survives fast fission, the compound nucleus can lose its excitation energy by evaporating nucleons, alpha particles and gamma radiation. Shortly after being formed (about 10^{-19} s), the compound nucleus will evaporate a few particles. By doing so the nucleus will lose at least the equivalent of the binding energy (8MeV) and on average $\sim 1\,\hbar$ of angular momentum for each emitted nucleon. After about 10^{-15} s gamma ray emission starts to compete with particle emission, and when the excitation energy is less then the nucleon separation energy, gamma emission is the only way to dissipate energy.

The radiation is mainly electric dipolar (E1) in nature with an energy that varies between 2 and 8 MeV and it proceeds to remove excitation energy from the nucleus towards the yrast line, which connects the levels of the lowest excitation energy for each spin value. The high density of states makes it not possible to resolve these gammas and they will form a continuum. When the nucleus is approaching its ground state and the internal energy is below about 2 MeV, discrete gamma transitions can be clearly detected and give an insight into the nucleus' structure. These gamma rays can be used to construct level schemes by using γ-γ coincidence techniques.

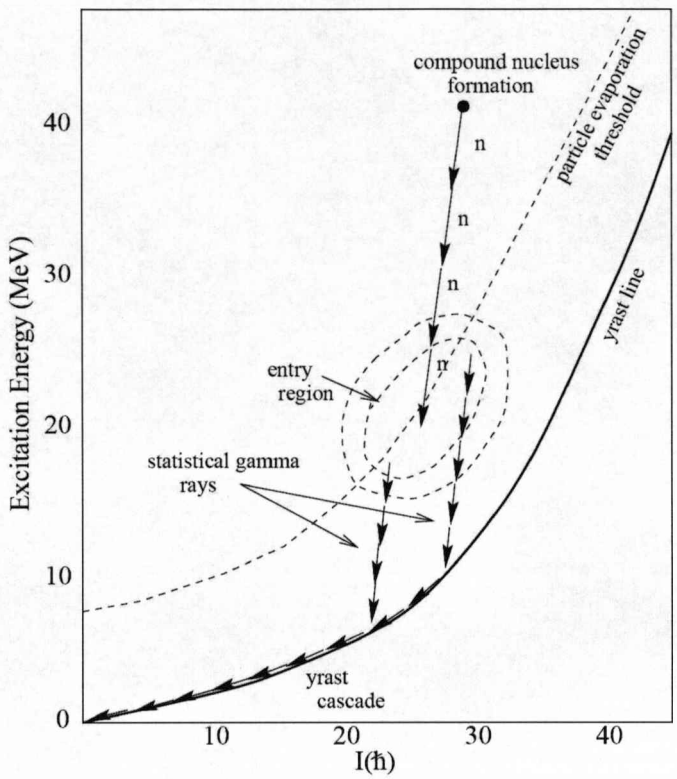

Figure 3.2: Schematic diagram of the de-exitation of a compound nucleus. Angular momentum is plotted versus the excitation energy. The yrast line and the particle evaporation treshold are also highlighted.

3.3 Recoil separation

Nuclei of interest have to be separated from the primary heavy-ion beam that did not react with the target nuclei and from other reaction products. A recoil separator can separate particles having different mass to charge ratios or velocities into different spatial trajectories by means of magnetic and electric fields. These trajectories are defined in a magnetic field by the Lorentz force. One defines the magnetic rigidity $B\rho$ of a particle with electric charge q and mass m moving in a

homogeneus magnetic field B with velocity v perpendicular to the field as:

$$B\rho = \frac{mv}{q}. \tag{3.3}$$

where ρ describes the radius of curvature in the magnetic field. Fusion products recoil out from the target with a broad distribution of charges and velocities. According to equation 3.3 the recoil's spatial distribution after the dipole magnet in vacuum mode mass separators is very wide. Thus, only few charge states can be focused to the focal plane detector and the efficiency is highly affected. On the other hand a great advantage of vacuum mode mass separators is high mass resolving power, which can be the most significant property for some experiments. A method to achieve high efficiency is to fill the dipole magnet with dilute gas.

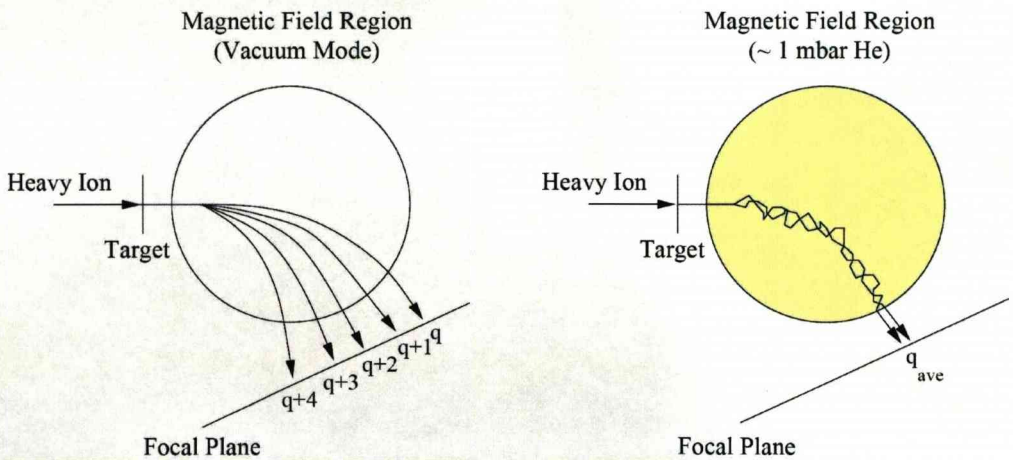

Figure 3.3: Illustration of the separation obtained for magnetic separator; on the left in vacuum mode the different charge states follow different trajectories. On the right the gas filled mode, where an average charge state is created through collision between recoils and the gas atoms.

When heavy ions penetrate the gas they undergo atomic charge-changing collisions, and this makes the charge state of the ions change around the mean charge

state q. The average charge state q_{ave} can be found using some assumptions proposed by Bohr [Bohr40] and Lamb [lamb40]. The approximation is that an ion which is moving in a gas loses those electrons whose speed is less than its own speed. The average charge state q_{ave} is approximated by the Thomas-Fermi model of the atom as:

$$q_{ave} = (\frac{v}{v_0})Z^{\frac{1}{3}}, \tag{3.4}$$

In these equations v_0 is the Bohr velocity (2.19 10^6 m/s) and Z is the atomic number of the ion, and the equation is valid if the velocity of the ion is in the range: $1<v/v_0<Z^{2/3}$. The magnetic rigidity $B\rho$ can now be written using eq. 3.4 [Ghio88]:

$$B\rho = 0.0277\frac{v}{v_0}\frac{1}{q}A, B\rho = 0.0277\frac{A}{Z^{1/3}}, \tag{3.5}$$

In this approximation one can see that the $B\rho$ of the ion in gas is dependent only on the mass number A and the atomic number Z of the ion and it is independent of the velocity and the original charge state of the ion. The spatial distribution of the recoils after separation is narrower and thus the recoil collection efficiency higher than in vacuum mode. On the other hand in the filling gas mode a disadvantage is the decrease in the mass resolving power. Typical mass resolution of gas-filled recoil separators is 10%.

3.3.1 The RITU recoil separator

The gas-filled recoil separator RITU (Recoil Ion Transport Unit), shown in figure 3.4 was originally designed [Lei95] for the studies of super heavy elements using asymmetric fusion reactions. The optical configuration of RITU is QDQQ, where D corresponds to a magnetic dipole field and Q to a quadrupole field. The entire separator is filled with helium gas with a pressure in the range 0.5-3 mbar. A differential pumping system separates the high vacuum of the beam line from the

gas volume in RITU. In the RITU separator the quadrupole magnet in front of the dipole magnet provides extra focusing, providing that the evaporation residues optimally match the dipole magnet acceptance and thus increase the transmission of the separator up to ~30%. The dipole magnet separates the fusion-evaporation

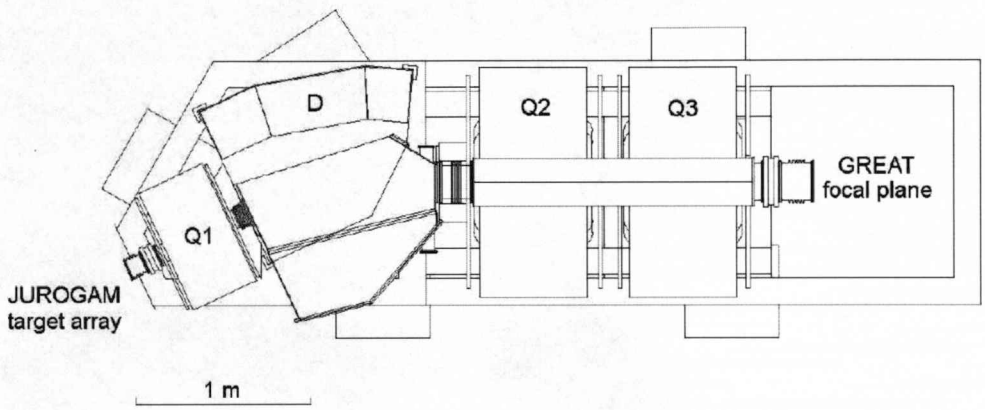

Figure 3.4: Schematic view of the RITU gas-filled recoil separator showing the position of the focal plane array GREAT and the JUROGAM array at the target position.

products from the primary beam particles and the other reaction products, which are stopped on the beam stop inside the dipole chamber, see figure 3.4. The fusion products are then focused onto the focal plane detector system of the separator using two quadrupole magnets.

3.4 The GREAT spectrometer

The Gamma Recoil Electron Alpha Tagging (GREAT) spectrometer is a combination of gas, silicon and germanium detectors. Fig. 3.5 shows the complete experimental set-up at JYFL, comprising from the right the JUROGAM array, the RITU gas-filled recoil separator and the GREAT focal plane spectrometer.

GREAT was designed to measure the protons, α particles, β particles, γ rays, X rays and conversion electrons emitted by reaction products transported to the focal plain of a recoil separator. Further details and description can be found in references [Page03] and [And04]. Separated fusion-evaporation residues are focused

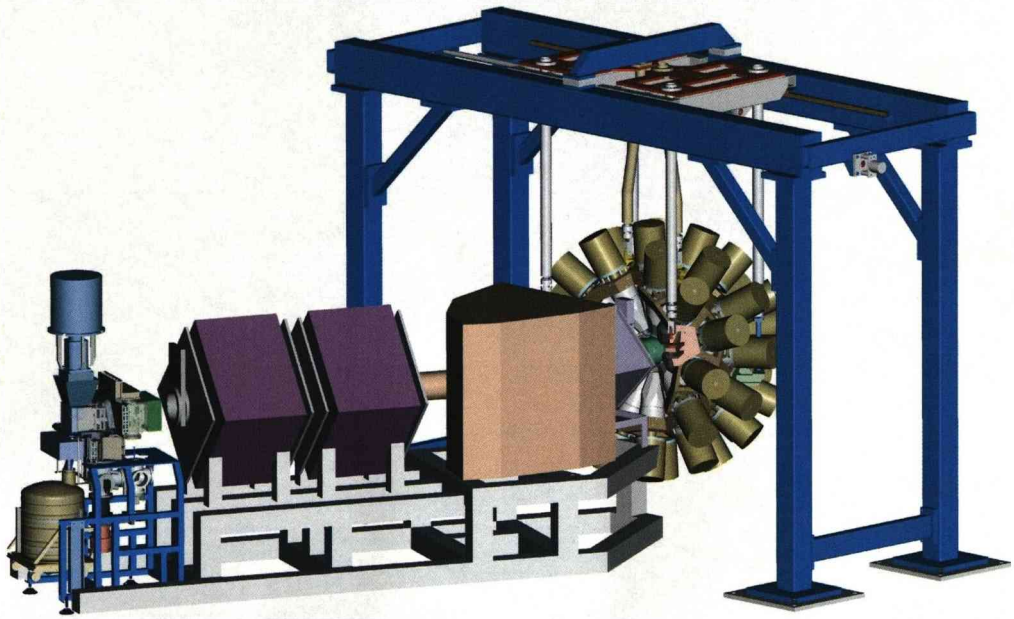

Figure 3.5: The experimental JUROGAM plus GREAT plus RITU set-up in Jyväskylä

and implanted into a position-sensitive silicon strip detector at the focal-plane detector system shown in figure 3.6. The final identification of the implanted products was based on the method of position and time correlation with the subsequent decays in the silicon strip detector. In the next sections each component of the GREAT spectrometer is explained more in detail.

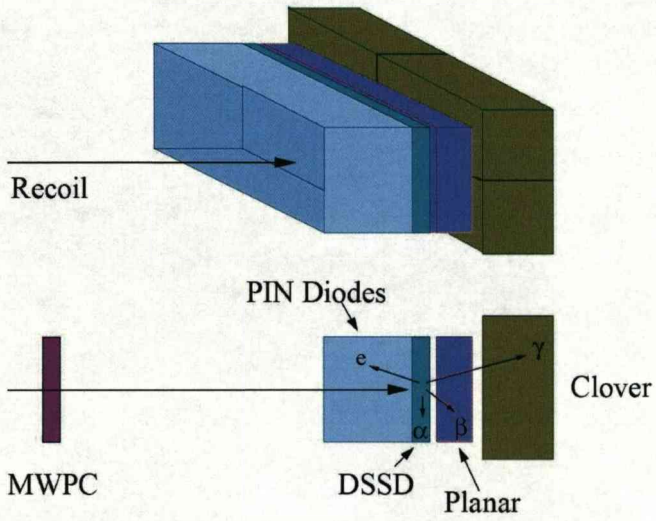

Figure 3.6: Schematic representation of the GREAT spectrometer.

3.4.1 The Multiwire Proportional Counter

A transmission multiwire proportional counter (MWPC) was installed at the entrance of GREAT, for the detection of particles arriving at the focal plane of RITU. It comprises four cathode wire planes, an anode wire plane and two mylar windows. The entrance window measures 131mm x 50mm and separates the ~3.5 mbar isobutane from the low-pressure helium gas of RITU, while the exit window separates the isobutane from the vacuum in which the other GREAT detectors operate. The MWPC allows recoiling reaction products which will pass through to be distinguished from their radioactive decays. Another feature of the MWPC is to distinguish between beam-like and recoil-like particles. The gas detector records the energy loss, time and position of any particle passing through it. The position information is obtained by comparing the delay line readouts from the ends of vertical and horizontal wire planes with a fast signal

from the anode. Combining this information and the time of flight between the MWPC and the DSSD one can eliminate unwanted scattered beam events and thus increase the correlation efficiency.

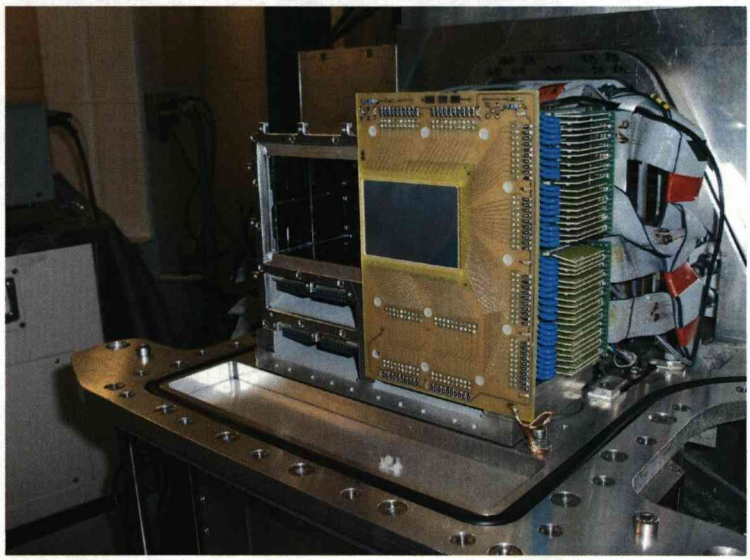

Figure 3.7: Photograph of one double sided silicon strip detector plus PIN detectors.

3.4.2 Implantation Detector

The transmitted recoils are implanted into a pair of double-sided silicon strip detectors (DSSDs). The DSSDs are used to measure the energies of ions that are implanted and of the protons, α particles and β particles they subsequently emit. Fig. 3.7 shows a photograph of one double sided strip detector during a replacement of the second DSSSDs detector. Each DSSD has an active area of 60 mm x 40 mm and a thickness of 300 μm. They are mounted side by side and have 60 vertical and 40 horizontal strips. The strip pitch is 1 mm in both directions, giving a total of 4800 pixels. The DSSSDs are mounted on a hollow block through which coolant is circulated, to reduce their temperature to -20C. The active areas of the two DSSDs are separated by a gap of 4 mm, giving an

estimated typical collection efficiency of 85%.

3.4.3 Conversion electron detector array

Typically reaction products are implanted into the DSSDs at depths of 1-10 μm, depending on the energy. Therefore α particles, β particles and conversion electrons have a significant probability of emerging from the DSSD in the backward direction relative to implantation. To measure the energies of these particles the DSSD is surrounded by 28 silicon PIN diodes mounted in a box arrangement. Each PIN diode has an active area of 28 mm x 28 mm and has a thickness of 500 μm.

3.4.4 Planar germanium strip detector

To measure the energies of X rays and low-energy γ rays a planar double-sided germanium strip detector has been designed for GREAT. The detector has an active area of 120 mm x 60 mm and a thickness of 15 mm. It is positioned behind the DSSSDs approximately 10 mm downstream of the DSSD. Both faces are segmented into 24 and 12 orthogonal 5 mm wide strips, respectively, giving a total of 288 effective pixels. The detector is housed in its own cryostat and mounted directly inside the GREAT vacuum chamber to minimise the attenuation of the photons. It can also be used to detect high-energy β particles (>2 MeV) that penetrate through the DSSSD.

3.4.5 Clover germanium detector

The energies of higher energy γ rays are measured using a large voulume HPGe detector mounted outside the GREAT vacuum chamber. The detector has four coaxial germanium crystals each segmented into four regions. Each of the four germanium crystals measures 70mm in diameter and 105mm in length. A sup-

pression shield with bismuth germanate crystals, 185 mm long, surrounds the clover detector to improve its peak-to-total ratio.

3.5 The JUROGAM array

Part of the data analysed in this work utilized the JUROGAM germanium detector array to detect prompt γ ray transitions at the target area. When studying nuclear structure at high spin, long γ-ray cascades are emitted over all directions and detectors with high energy resolution and efficiency in a wide energy range are required. Typically large germanium detector arrays have a geometry that covers as much area as possible around the target. In the case of JUROGAM the spatial coverage cannot be 4π since the entrance of the quadrupole in front of the RITU separator is placed directly after the target area. Fig. 3.8 shows a photograph of part of the JUROGAM array with the cooling Dewars and the framework holding the detectors. The JUROGAM array consists of 43 EUROGAM phase-I Ge detectors from the former EUROBALL array. Each detector module comprises a high purity Ge detector and a bismuth germanate Compton suppression shield to reduce the background caused by multiple Compton scattering of the incident radiation. The 43 detectors are mounted in a a honeycomb geometry to provide the best solid angle coverage.

3.6 Recoil Decay Tagging

The data analysed in this thesis were produced via heavy ion fusion evaporation reactions. This type of reaction usually generates a large number of γ rays around the target position, many of which are produced from fission events, deexcitations following Coulomb excitation, transfer reactions and from other open fusion evaporation channels. γ rays associated with the nucleus of primary in-

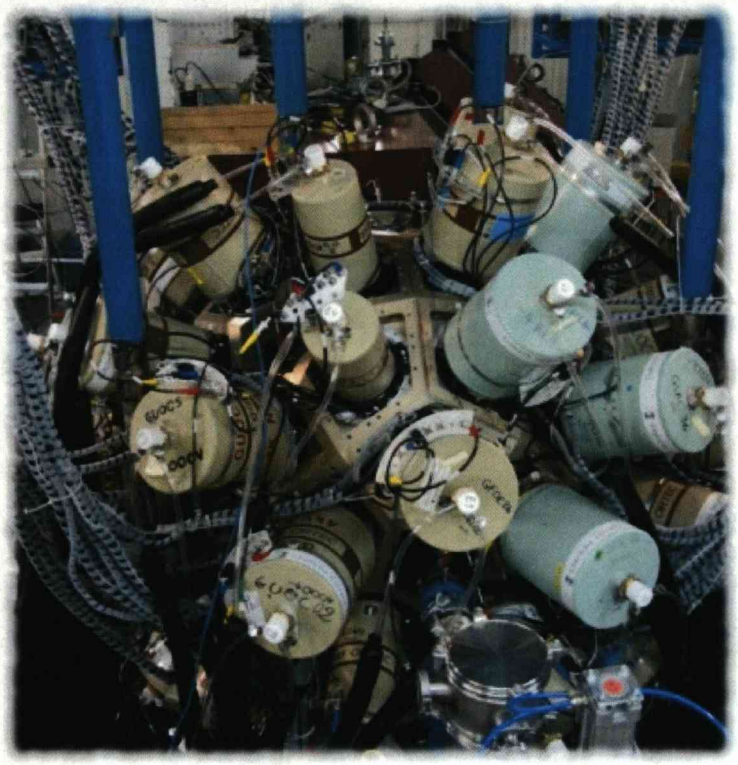

Figure 3.8: Phoograph of the JUROGAM array showing the cooling Dewars and the honeycomb framework holding the detectors.

terest of the study could be hidden among the other γ rays produced during the experiment. It is therefore of primary importance to clearly select a specific reaction channel in order to assign the γ rays to the correct recoil. The Recoil-Decay Tagging (RDT) [EPaul95] technique was developed to obtain this selection. It is a powerful technique to pick out those channels that otherwise would be swamped in the background from other reaction products.

By means of the specific radioactive decay of a nuclide the RDT technique is able to identify a certain fusion-evaporation residue. Nuclei close to the proton drip line often decay by alpha or proton emission, and these particle emissions have discrete and unique energies that can be used as a signature of the nuclei from which the particles were emitted. The only limitation of this technique

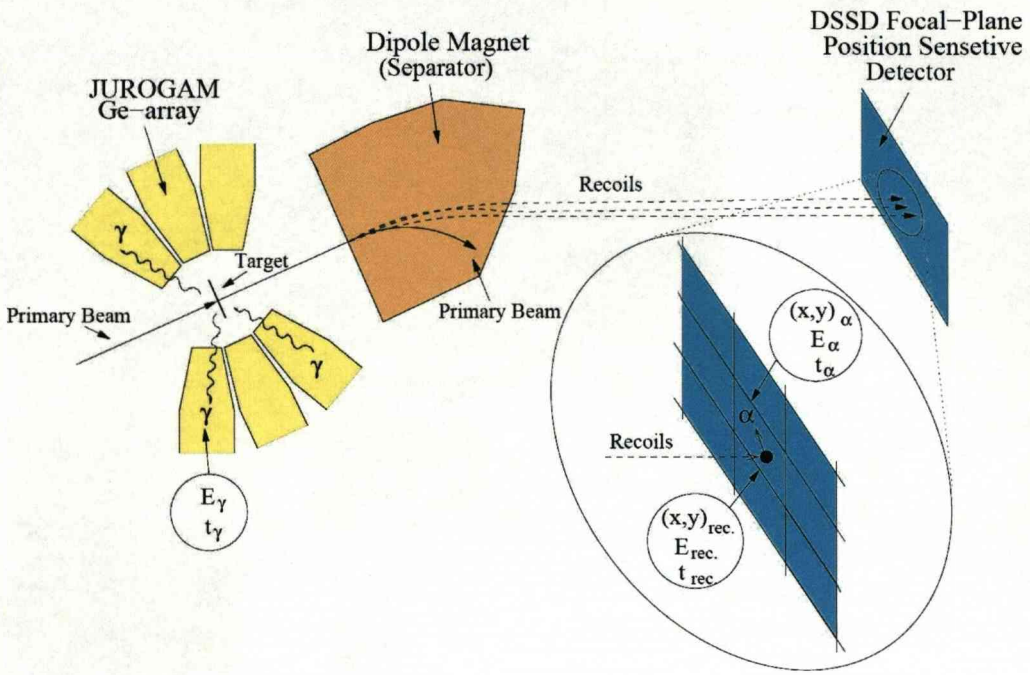

Figure 3.9: Schematic view of the RDT technique. When an α decay or proton is detected in the DSSD detector, the position and time are recorded, so that the corresponding recoil can be identified in the same pixel. One then can search back in time and check the prompt γ rays emitted at the target position in coincidence with the recoil.

comes from the flight time of the recoil through the separator. In the case of RITU the flight time of a recoil through the separator is usally 0.5-1 μs, so if the half-life for the charged particle emission is not too short the radioactive decay can be detected at the focal plane DSSD. When a recoil is implanted into the DSSD its spatial and temporal information are recorded. The same information is recorded for the subsequent decay, and correlation between radioactive decay and implanted recoil can be performed. Fig. 3.9 shows the principles behind the RDT technique. The identification of the implanted recoil is made with its decay particle, α particle or proton. The search time between recoil implantation and

the subsequent radioactive decay in the same pixel in the DSSD is usually taken to be three half-lives of the decay in question.

3.6.1 Total data readout

Usually experiments using implantation detection system relied on an hardware triggering. This means that a trigger condition is set in a detector and then signals from all other detectors are delayed and read out as being part of that event. This leads to a large dead time, especially when counting rates are high

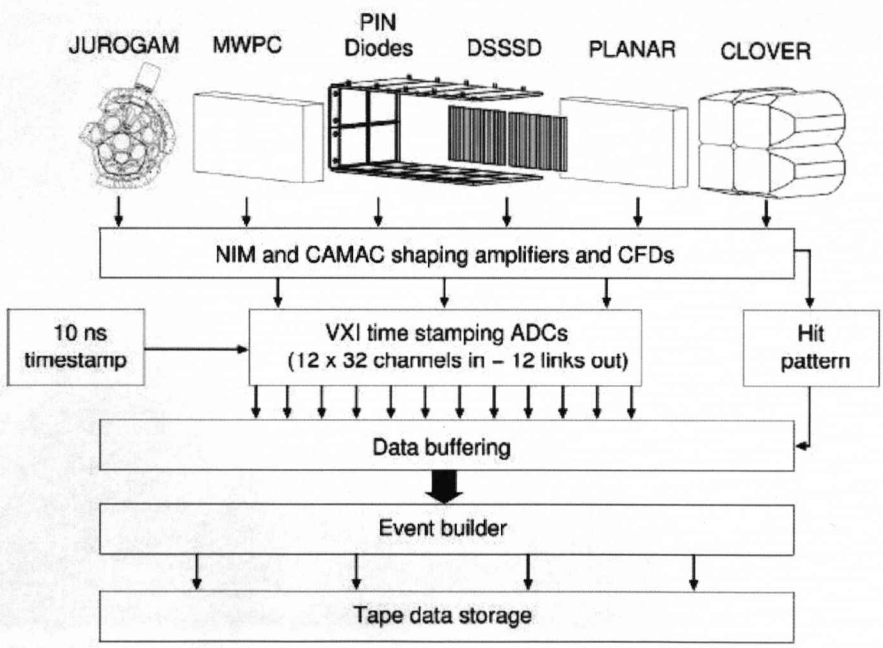

Figure 3.10: Schematic representation of the TDR data acquisition system.

or when trigger gates are wide. The Total Data Readout concept was developed for GREAT to overcome this limitation. All detectors channels have their output treated independently and continuously, so that each channel has its energy recorded and time stamped with the synchronization of a 100 MHz global clock.

The data stream is time ordered and allows the trigger conditions and the event construction to be set via software. Figure 3.10 shows a schematic representation of the layout and electronics of the data acquisition system.

Chapter 4

Data analysis

4.1 Energy Calibration Procedure

Calibration of all detectors at the focal plane was performed with the appropriate sources, in order to cover the different energy ranges typical of each detector. The DSSD was initially calibrated with an external alpha source positioned at the focal plane. The source is a triple alpha source, containing ^{241}Am, ^{239}Pu and ^{244}Cm, which emits α particles at distinct energies between 5 and 6 MeV. The calibration was repeated at the end of the experiment to check that no gain shifts happened during the experiment. The calibration with the external source is not appropriate for decays that happen internally in the detector because it does not take into account the energy loss caused by the particle passing through the source windows and the dead layer at the detector's surface or the part of the daughter's recoil energy that is registered. An internal calibration was therefore performed with the identification of known alpha decays produced during the experiment. The alpha peaks used for the internal calibration were taken from Ref. [Page96] using α decay lines of implanted $^{149-150}$Dy(3973,4233 keV), ^{149}Tb(3973keV),$^{156-157}$Hf(7782, 5728 keV), and $^{155-156}$Lu(7390, 5565 keV) for the first experiment. These peaks were clearly visible in every strip of the DSSD al-

pha spectrum covering a large energy interval, see Figure 4.1. For the second experiment performed in July 2007 the peaks used were ^{149}Tb (3967 keV) and ^{161}W (5777 keV). The detector usually has a linear relationship between the peak

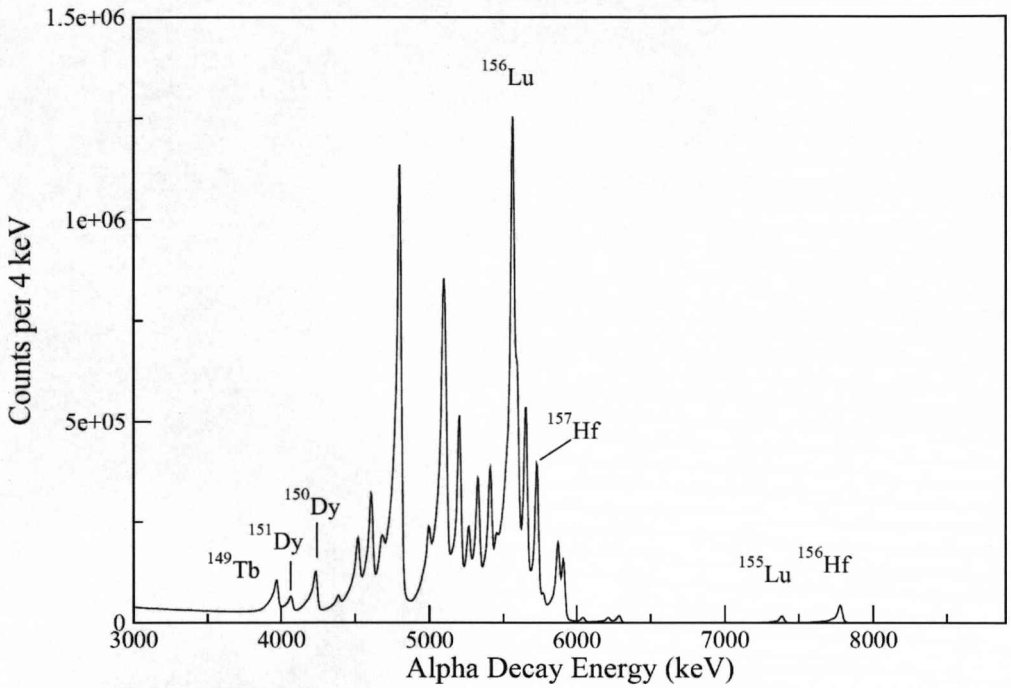

Figure 4.1: Energy spectrum showing the alpha peaks used for the DSSD calibration.

position in the histogram and the energy, therefore a linear fit was applied which covered energies interval around 5-7 MeV. For proton emission the energy falls outside this interval and a correction had to be applied. From the data acquired during the experiment two known proton emitters were identified: ^{160}Re (1261 keV) and ^{156}Ta (1107 keV). The proton energy was compared with the literature and an offset from the average of these two values was identified, and subsequently applied to any proton decays. The same triple alpha source was used for the PIN diode detector gain matching.

The planar germanium detector was gain matched in an energy range up to

~400keV and was calibrated using an external ^{133}Ba source placed in front of the DSSD detector.

The clover germanium detector was configured to measure γ rays in an energy range up to ~2.5 MeV and was calibrated using a combined source of ^{152}Eu and ^{133}Ba. The 43 JUROGAM detectors were calibrated using the known γ-ray energies from ^{152}Eu and ^{133}Ba sources which were placed at the target position.

4.2 Event identification and correlation

Most of the scattered beam and fission fragments are suppressed by the recoil separator RITU, but some are transported and implanted into the DSSD at the focal plane. To apply properly the RDT technique a clean recoil identification of the fusion-evaporation reaction residue has to be made. The first selection applied on the data was a two dimentional gate (2D gate) to separate evaporation residue ions from scattered beam and fission fragments. A two dimensional histogram was produced, representing the time of flight between the MWPC and the DSSD as a function of energy loss in the MWPC. The selection of recoil nuclei from other unwanted implantation events is made through a 2D gate applied to this histogram, as shown in Fig. 4.2.

The reaction used during the experiment (^{58}Ni + ^{108}Cd) was sufficiently asymmetric that the magnetic rigidity of the beam was very different from the fusion-evaporation products and the different components of the events implanting in the DSSD can be easily separated, see Fig. 4.2.

A second separation is made to distinguish between recoil-events and decay-events. A recoil event will pass through the MWPC, generating a signal in it while a decay event will only have a signal from the DSSD. Therefore requiring an anti-coincidence between these two detectors, it is possible to select only decay events. The correlation method is made possible by the use of two basic pieces of

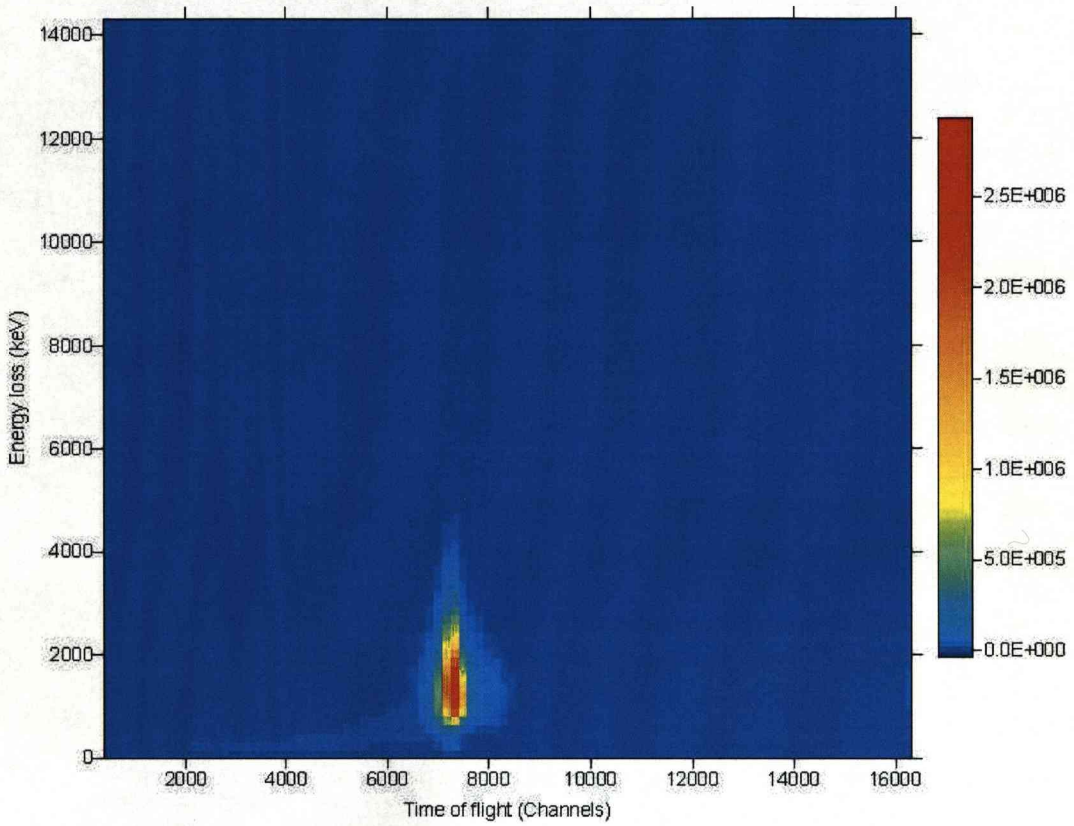

Figure 4.2: Energy loss in the gas detector vs time-of-flight between the MWPC and the DSSD.

information: the event position in the DSSD and the time at which it occurred. These data are stored and handled both on-line and off-line through the Java based analysis program GRAIN [grain], a framework developed to be used with the TDR data acquisition system. Data emerging from a TDR system are not structured or filtered in any way, apart from the timestamp ordering (10ns precision). The software enables the user to change the trigger condition according to necessity, and through the spatial and temporal information, correlated event chains can be constructed. During this experiement the trigger to define an event was a signal from any X face strip of the DSSD. It is also possible to choose the event time width, which takes into account a time window before and after the

trigger signal. Once the event is defined it is possible to look for a chain of events. This is crucial when studying decay spectroscopy because it allows a sequence of decays to be correlated and assigned to the right recoil. In the software it is

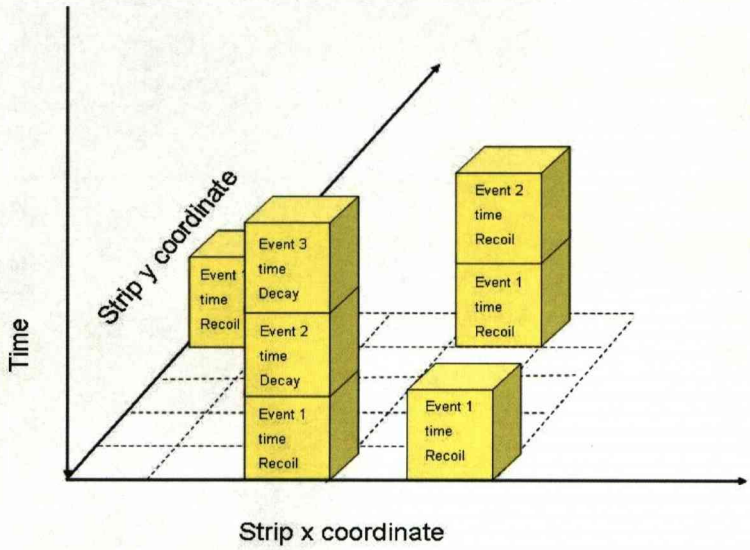

Figure 4.3: The 'tagger' GRAIN object. To create a chain of events the timestamp and position in the DSSD detector are recorded for each event. These allow spatial and temporal correlations to be chosen.

possible to define an object called 'tagger' which contains a sequence of events which can be recoil or decay events and their time stamp, see Fig. 4.3. The standard correlation procedure is to search through the tagger and look for all the events that happened in the same DSSD pixel within a certain time window and check until the corresponding recoil is found. The time window or 'search time' is normally defined as 3 times the half-life of the decay of interest.

During the correlation procedure several problems had to be addressed:

- random correlation can occur due to the electronic dead time. The main source of this dead time arises from the MWPC detector which has a counting rate of few kHz. By checking the time stamp of a recoil passing through the gas detector a dead time of $\sim$14 μs was measured. This means that any recoil passing through the MWPC within that time window will not generate a signal, and therefore will not be recognised as a recoil in the DSSD. The DSSD on the other hand has much lower counting rate of $\sim$0.5 Hz/pixel. What could happen is that the event will generate a signal in the DSSD and no signal in the MWPC, and will therefore be stored as a decay although being a recoil.

- The MWPC entrance window is slightly larger that the DSSD window, a recoil could therefore pass through the MWPC without implanting in the silicon detector. On the other hand if another recoil at the same time is passing through the MWPC and generating a signal, it could be wrongly correlated to the subsequent decay.

To try to overcome these problems the sorting code was modified. A time window was set in order to consider only events for which the time difference between the gas signal and the DSSD signal was the correct for recoils flying through the MWPC, reducing the number of random correlations. Furthermore when more than one event is stored in the tagger one needs to check that the chain recoil$\rightarrow$ decay1 $\rightarrow$ decay2$\rightarrow$ decay3... does not have any recoil intruder in between two decay events.

Fig. 4.4 shows the spectrum of α decay within 20 ms from a recoil, followed by a subsequent α decay within the same DSSD pixel in the energy range of ^{157}Ta α. Two peaks belonging to ^{155}Lu and ^{156}Hf are quite strong being randomly correlated and one can clearly see the effect before (black curve) and after (red curve) applying the correction condition.

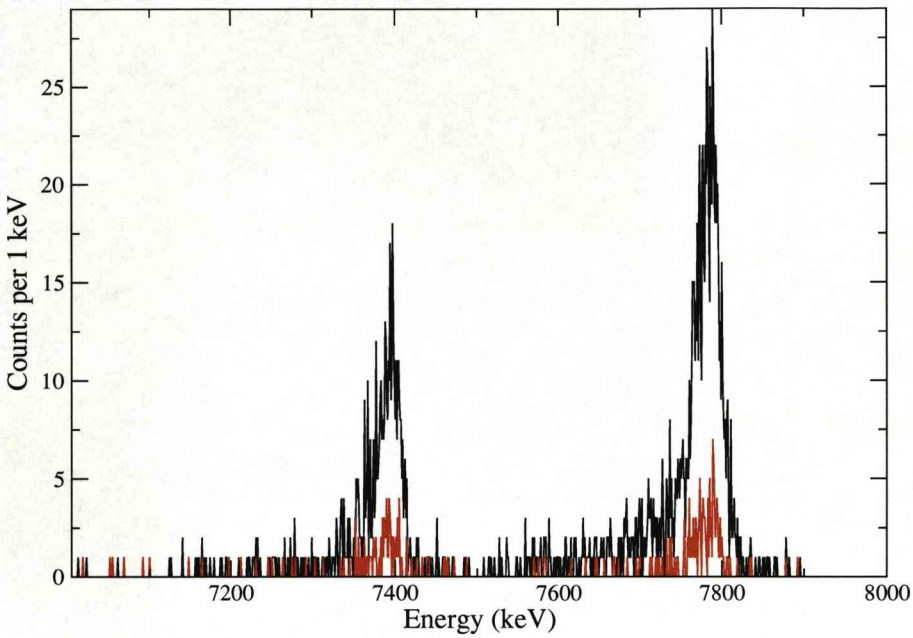

Figure 4.4: The effect of the filter applied in the sort code on the background caused by ^{155}Lu and ^{156}Hf peaks. The black line shows the spectrum before while the red line after the filter condition was applied.

4.3 Signal baseline shift correction

When a recoil is implanted in the DSSD the preamplifier will record a signal that due to the high energy will need up to 200 μs before restoring the baseline. This is due to the long exponential decay of the preamplifier signal. When dealing with a short half-life it could happen that the preamplifier signal from a decay is too close in time to the recoil signal and the baseline of the previous impulse is not fully restored. The effect is that the amplitude of the second signal suffers from an offset that should be added back to have a correct measure. To check this effect we plotted the alpha energy distribution as a function of time for a

fast decaying nucleus produced during the experiment. We can see from Figure 4.5 the alpha decay of ^{155}Lu ($t_{1/2}$ = 2.7ms) and ^{156}Hf ($t_{1/2}$=0.52ms) and it is evident from the spectrum that for times shorter than 200μs the energy curve devates towards lower energy due to the signal undershoot. We corrected this

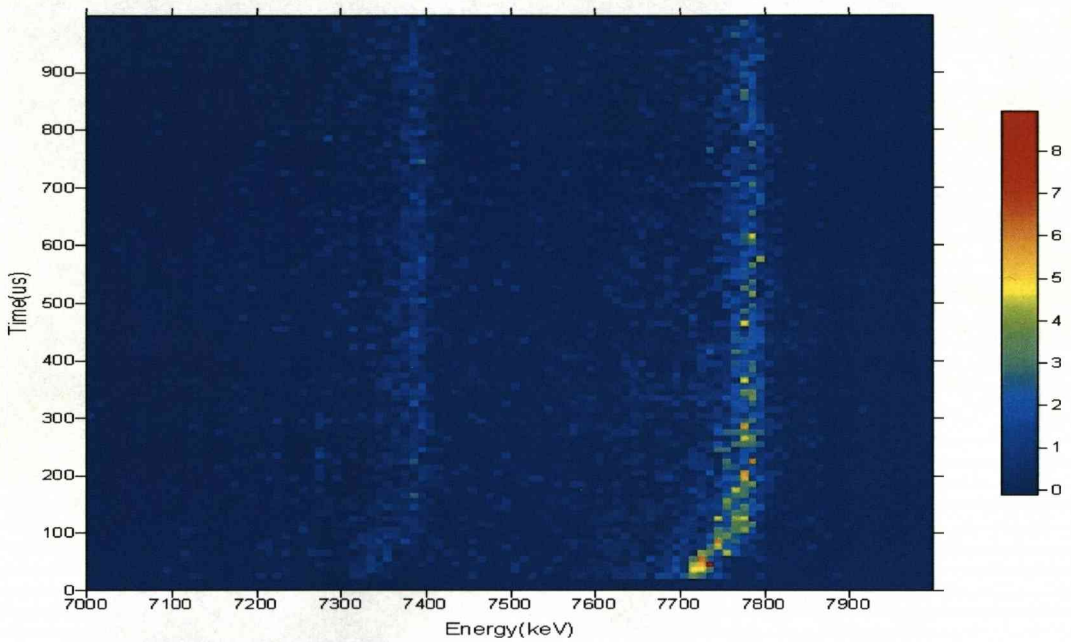

Figure 4.5: The baseline shift effect in the DSSD detector. Energy as a function of time for ^{155}Lu and ^{156}Hf.

effect offline via software, restoring the offset through a linear correction, and the effect after the correction is shown in Figure 4.6.

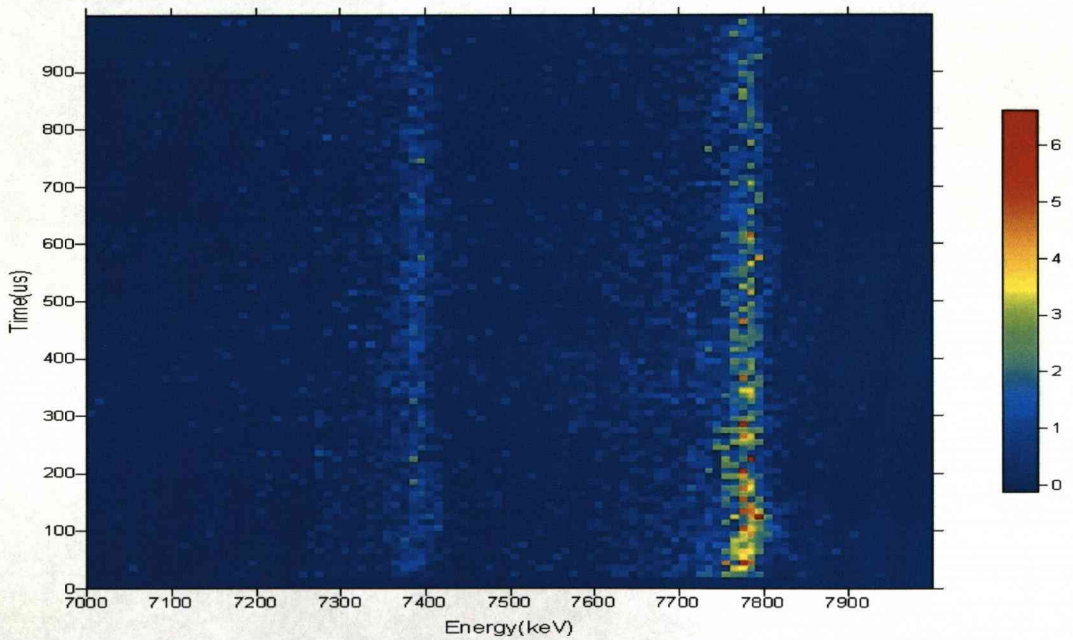

Figure 4.6: The effect of the baseline shift correction in the DSSD detector.

Chapter 5

^{161}Os α decay and ^{157}W β decay

5.1 Introduction

The lightest osmium isotope known before this experiment was ^{162}Os, which was discovered by Hofmann *et al.* in 1989 using the SHIP [Ship] velocity separator and emits 6.6 MeV α particles with a half-life of 2 ms [Hof89, Bing96, Mah00]. More recently, Joss *et al.* [Joss04] performed the first in-beam γ-ray spectroscopy experiment to study excited states in this nuclide, which was produced with a cross section of ~400 nb [Joss04]. Previously, Mahmud *et al.* searched for ^{161}Os using the FMA [Dav92] and deduced an upper limit of $\sim 2-3$ nb for the production cross section [Mah00]. Although the same reaction was employed as in this work, the beam energy was significantly lower at 270 MeV, and no ^{161}Os was observed.

The nuclides ^{161}Os and ^{157}W have 23 fewer neutrons than their lightest stable isotopes. The N = 82 shell closure has a profound influence on the occurrence of α decay in this region of the nuclear chart through its effect on α-decay Q-values, which are predicted to drop by ~1.8 MeV for even-Z N = 83 isotones compared with their N = 84 isotopes [MNK]. Consequently, ^{161}Os is expected to be the lightest α-decaying odd-A osmium isotope, while ^{157}W is expected to β decay.

In the region beyond the proton drip line above N = 82, the structure of nuclei is governed at low spin and excitation energy by valence neutrons in the $f_{7/2}$ and $h_{9/2}$ orbitals and protons in the $s_{1/2}$, $d_{3/2}$ and $h_{11/2}$ orbitals [Woods97]. An interesting feature of this region (see ref. [Ding]) is the rapid drop in energy of the $\nu h_{9/2}$ neutron states relative to the $\nu f_{7/2}$ states above the Z = 64 subshell. Below Z = 64 protons occupy the $\pi g_{7/2}$ and $\pi d_{5/2}$ orbitals. Above Z = 64 these orbitals are full so the occupation probability of the $\pi h_{11/2}$ orbital becomes significant and the interaction with the $\nu h_{9/2}$ and $\nu f_{7/2}$ states starts having an effect. The lowering of the $\nu h_{9/2}$ relative to the $\nu f_{7/2}$ states should be reflected in the decreasing energy difference between $9/2^-$ and $7/2^-$ levels that is shown in fig. 5.1. The lightest N

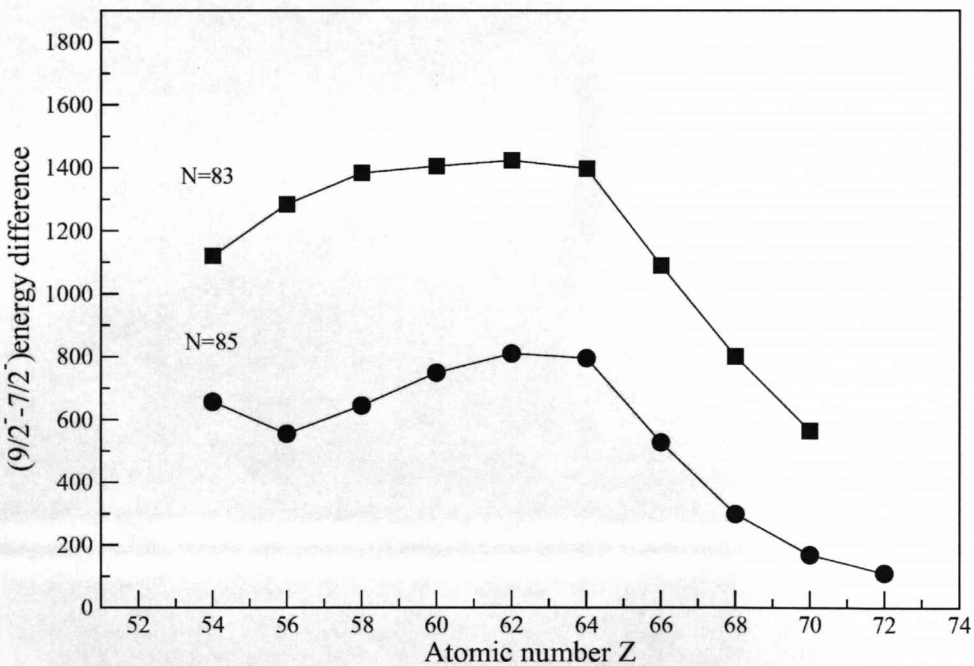

Figure 5.1: Experimental energy difference between $7/2^-$ and $9/2^-$ states for N=83 (filled squares) and N=85 (filled circles) isotones, values are taken from ref. [Toth79, Piip79, Piip81, Ding, McNei89, Foin82, Urban02, Urban96].

= 85 isotone for which this energy difference is known is $^{157}_{72}$Hf, where the value is 111 keV [Saad95].

The ground state of $^{159}_{74}$W, is expected to be a $\nu f_{7/2}$ state because the proton decay of $^{160}_{75}$Re to ^{159}W shows no sign of hindrance due to a change in neutron configuration, fitting in with the regular behaviour of proton emission from states formed by coupling a $d_{3/2}$ proton with an $f_{7/2}$ neutron [Page92, Page96, Dav97]. The ground-state configurations of even heavier N = 85 isotones, such as $^{161}_{76}$Os, are an interesting question, as are those of the N = 83 isotones, such as ^{157}W, although the $9/2^-$ states lie somewhat higher in excitation energy. In both cases, the radioactive decay properties will be influenced by the quantum numbers of the unpaired neutron.

The ground state assignment of odd-A nuclei still poses a major challange to nuclear theories. The lowest nuclear state for odd-A nuclei within the nuclear shell model is predicted to be [Nord49] the one occupied by the odd nucleon, and this should be in the lowest energy orbital not completely filled. Recent global microscopic calculations of ground-state spins and parities for odd-mass nuclei by Bonneau *et al.* [Bonn07] show how the results of Skyrme-Hartree-Fock-BCS calculations of ground state spins and parities have an agreement with experimental values that oscillate between 54.4% and 66.4%, in the case of spherical and well-deformed odd-mass nuclei, respectively. Is clear that ground state spins of exotic nuclei provide a stringest test of nuclear models.

5.2 Results

Alpha-decay properties were investigated for the first time for ^{161}Os. The present experiments were performed at the Accelerator Laboratory of the University of Jyväskylä. The ^{161}Os nuclei were populated in the ^{106}Cd(^{58}Ni,3n) reaction. The target was a 1.1 mg/cm^2 thick, self-supporting ^{106}Cd foil of 96.5 % isotopic en-

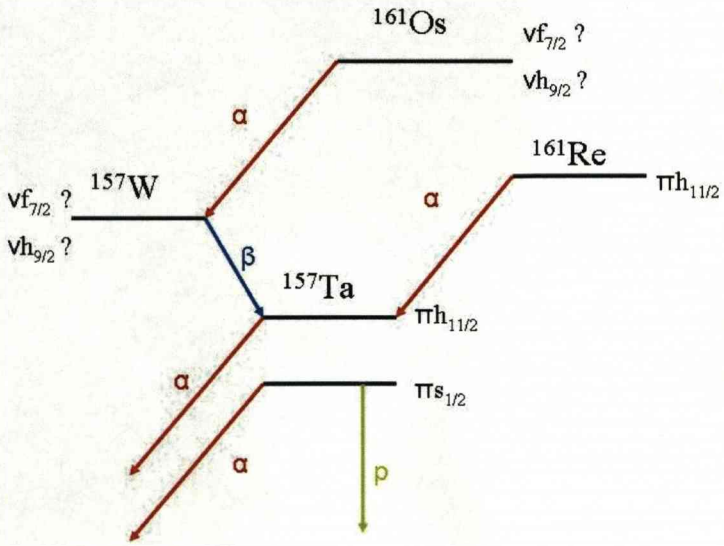

Figure 5.2: Decay scheme of ^{161}Os. Levels involved are assigned when known, for ^{161}Os and ^{157}W two possible ground state are shown.

richment. Average beam currents and irradiation times were 2.3 pnA for 104 hours at a beam energy of 290 MeV, 4.7 pnA for 75 hours at 300 MeV and 3.0 pnA for 96 hours at 310 MeV. The decay scheme of ^{161}Os is presented in Fig. 5.2. In Fig. 5.3 all the alpha decays within 4 ms are shown. Several peaks belonging to nuclei in the region are present and to separate the ^{161}Os α decays from the large number of counts in this spectrum, correlations were sought with the α decay of ^{157}Ta, which is populated via the ^{157}W β, see Fig. 5.2.

The β-particle detection eficiency is not well known therefore the analysis code took into account the possibilities that the ^{157}W β particle was either detected or escaped the pixel without interacting. Two α-decaying states are known in

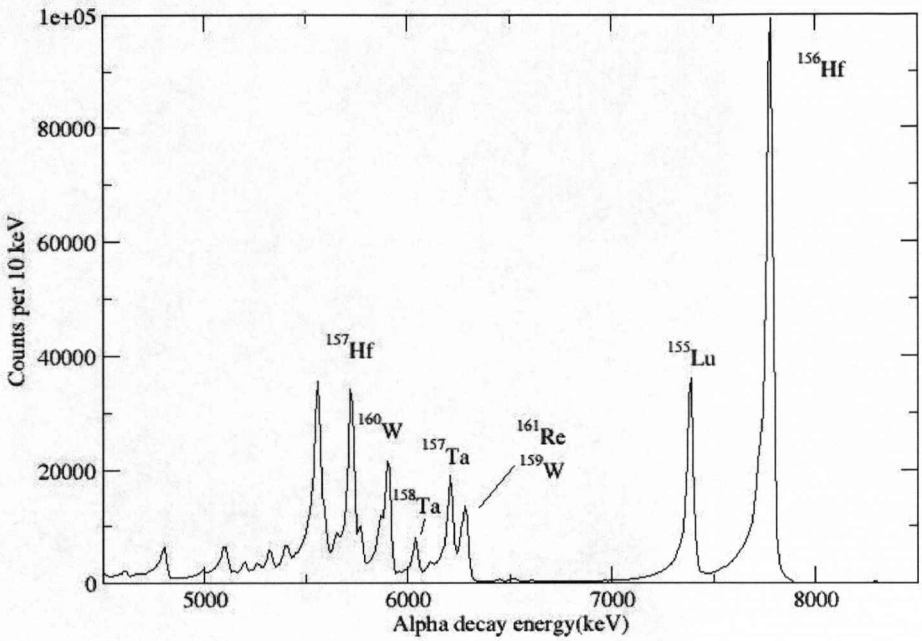

Figure 5.3: Energy spectrum of all decays occurring within 4 ms of an ion implantation into the same DSSD pixel.

^{157}Ta, one of which also has a 3.4 % proton decay branch [Irvine97]. The $\pi h_{11/2}$ state decays solely by emitting 6213 keV α particles with a half-life of 4.3 ms [Page96], while the $\pi s_{1/2}$ ground state has a half-life of 10.1 ms and emits 927 keV protons and 6117 keV α particles [Irvine97]. Fig. 5.4 shows the energy spectrum of decays that are followed within 4 s by either ^{157}Ta α decay. The strongest peak in this spectrum is the 6.27 MeV α-decay line of the $\pi h_{11/2}$ state in ^{161}Re, which populates the corresponding state in ^{157}Ta and has a half-life of 16 ms [Page96, Irvine97]. The peak at 6.5 MeV is attributed to ^{163}Os α decays correlated with those of ^{159}W, the low-energy tail of whose 6.3 MeV α-decay line extends into the ^{157}Ta energy gate, while the peak at 6.1 MeV arises from

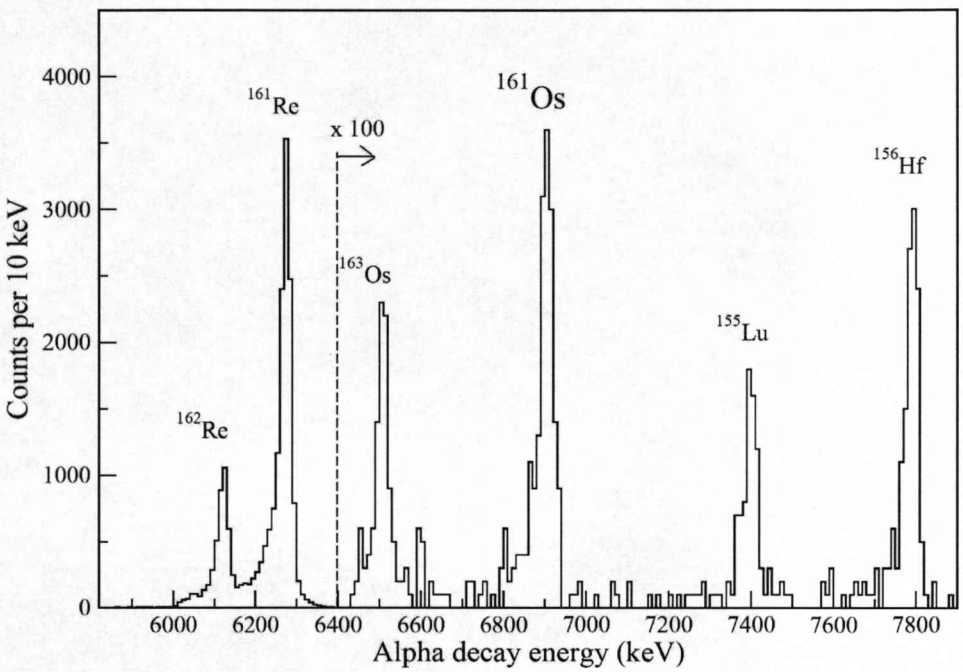

Figure 5.4: Same as fig. 5.3 but with the additional requirement that the α decay is followed within 4 s by either of the α decay branches of ^{157}Ta

^{162}Re α decays correlated with the 6.05 MeV α decays of ^{158}Ta, which also falls within the ^{157}Ta energy gate. The ^{155m}Lu and ^{156m}Hf peaks at 7.4 MeV and 7.8 MeV, respectively, can be understood as arising from random correlations. The clear peak comprising over 200 counts at 6890 $\pm$ 12 keV is a new activity that is assigned as the α decay of ^{161}Os. In order to extract the half-life of this new activity, the time difference between the implantation of each recoil and its subsequent alpha decay was measured for the $\approx$200 counts in the peak. The maximum likelihood method takes the mean time difference to be the mean lifetime [Schmidt84]. In this case, the average dead time following implantation was 13 μs and has to be corrected for, so this was subtracted from the mean value. The error values were estimated using Poisson statistics [Schmidt84]. The half-

life was also calculated using the maximum likelihood method implementation developed by Meyer [Meyer75], which corrects for the discrete bin width and also for the finite measurement period. The error bars were calculated using a "score function", which comes from the derivative of the likelihood function.

The maximum likelihood method is known to be sensitive to background counts occurring at long time differences which distorts the mean value. The data were therefore analysed by successively removing the longest time difference to see what effect this had on the half-life. The range of plausible half-life values from the fit was included as a contribution to the error bars. A half-life of 640 $\pm$ 60 μs was adopted after considering all the results of this analysis.

Fig. 5.5 shows the energy spectrum of ^{157}Ta α decays that follow the ^{161}Os α decays within 4 s. From this spectrum it is evident that both α-decaying states in ^{157}Ta are fed with comparable intensities by the β decay of ^{157}W. If a $\nu h_{9/2}$ state were the ground state of ^{157}W then one would expect the β decay to proceed mainly to the $\pi h_{11/2}$ state in ^{157}Ta through a favoured Gamow-Teller transition. However, if the ground state were a $\nu f_{7/2}$ state, then both ^{157}Ta states would be populated with similar probability through intermediate states. Since this is exactly what is observed for ^{157}W, it is proposed that a $\nu f_{7/2}$ state represents its ground state. The same conclusions can be drawn from the case of the β decay of the isotone ^{155}Hf where ^{156}Ta proton decays are correlated with the α decays of both low-lying states in ^{155}Lu [Page96]. The half-life of ^{157}W was deduced from the measured time differences between the α decays of ^{161}Os and ^{157}Ta, taking into account the lifetimes of the ^{157}Ta states. The resulting half-life of 270 $\pm$ 25 ms obtained using the method of maximum likelihood is consistent with the predicted value of 209 ms [MNK].

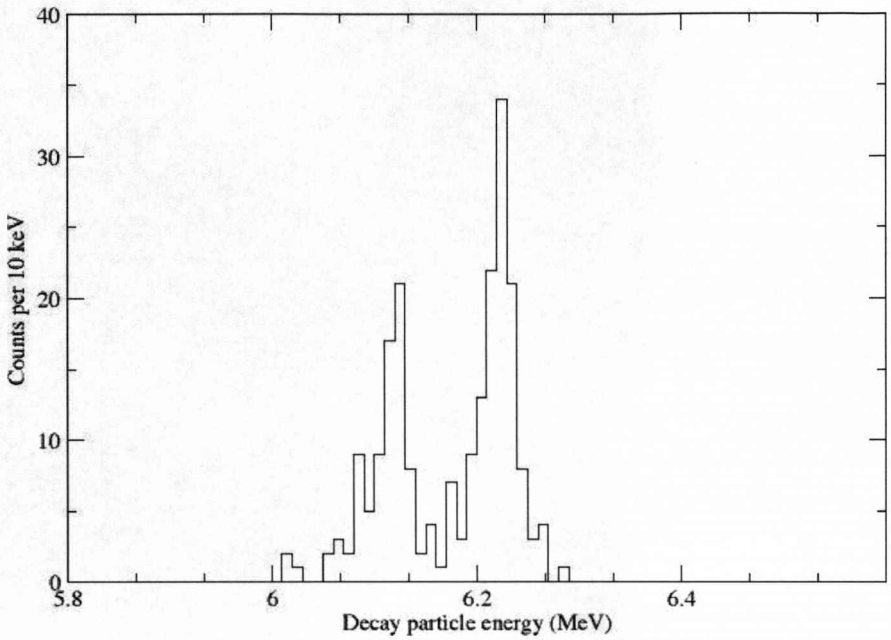

Figure 5.5: Energy spectrum of ^{157}Ta α decays following α decays in the ^{161}Os peak.

5.2.1 Fine structure in ^{161}Os

The observation of fine structure in the α decay of ^{161}Os can confirm its ground-state configuration, as can be seen from the calculated branching ratios shown in Fig. 5.7. One experimental difficulty is that in the expected energy region around 300 keV (see fig. 5.1) there is potentially interference from α decays of ^{163}Os to ^{159}W (see fig.5.4), which has a half-life of 8.2 ms [Page96]. To circumvent this source of background, only decays appearing in Fig. 5.4 that were followed more than 50 ms later by a ^{157}Ta α decay were considered and reduced maximum correlation times of 2 ms and 2 s were applied.

The resulting spectrum is shown in Fig. 5.6, in which a group of counts at 6580 $\pm$ 30 keV can be seen. These counts are assigned as the fine structure in

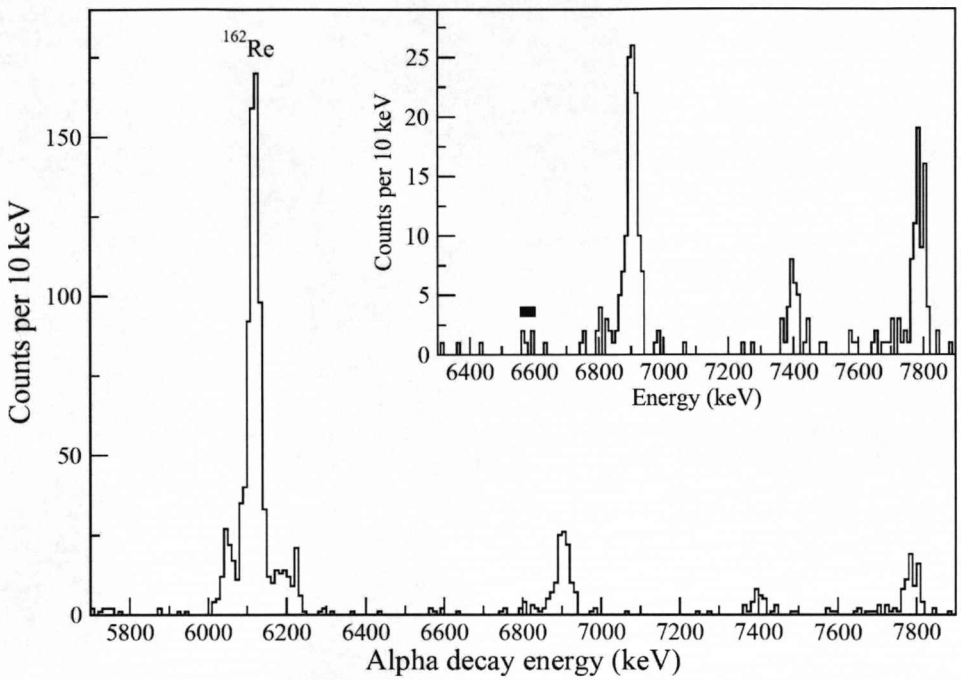

Figure 5.6: Spectrum of α decays occurring within 2 ms of an ion implantation into the same DSSD pixel that are followed between 50 ms and 2 s later by either of the α-decay branches of ^{157}Ta. The inset shows the region around 7 MeV and the black rectangle indicates ^{161}Os α-decay fine structure.

^{161}Os populating the $9/2^-$ state in ^{157}W. The corresponding excitation energy of 318 ± 30 keV in ^{157}W is plotted in Fig. 5.12 and follows the trend of decreasing the energy difference between $9/2^-$ and $7/2^-$ states. The branching ratio for this activity was $3.8^{+2.22}_{-1.6}$% and these values are consistent with an $f_{7/2}$ ground state in ^{161}Os (see Fig. 5.7).

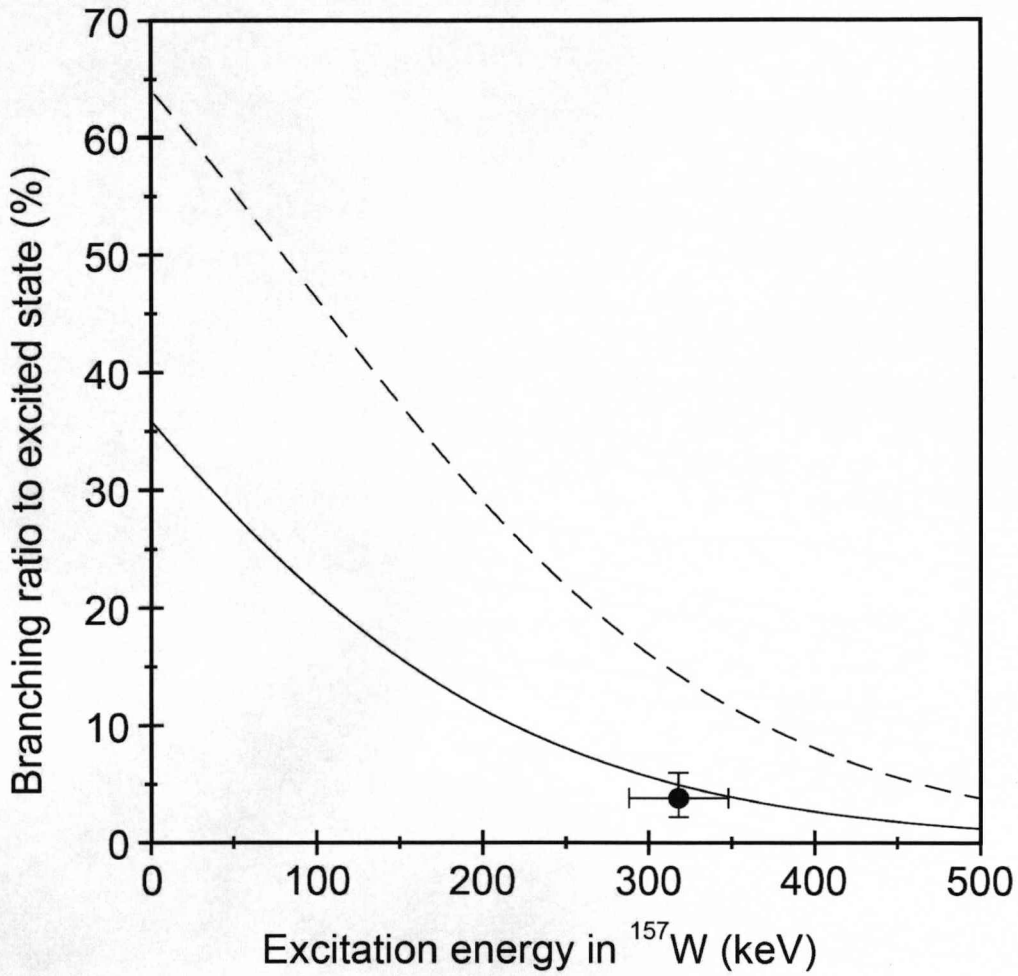

Figure 5.7: Calculated branching ratios for ^{161}Os α decay to the first excited $9/2^-$ state in ^{157}W as a function of its excitation energy above the $f_{7/2}$ ground state. The dashed curve is for an $h_{9/2}$ ground state in ^{161}Os, while the solid line is for an $f_{7/2}$ ground state. The same reduced width has been assumed in all calculations, which used the method of Rasmussen [Ras59]. The filled circle indicates the measured value from the present work.

5.3 Interpretation

The α-decay Q-value of 7066 $\pm$ 12 keV measured for ^{161}Os from the present work is included in fig. 5.8. The value for ^{161}Os fits in with the trends with no significant deviation that could be an indication of a change from a $\nu f_{7/2}$ to a $\nu h_{9/2}$ ground state. Furthermore, the Q-value for ^{161}Os is in excellent agreement with the predicted value of 7.03 MeV [MNK].

In order confirm the assignment of the ^{161}Os ground state is useful to look at the reduced width systematics for even Z nuclei in the same region. The predicted partial half-life for β decay of ^{161}Os is in excess of 100 ms [MNK], so it is assumed that α-particle emission is the only significant decay branch. From the measured

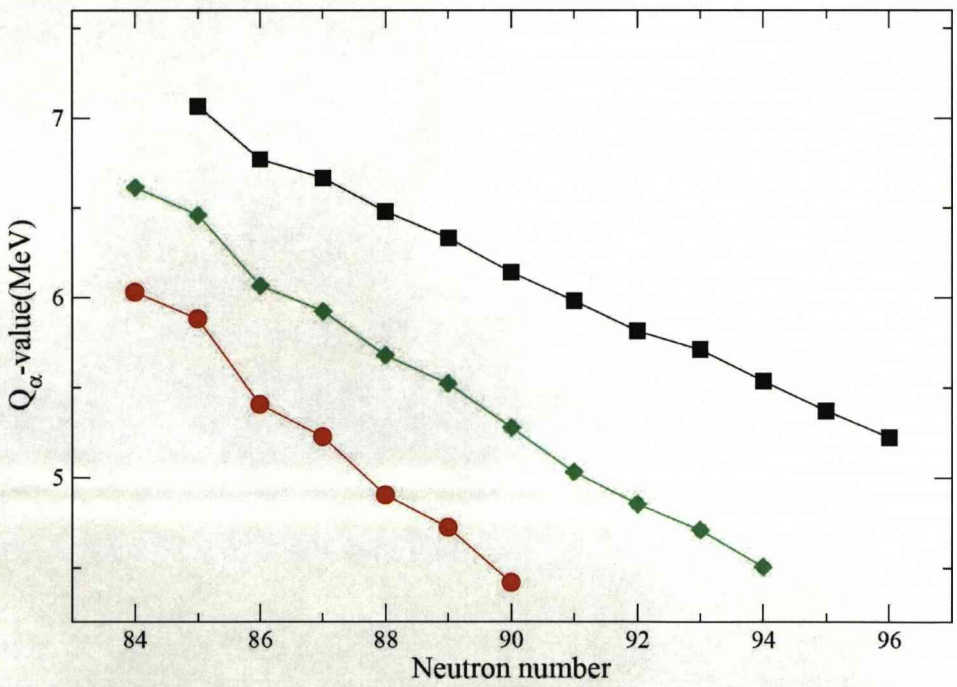

Figure 5.8: Alpha-decay Q-value systematics for the Os (squares), W (diamonds) and Hf (circles) isotopes.

α-decay energy and half-life, the reduced α-decay width of ^{161}Os was calculated to be 37 $\pm$ 5 keV using the method of Rasmussen [Ras59], assuming s-wave emission. Although the reduced widths for odd-A nuclei are generally below those of even-even nuclei, this value for ^{161}Os is somewhat lower than values deduced for the heavier odd-A osmium isotopes that are shown in fig. 5.9. This plot includes the

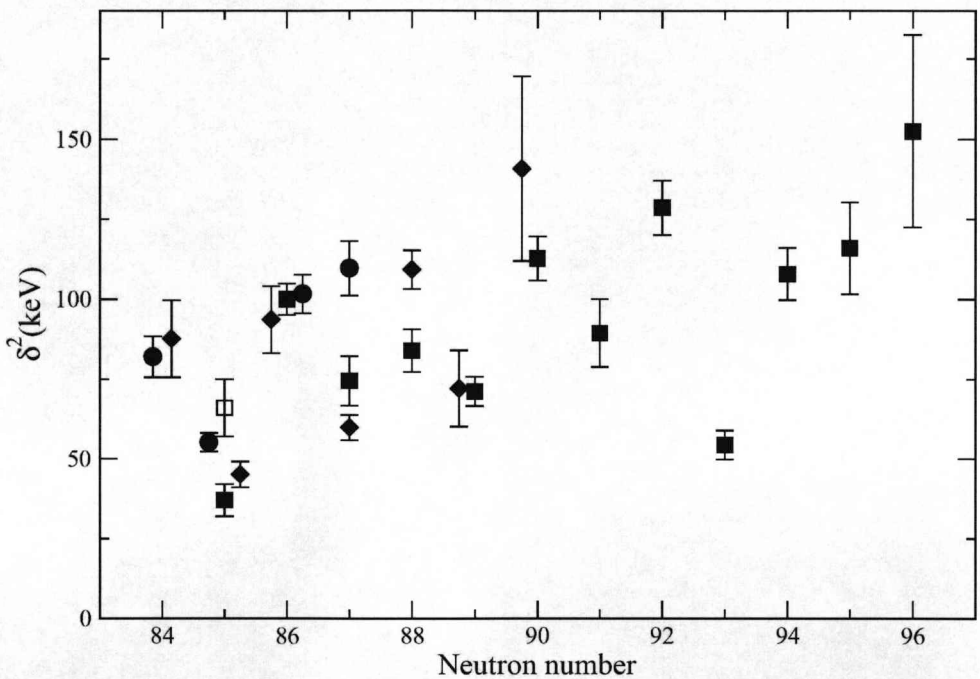

Figure 5.9: Reduced α-decay widths (δ^2) for Os (squares), W (diamonds) and Hf (circles) nuclei, calculated using the method of Rasmussen [Ras59] assuming s-wave α-particle emission. Some data points are displaced slightly from their true neutron number for clarity of presentation.

values deduced using the more precise branching ratios determined for $^{164-166}$Os in this work. The reduced width for ^{161}Os would become 66 $\pm$ 9 keV assuming d-wave emission, which would be the case if the ground state of ^{161}Os were a $\nu h_{9/2}$ state, rather than $\nu f_{7/2}$. This is more in line with values for heavier isotopes,

but it is important to note that the reduced widths for the N = 85 isotones are generally lower, as can be seen from the trends for W and Hf nuclei that are also plotted. Fig. 5.10 shows the difference between the reduced widths calculated for Os and W isotones. From this it is clear that the present data are compatible

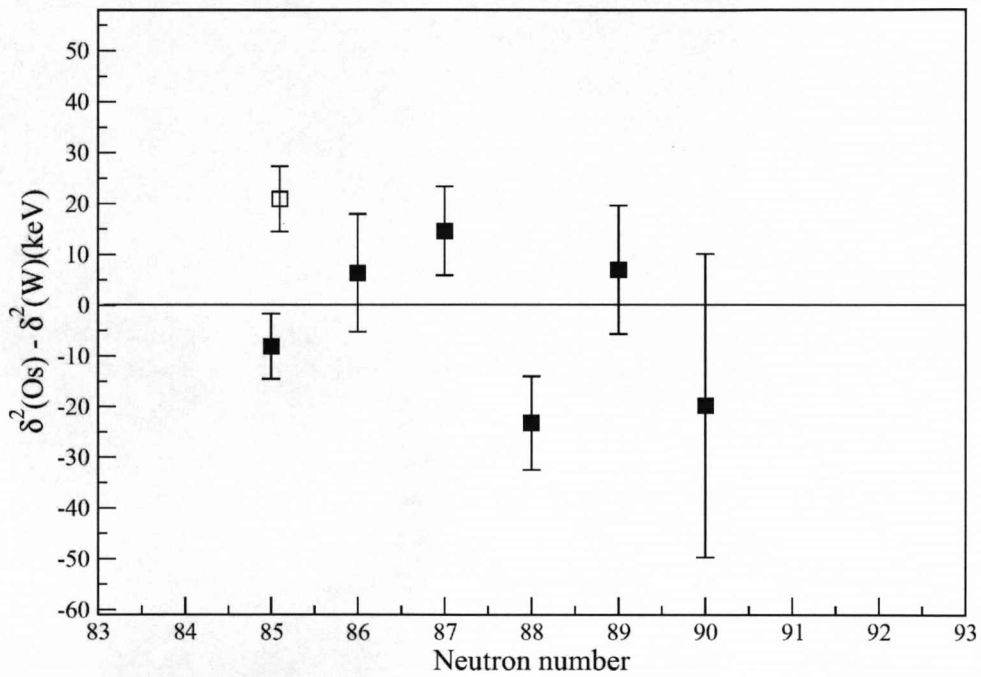

Figure 5.10: Difference between reduced α-decay widths of Os and W isotones assuming s-wave α-particle emission. The calculated value for ^{161}Os assuming d-wave α-emission is plotted with the open symbol for comparison. The data are from [Page96, Hof89, Bing96, Joss04, Mah00, Hof81, Rytz91, Kett04, Meissner, Hof79, Schrewe, Toth83, Toth73] and the present work.

with an s-wave α decay, indicating that the ground state of ^{161}Os, like ^{157}W, probably comprises an unpaired neutron in an $f_{7/2}$ state, in agreement with the observation of α-decay fine structure.

5.3.1 Discussion

The study of nuclei far from the line of β stability allows new features of the inter-nucleon forces that govern the properties of atomic nuclei to be investigated. For example, dramatic changes in the shell structure have been discovered in neutron-rich light nuclei. One proposed mechanism for these changes is the interaction between nucleons occupying states in $J_{>,<} = l \pm 1/2$ and neutrons in $J_{>,<} = l \pm 1/2$ as described in Ref. [Ots05] (see fig. 5.11), shifting the relative energies of specific orbitals depending on their occupancy.

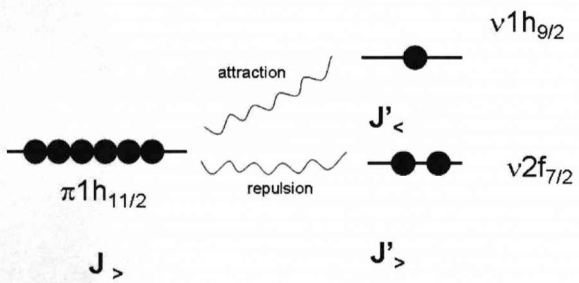

Figure 5.11: Schematic repesentation of the force produced by the tensor interaction between protons in $J_{>,<} = l \pm 1/2$ and neutrons in $J_{>,<} = l \pm 1/2$ as described in Ref. [Ots05], for the ^{161}Os case.

This leads to variations in the energy gaps between orbitals as the nucleon numbers change [Ots01, Ots05]. These interactions could also play a significant role in determining the structure of much heavier nuclei [Col07]. Interactions between nucleons occupying the $h_{11/2}$ and $h_{9/2}$ orbitals would lower the energies of these orbitals. Comparatively large shifts could be expected for these high-j

orbitals with large spatial overlaps. These expectations are supported by the Hartree-Fock calculations [ESuc] shown in Fig. 5.12 of the energy difference between $\nu h_{9/2}$ and $\nu f_{7/2}$ orbitals for N = 82 isotones using the three commonly used Skyrme parameterisations Sly5 [Chab98], SkM* [Bart82] and SkI4 [Rein95].

All three calculations predict that the energy difference decreases as Z increases, until the Z = 82 shell closure is reached. The addition to each of these Skyrme forces of a tensor term with coupling strengths of U=-408 MeV fm^5 and T=888 MeV fm^5 [Col07] steepens the gradients, at least to Z = 76, suggesting the possibility of an inversion of the $\nu h_{9/2}$ and $\nu f_{7/2}$ orbitals. The energy difference between the $\nu h_{9/2}$ and $\nu f_{7/2}$ orbitals should be reflected in the energy differences between 9/2- and 7/2- states in odd-N, even-Z nuclei just above N = 82. In Fig. 5.12 the experimental data and theoretical predictions are overlapped and the new assignment from this work for the excitation energy of the $9/2^-$ state in ^{157}W is added and it is evident that the tensor component is essential in order to reproduce even the the sign of the slope correctly on both sides of N = 64.

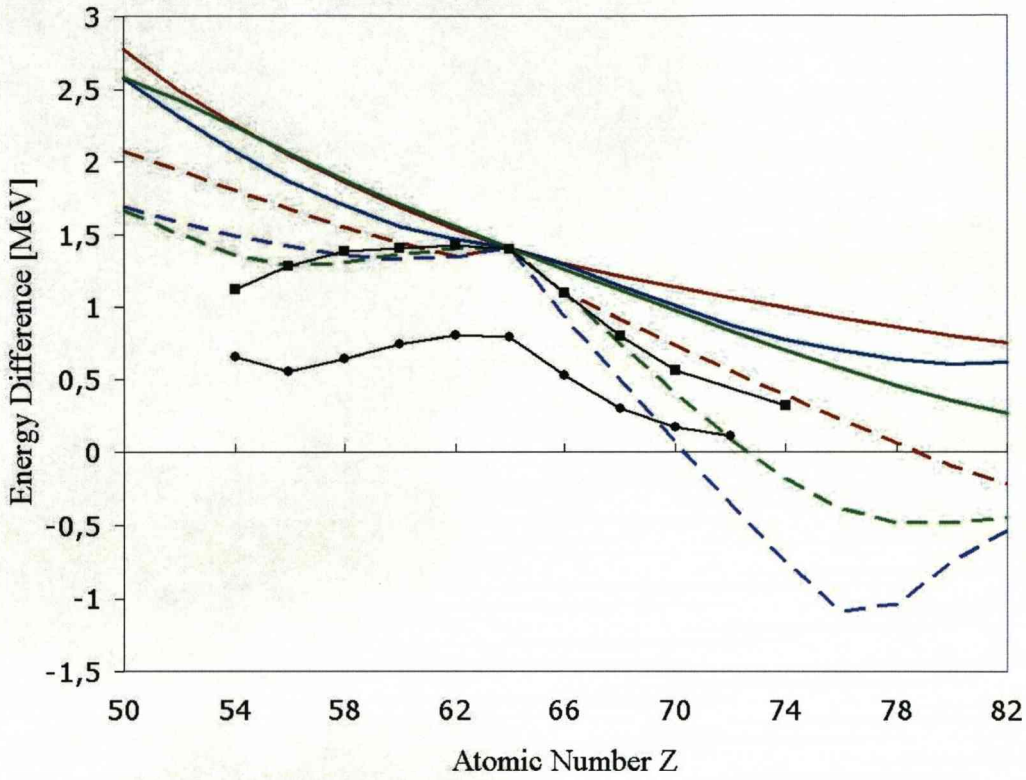

Figure 5.12: The measured energy difference between lowest-lying $9/2^-$ and $7/2^-$ states for N = 83 (filled circles) and N = 85 (filled squares) isotones compared with (color on-line) calculated energy difference between the $\nu f_{7/2}$ and $\nu h_{9/2}$ orbitals N = 82 isotones. The value for ^{157}W from the present work is shown at Z = 74. The calculations were performed using the Hartree-Fock method for the Skyrme forces Sly5 [Chab98] (solid red line), SkM* [Bart82] (solid greed line) and SkI4 [Rein95] (solid blue line). The addition of a tensor term with coupling strengths of U=-408 MeV fm^5 and T=888 MeV fm^5 [Col07] to each of these Skyrme forces results in the corresponding dashed lines. The calculations are normalized to the energy difference of 1.397 MeV measured for ^{147}Gd [Klein79].

Chapter 6

α decay of ^{159}Re and proton emission from ^{155}Ta

6.1 Introduction

The push to extreme values of isospin has resulted in the discovery of many new nuclides beyond the proton drip line, where decay spectroscopy has proved to be a highly effective tool for extracting detailed information about the structure of proton-emitting nuclei [Hofmann89, Woods97, Bla08]. For proton emitters below the N = 82 neutron shell closure, where β decay is the main competing decay process, the identification has relied on their relatively short half-lives which allows temporal and spatial correlations with the parent nuclei implanted into double-sided silicon strip detectors (DSSDs) deployed at the focal plane of a recoil separator. The fine segmentation of the DSSDs suppresses the background from the β particles [Page94], while the ratio of the mass of the implanted ion to its ionic charge state combined with the systematic behaviour of proton separation energies can allow an unambiguous assignment of the proton decay to a specific nuclide.

Using this approach, important information about the deformation and single

particle structure of these extremely neutron-deficient nuclides has been deduced [Gint03, Woods04].

Proton-emitting nuclei have also been extensively studied in the region above N = 84, where α decay can occur as a significant competing decay mechanism. Although α emission reduces the yield of proton peaks when the decays emanate from the same state and can also give rise to significant background at energies where proton lines occur, α decays do provide the opportunity for correlating proton emitters' decay chains. Consequently, even very weakly produced decay lines can be identified and their decay properties established with confidence. This reliable and sensitive method of correlating with α decays has allowed a large number of cases of proton emission to be studied, resulting in extensive systematics of relative energies of single-particle orbitals and proton spectroscopic factors of nuclei in this region [DJoss06, Dav97].

Nuclei in the intermediate zone just below N = 84 represent particularly difficult cases for proton decay studies because correlations with subsequent α decays are delayed by the β decays of intermediate nuclides. Furthermore, less neutron-deficient isobars can undergo α decay with short half-lives. This leads to a situation where it is difficult to isolate the proton decays from the background arising from escaping α particles through correlations with the implanted ions. In addition, correlations with the β-decaying descendants are so slow that significant background from random correlations can render the peaks unobservable.

6.1.1 Previous work

A prime example of just such a difficult case is the proton decay of the N = 82 nuclide ^{155}Ta studied using the Fragment Mass Analyzer at the Argonne National Laboratory [Uusi99]. The background in that case arose from the 7.39 MeV α decays of an isomeric state in ^{155}Lu that has a half-life of only 2.71 ms [Page96]

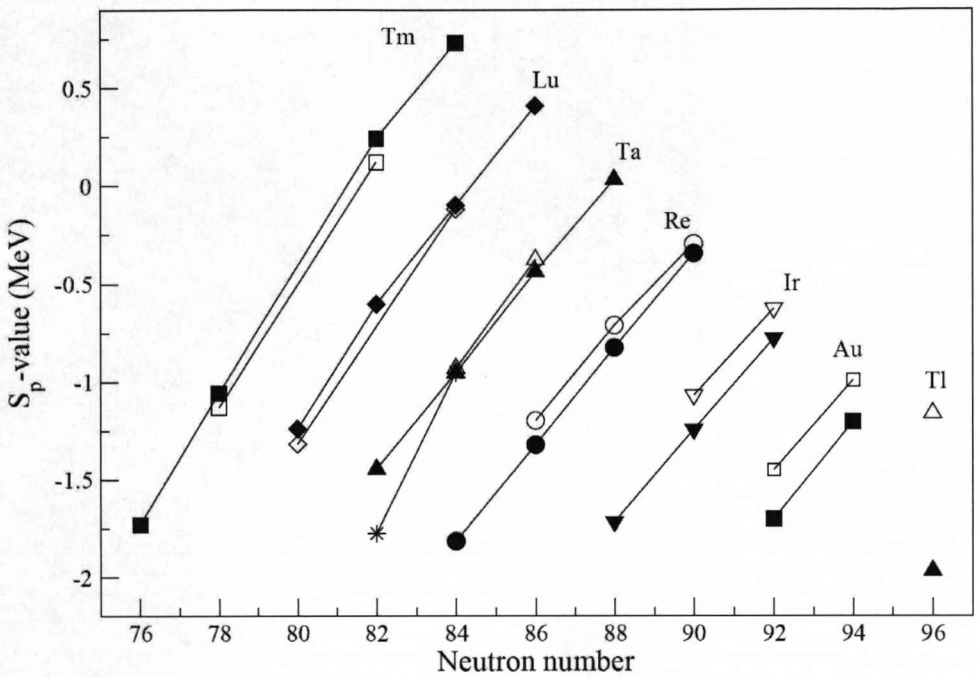

Figure 6.1: Measured S_p-values of odd-Z, even-N nuclides of elements between Tm and Tl. The asterisk represents the ^{155}Ta value from [Uusi99]and the filled triangle is taken from the present work. Filled symbols correspond to the $\pi h_{11/2}$ states, while open symbols represent the $\pi s_{1/2}$ states and the error bars are smaller than the size of the plotted symbols. Solid lines connect values for the same odd-proton configuration in a given isotopic chain.

and was produced very strongly as an evaporation residue. To suppress this background, a spectrum was obtained by selecting only decay events that occurred within 30 μs of an ion implant in the same DSSD pixel and were followed by an α decay of the great granddaughter ^{154}Yb (see Fig. 6.2). This second correlation stage is extremely difficult because the average time interval between any proton decay and the subsequent ^{154}Yb α decay is over 5 s [Page96, Hof81, Vier88]. The peak in this final spectrum was assigned as the proton decay of ^{155}Ta and

comprised six counts at an energy of 1765 $\pm$ 10 keV. Even with such stringent correlation conditions for the first decay, significant levels of background are still evident in the spectra [Uusi99]. Although the reported decay energy and half-life

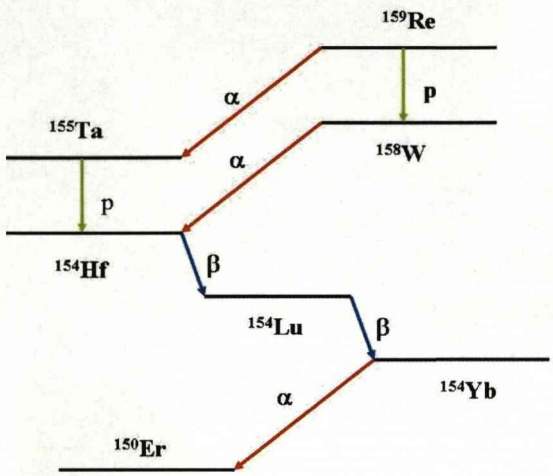

Figure 6.2: Decay paths originating from the $\pi h_{11/2}$ state in ^{159}Re.

for ^{155}Ta are compatible with emission from a $\pi h_{11/2}$ orbital, the reported proton separation energy of -1776$\pm$10 keV for ^{155}Ta [Uusi99] clearly deviates markedly from the monotonic variation of the S_p-values as a function of neutron number shown in Fig. 6.1. The anomaly cannot be attributed to the N = 82 shell closure, because no corresponding effect is seen for the Tm or Lu isotopic chains. This deviation is even more striking in Fig. 6.3, where the differences in S_p-values of the isotones of adjacent odd-Z nuclides [e.g., $S_p(^{153}\text{Lu})$- $S_p(^{155}\text{Ta})$] are plotted.

From these plots, it appears that there is a discrepancy of $\sim$300 keV in the S_p-value for ^{155}Ta. The recent discovery of proton emission from a $\pi h_{11/2}$ orbital by ^{159}Re [DJoss06] also raises questions about those previously reported results for ^{155}Ta [Uusi99]. In particular, it is possible to deduce the α-decay Q-value for ^{159}Re, assuming the α decay feeds the reported proton-emitting state in ^{155}Ta,

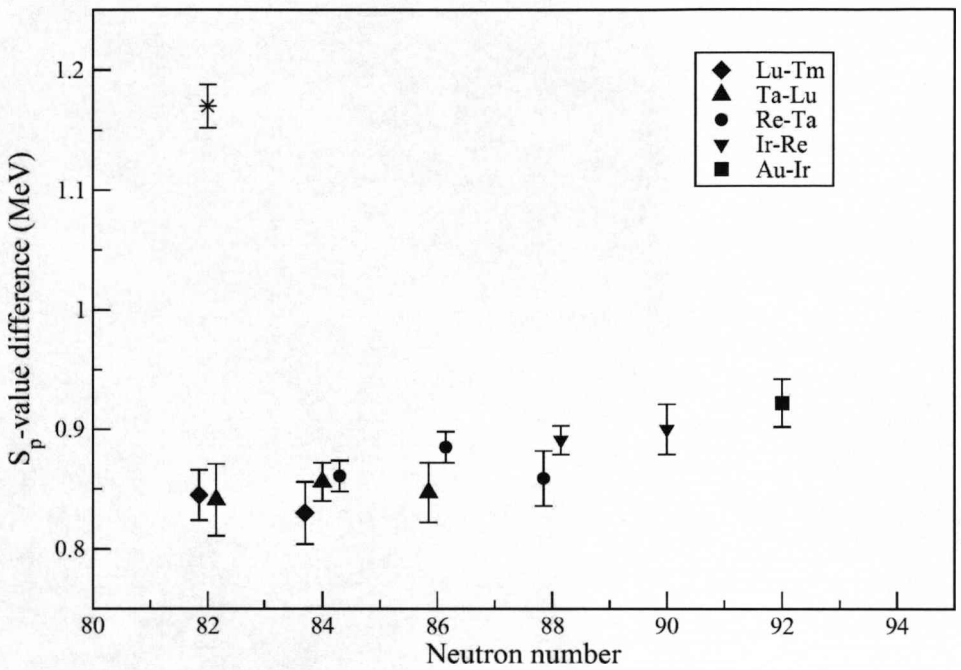

Figure 6.3: Differences in the S_p-values for $\pi h_{11/2}$ states of isotones of consecutive odd-Z elements. The value of $S_p(^{153}Lu).S_p(^{155}Ta)$ calculated using the value for ^{155}Ta from Ref. [Uusi99] is plotted with the asterisk symbol while the value deduced from the present work is represented by the large filled triangle. In cases where more than one data point can be determined for a given isotone, the points are displaced slightly from the true neutron number for clarity of presentation.

since $Q_\alpha(^{159}Re) = Q_\alpha(^{158}W) - S_p(^{159}Re) + S_p(^{155}Ta) = 6652 \pm 23$ keV [DJoss06, Uusi99, Mah00]. This value appears to be anomalously low compared with the systematics of Q_α-values plotted in Fig. 6.4 and is in fact even smaller than the value of 6711 $\pm$16 keV measured for the neighboring isotope nearer stability, ^{160}Re [Page96]. Such a low value is hard to explain and casts further doubt on the assignment of the peak observed in ref. [Uusi99] to the proton decay of the lowest-lying $\pi h_{11/2}$ state in ^{155}Ta.

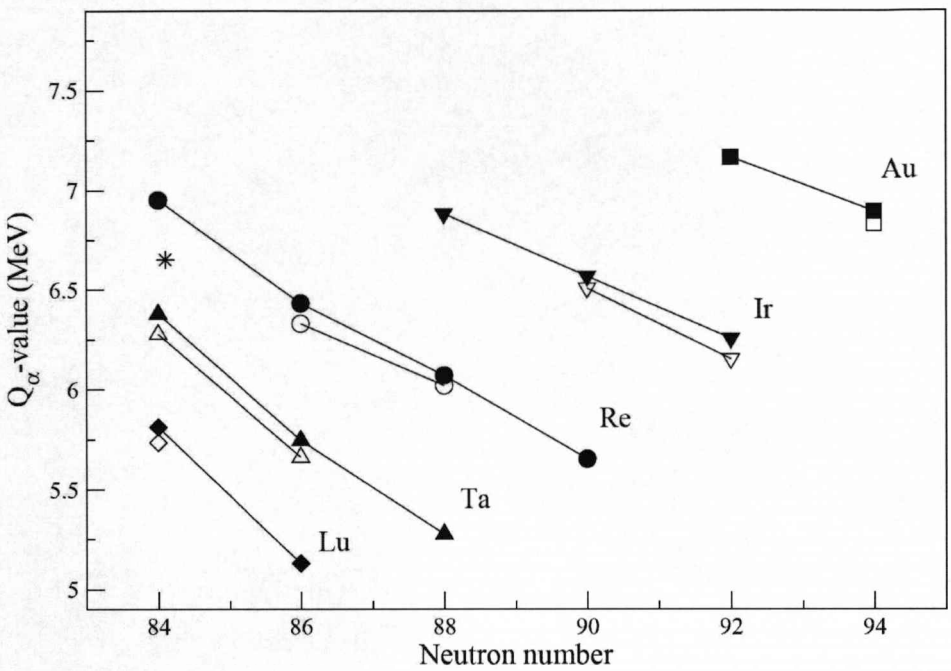

Figure 6.4: Measured α-decay Q-values of odd-Z, even-N nuclides. The asterisk represents the value deduced from Q_α-value for ^{158}W [Mahmud] and the S_p-values for ^{155}Ta [Uusi99] and ^{159}Re [DJoss06]. The Q-value measured for ^{159}Re in the present work is denoted by the large filled circle. Other data are taken from Refs. [Woods97, Dav97, Page96, Batchelder, Bingam, Irvine97, Robinson, Kett01, Kett04, Mahmud02, Poli]. Filled symbols correspond to the $\pi h_{11/2}$ states, while open symbols represent the $\pi s_{1/2}$ states and the error bars are smaller than the size of the plotted symbols. Solid lines connect values for the same odd-proton configuration in a given isotopic chain.

6.2 Results

The first observation of the α decay of ^{159}Re is presented, along with the proton decay properties of the state in ^{155}Ta that this populates. These new measurements benefit from the fast direct correlations between these short-lived decays and are compared with the systematic behaviour of nuclei in this region. Possi-

bilities for the origin of the peak previously assigned as the proton decay of ^{155}Ta are explored.

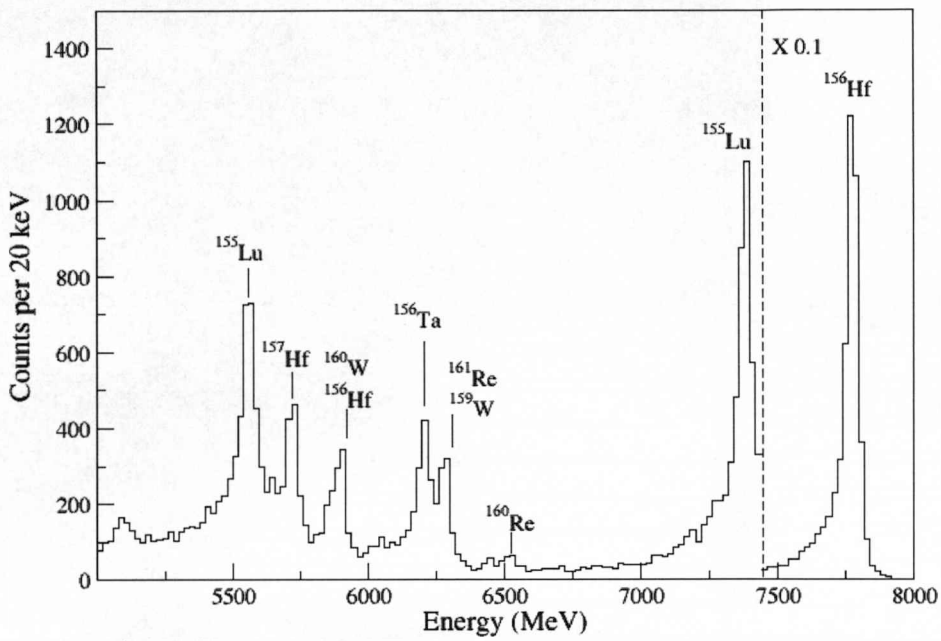

Figure 6.5: Energy spectrum of all decays occurring within 100 μs of the implantation of an evaporation residue in the same DSSD pixel. Known α-decay lines are labeled.

The experiment was performed at the Accelerator Laboratory of the University of Jyväskylä with the RITU + GREAT setup. The ^{159}Re nuclei were populated in the ^{106}Cd(^{58}Ni,p4n) complete fusion evaporation reaction. A beam of 300 MeV ^{58}Ni ions bombarded a 1.1 mg/cm^2 thick, self-supporting ^{106}Cd target foil of 96.5 % isotopic enrichment. The average beam current of 4.7 pnA was delivered over a period of 75 hours. The average recoil implantation rate was $\sim$2 kHz.

In the recent report of the discovery of ^{159}Re by Joss *et al.* [DJoss06], no

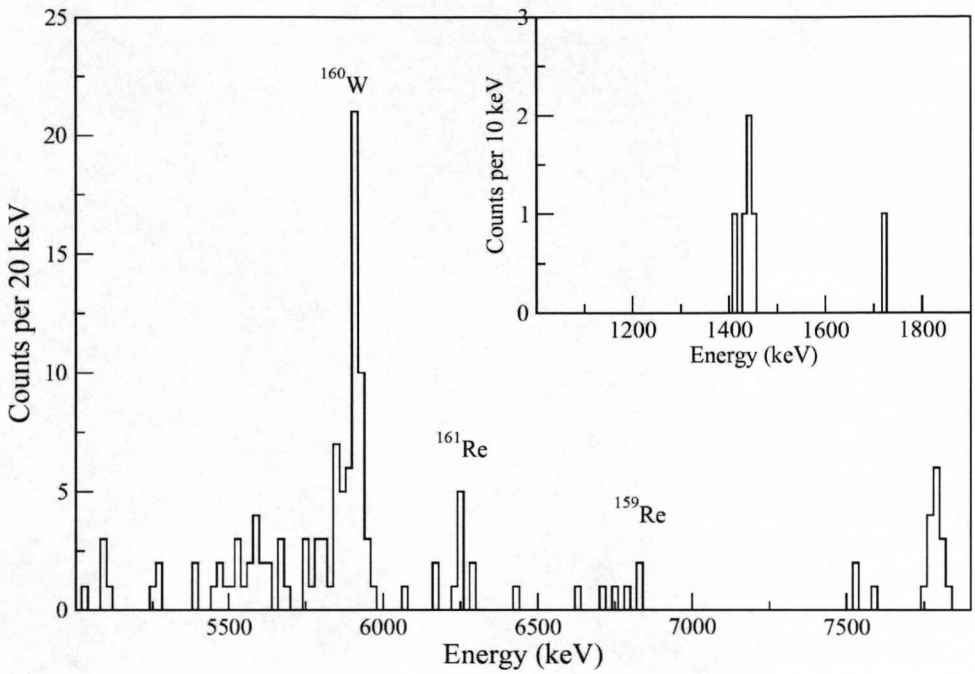

Figure 6.6: Decays as in 6.5 that were followed within 10 ms by a signal in the energy range 1.1-1.8 MeV, corresponding to possible proton decays of ^{155}Ta. The counts at ~6.8 MeV represent a new activity that is assigned as the α decay branch from the $\pi 11/2$ state in ^{159}Re. The inset shows the energy spectrum of decays occurring within 10 ms of events in the ^{159}Re α-decay peak. The peak at ~1.4 MeV is assigned as the proton decay of the lowest-lying $\pi 11/2$ state in ^{155}Ta.

evidence could be found for α decays of ^{159}Re correlated with proton decays of ^{155}Ta having the previously published properties [Uusi99]. However, given the questions surrounding those ^{155}Ta data, the present data were searched for any evidence of an α-decay branch from ^{159}Re followed by proton decays of ^{155}Ta with much less restricted proton energy and correlation time constraints. The measured half-life of the $\pi h_{11/2}$ state in ^{159}Re is 21 $\pm$ 4 μs, so any α-decay branch from this state should be observed with the same half-life. Fig. 6.5 shows

the energy spectrum of all decays occurring within 100 μs of the implantation of an evaporation residue into the same GREAT DSSD pixel. This spectrum is dominated by the 7.8 MeV α decay of the 0.5 ms 8^+ isomer in ^{156}Hf [Page96]. Fig. 6.6 shows the decays from Fig. 6.5 that were then followed within 10 ms by a signal in the energy range 1.1 - 1.8 MeV, which would correspond to possible proton decays of ^{155}Ta. Known α-decay lines below 6.5 MeV appear because the broad energy gate for the proton decays encompasses part of the energy spectrum of α particles that deposit only part of their energy as they escape from the DSSD in the backward direction (see Fig.2 of ref. [DJoss06]). These α-decay lines then appear through correlations with their escaping daughter α decays. The ^{156}Hf peak can be understood as arising when a ^{156}Hf ion is implanted and decays shortly before an uncorrelated escaping α decay of a longer-lived nuclide occurs in the same DSSD pixel. The occurrence of this small number of random correlations reflects the large number of counts in the ^{156}Hf peak in Fig. 6.5. Reducing this proton decay time gate from 10 ms to 100 μs results in an empty spectrum, confirming that there is no evidence in these data for α decays of ^{159}Re correlated with the 1776 keV, 12 μs proton activity reported in ref. [Uusi99].

The counts at 6776 $\pm$ 26 keV represent a new activity, the half-life of which was measured to be 16 $\pm$ 9 μs using the method of maximum likelihood [Schmidt84]. This half-life is an order of magnitude too short to result from a nucleus produced in this fusion reaction decaying by α emission alone, but is consistent with the value measured for the proton decay of ^{159}Re [DJoss06]. It is therefore assigned as the α-decay branch of the $\pi h_{11/2}$ state in ^{159}Re. The α-decay branching ratio measured for this state was 7.5 $\pm$ 3.5 %.

The inset to Fig. 6.6 shows the energy spectrum of events that followed the ^{159}Re α decays within 10 ms. The peak at 1444 $\pm$ 15 keV is assigned as the proton decay of ^{155}Ta. Combining the α-decay Q-value for ^{159}Re with that for this proton decay of ^{155}Ta yields a total of 8405 $\pm$ 30 keV. This compares with the

total of 8428 $\pm$ 20 keV obtained by summing the Q-values for ^{159}Re proton-decay [DJoss06] and ^{158}W α decay [Mahmud]. These values are mutually consistent, which supports the interpretation that the new correlated activities start from the $\pi h_{11/2}$ state in ^{159}Re and end at the ground state of ^{154}Hf (see Fig. 6.2). The half-life of this new proton decay line was measured to be $2.9^{+1.5}_{-1.1}$ ms using the method of maximum likelihood [Schmidt84]. The single count at 1725 keV occurs over 2 ms after the first decay, so it is incompatible with the 12 μs activity assigned as ^{155}Ta in the previous study. Furthermore it is inconsistent with the sum of the Q values and is therefore presumed to be background.

6.2.1 Systematic

The Q-value for the α-decay of ^{159}Re measured in the present work is included in the data presented in Fig. 6.4. It fits in well with the systematics, showing the slightly larger increase in Q-value that is observed at N = 84 for the isotones ^{155}Lu and ^{157}Ta. From the decay energy and branching ratio measured in the present work and the half-life deduced from the ^{159}Re proton decays [DJoss06], a reduced width of $\delta^2 = 81 \pm 44$ keV is deduced using the method of Rasmussen [Ras59]. This agrees well with values measured for decays of nuclei in this region, although the uncertainty is large owing to the small number of counts.

The measurement of an α-decay branch from ^{159}Re allows the partial half-life for proton emission from this state to be determined. Correcting for the branching ratio gives a partial proton decay half-life of 23 $\pm$ 6 μs and the revised spectroscopic factor after allowing for the α-decay branch is 0.41 $\pm$ 0.15. This compares with the expected value of 0.44 for a Re proton emitter [Dav97] and does not alter substantially the conclusions drawn in ref. [DJoss06] about the proton being emitted from a $\pi h_{11/2}$ orbital.

The half-life measured for the ^{155}Ta proton decay in the present work is much

shorter than the value of ~330 ms predicted for its β decay [MNK], so this β-decay branch is expected to have a negligible effect on the partial half-life for proton decay. The measured half-life can be compared with values calculated for the different possible proton orbitals and the measured ^{155}Ta proton decay energy. Using the WKB approximation with the potential of Becchetti and Greenlees [BG] yields calculated values of 91 ns, 0.78 μs and 1.8 ms for the $s_{1/2}$, $d_{3/2}$ and $h_{11/2}$ proton orbitals, respectively. The measured value is only compatible with that calculated for the $\pi h_{11/2}$ orbital. Furthermore, the present measurements for both ^{155}Ta and ^{159}Re agree well with the systematics of proton emission for nuclei with $Z > 68$, provided the protons are emitted from $h_{11/2}$ orbitals [Delion]. From the ratio of the calculated and the measured half-life, a spectroscopic factor of $0.63^{+0.38}_{-0.31}$ can be deduced. This compares with the value of 0.55 expected from a low-seniority shell model calculation for a tantalum isotope [Dav97]. Similar conclusions are reached from calculations performed using either the WKB approximation or a two potential method [Gurvitz] with a potential generated by the Hartree-Fock approach with the SkP Skyrme force [skp].

The proton separation energy deduced for ^{155}Ta in the present work is included in the data plotted in Fig. 6.1. The new value fits in very well with the systematic trends, continuing the expected monotonic decrease in S_p-values with decreasing neutron number. This agreement is also evident in Fig. 6.3, where the new result is seen to follow the smoothly varying behavior established for other nuclides in this vicinity. This is a strong indication that the proton peak observed in the present work represents the decay of the lowest-lying $\pi h_{11/2}$ state in ^{155}Ta. The origin of the previously published results for ^{155}Ta [Uusi99] is an interesting question. Joss *et al.* suggested the possibility that it could represent the decay of an isomeric state in ^{155}Ta [DJoss06]. In the lighter N = 82 isotones, seniority 3 $(\pi h_{11/2})^3$ $27/2^-$ isomers have been identified in the odd-Z nuclides ^{149}Ho, ^{151}Tm and ^{153}Lu [Hel82, McNei89, McNei93]. The corresponding isomer in ^{155}Ta could

be populated directly in the fusion reaction employed in ref. [Uusi99], but would not have been fed by the α decay of ^{159}Re in the present work. The proton decay of the isomer could decay directly to the seniority 2 $(\pi h_{11/2})^2$ 10^+ isomer in ^{154}Hf [McNei89, McNei93] in order to avoid the hindrance due to configuration changes by decaying directly to the ^{154}Hf ground state. However, a more likely decay path is to the 8^+ state in ^{154}Hf, since this would be favored by a higher Q-value than the decay to the 10^+ state.

Fig. 6.7a shows the excitation energies of the $27/2^-$ isomers and 8^+ states observed in N = 82 isotones plotted as a function of atomic number. The excitation energies appear to follow a parabolic trend for both the odd-Z and the even-Z isotones and a parabolic fit allows the excitation energy of the $27/2^-$ state in ^{155}Ta to be estimated. The $27/2^-$ states in $^{149}_{67}$Ho, $^{151}_{69}$Tm and $^{153}_{71}$Lu lie lower in energy than the 8^+ states in $^{148}_{66}$Dy, $^{150}_{68}$Er and $^{152}_{70}$Yb, which would be the respective daughters of their proton decays. Consequently, the proton decay Q-values of these isomeric states to the 8^+ states are lower than those of the $11/2^-$ states to the ground states. Fig. 6.7b shows this reduction in the proton decay Q-value plotted as a function of atomic number of the putative proton emitter. In the case of ^{155}Ta, the estimated Q-value is comparable with that of the lowest-lying $\pi h_{11/2}$ state and would clearly be incompatible with a value $\sim$300 keV larger. Furthermore, the known isomers all have very short half-lives ($\sim 35\mu$s, or less), so it would be surprising if an isomer with such an increased excitation energy were not to decay predominantly by γ-ray emission.

Shell model calculations have been performed by Lawson [Lawson] for the N = 82 isotones, assuming that excited states are formed by the coupling of the valence $h_{11/2}$ protons. Although these calculations achieve remarkable agreement with the measured properties of these isomeric states, they give no indication that other isomers with sufficiently long lifetimes should be expected. Since the proton emission previously reported for ^{155}Ta is purportedly from a $\pi h_{11/2}$ orbital,

it is therefore difficult to see how emission from an isomeric state can provide the explanation of those results.

In summary, new experimental results for the proton decay of ^{155}Ta have been obtained. The ^{155}Ta nuclei were populated through the newly discovered α decay of ^{159}Re and these short-lived radioactivities have allowed clean correlations to be obtained. The measured decay properties are compatible with the decays of $\pi h_{11/2}$ states in both nuclides and provide excellent agreement with the systematic behavior of nuclei in this region. However, they disagree with the previously reported decay properties of ^{155}Ta. Verifying or discounting those experimental results by improving on the background conditions would be a challenging but very important measurement. While the difficulties of such experiments are amply illustrated by the case of ^{155}Ta, it does appear that the smooth evolution of nuclear properties can still provide valuable guidance for future investigations into nuclear properties at this proton-rich extreme of isospin.

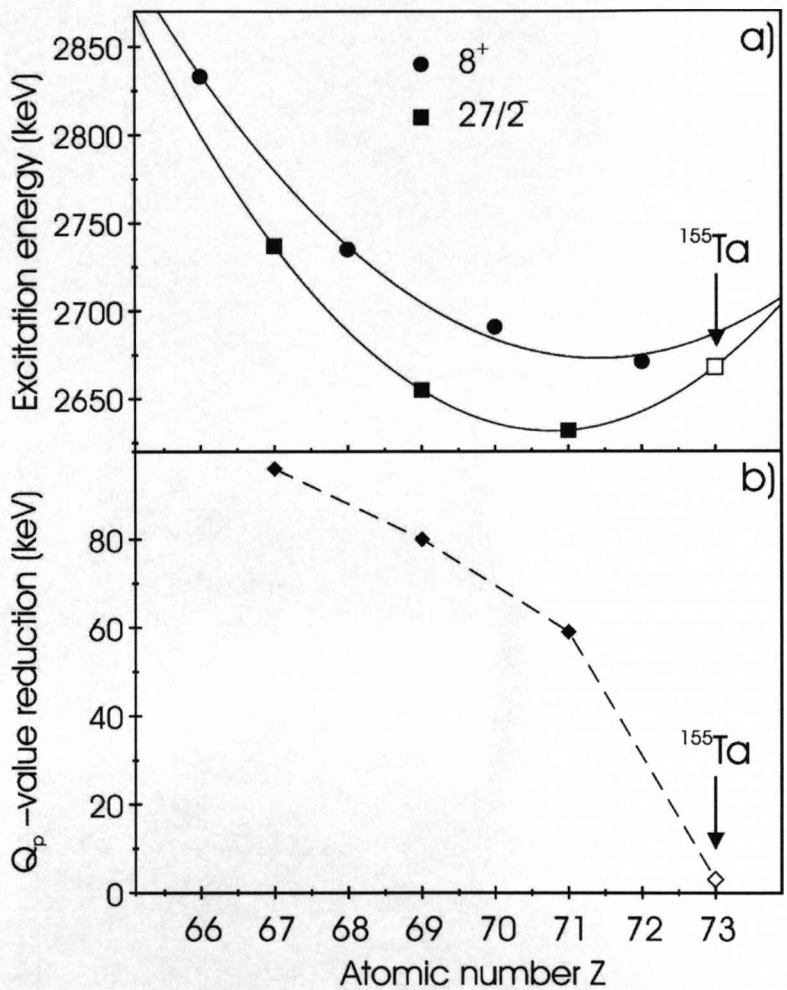

Figure 6.7: (a)Excitation energies of $27/2^-$ isomers and 8^+ states observed in N = 82 isotones plotted as a function of atomic number. Parabolic fits to the measured excitation energies are shown by the solid lines. Data are taken from Refs.[Hel82, McNei89, McNei93]. (b) Reduction in Q-values for proton emission from the $27/2^-$ isomers to the 8^+ states, relative to those for the lowest-lying $\pi h^{11/2}$ states to the ground states, plotted against the atomic number of the potential proton emitter. Expected values for ^{155}Ta are indicated.

Chapter 7

Alpha-decay branching ratios measurement

7.1 Introduction

The techniques of charged-particle and γ-ray tagging at the focal plane of recoil separators has been extensively used to identify nuclei emitting prompt γ rays at the target position in fusion reactions [EPaul95, Cullen98]. A large body of data has been accumulated in such experiments that can, in principle, be used to extract precise measurements of radioactive-decay properties of the nuclei produced, although there is often interference from decays of other nuclei having similar energies and half-lives. It is obviously possible to alter the beam energy or the reaction to study a specific nuclide under optimal conditions, but this is usually not desirable when the primary aim of an experiment is a recoil-decay tagging measurement of a different nuclide. Even so, improved decay-energy and half-life measurements have been reported for a wide range of nuclei from such data sets through correlations with daughter activities to isolate individual decay chains and measure their properties. However, in the case of α-branching ratio measurements it can be difficult to determine reliably the number of first gener-

ation parent nuclei present when there is interference because correlations with daughter decays cannot be used. Branching ratios are important for determining reduced α-decay widths [Ras59], which can give an insight into the structure of the nuclei involved.

We have applied a complementary method (i.e., "inverse tagging") in which γ rays measured at the target position have been used to provide an additional selection criterion in order to reduce background from interfering α decays. The present work extends that of Joss *et al.* [Joss01] and Hadinia *et al.* [Hadinia], who used γ-ray tagging for the purposes of identifying the α-decay lines.

7.2 α-decay branching ratios of $^{164-165-166}$Os

In order to compare our results for ^{161}Os with those of heavier osmium isotopes we sought an improved α-decay branching ratio for ^{165}Os, which had previously been measured to be 100 $\pm$ 40 % [Hof81]. The error in the branching ratio leads to a 40% error in the α-reduced width, which is not ideal considering that the data were used to extract a trend in the systematics of reduced widths of Os isotopes.

The experiment was performed at the Accelerator Laboratory of the University of Jyväskylä. The $^{168-170}$Pt nuclei were produced in reactions induced by 336 MeV and 348 MeV ^{78}Kr ions bombarding 565 μg/cm^2 thick self-supporting ^{92}Mo and ^{94}Mo target foils of 97.3 % and 97.0 % isotopic enrichment, respectively. The 336 MeV beam was delivered with an average beam current of 7 pnA over a period of 149 hours with the ^{92}Mo target and 1 hour with the ^{94}Mo target, while the 348 MeV beam was delivered with an average beam current of 6 pnA with the ^{94}Mo target for a period of 48 hours. The energies of prompt γ rays emitted during the de-excitation of reaction products were measured at the target position using the JUROGAM γ-ray spectrometer consisting of 43 EUROGAM-type escape-suppressed

spectrometers [Beaus92]. The total photopeak efficiency of the JUROGAM array was measured to be 4.2 % at 1.3 MeV. The measured γ-ray energies were used as a tag to select the Pt nuclei of interest in order to measure the daughter Os isotope α-branching ratios. The only previously reported α-branching ratio measurement

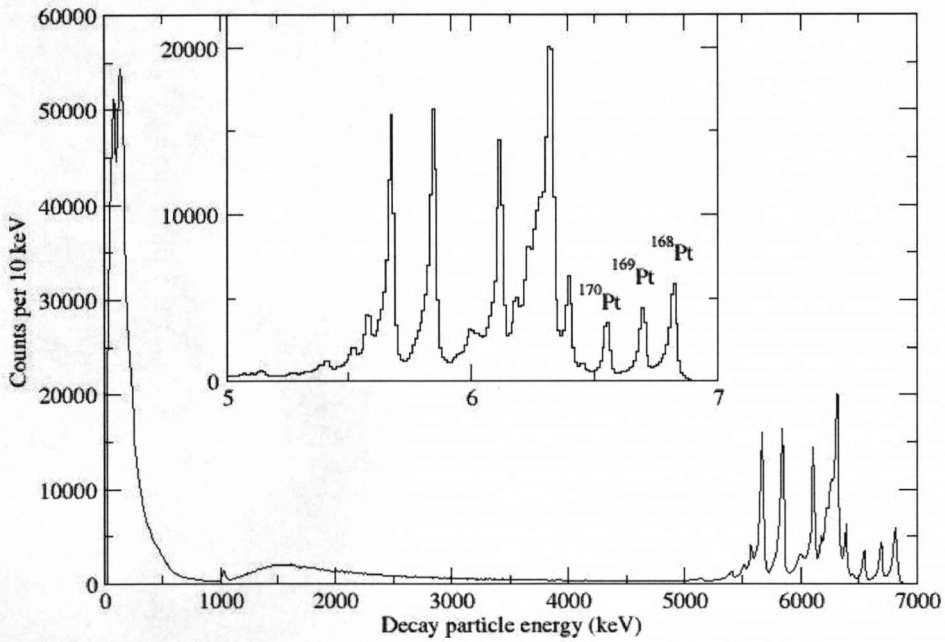

Figure 7.1: Energy spectrum of all decays occurring within 15 ms of an ion implantation into the same DSSD pixel in the reactions of ^{78}Kr with ^{92,94}Mo. The inset shows the region of this spectrum around the α-decay peaks. The $^{168-170}$Pt peaks are labelled. The continuum extending down to ~1 MeV arises from α particles that escape from the DSSD without depositing their full energy. A proton decay peak is just visible above 1 MeV. Below this, the spectrum is dominated by β particles.

for ^{165}Os is 100 $\pm$ 40 % [Hof81]. The beam energy of 348 MeV was optimised for producing ^{169}Pt while strongly suppressing the production of ^{168}Pt. These data

are in contrast to the more typical situation of the data obtained at 336 MeV (see below), in which ^{168}Pt acted as a significant source of interference for the ^{169}Pt α-decay peak. The standard method for calculating α-branching ratios was applied to the 348 MeV data by determining the fraction of events in this ^{169}Pt α-decay peak that are followed by the ^{165}Os daughter α decays, correcting for the time correlation period. The resulting α-branching ratio of 90 $\pm$ 2 % provides a precise value for comparison with that deduced using our new method, allowing its validity to be tested.

Fig. 7.1 shows the energy spectrum of all decays observed in the DSSDs within a time interval of 15 ms following the implantation of a recoil into the same DSSD pixel. When measuring branching ratios using the standard approach from these data, a major source of uncertainty would arise from the low-energy tails of higher-energy peaks extending into the energy gates, which can be seen more clearly in the insert to Fig. 7.1. The similar half-lives of these Pt isotopes gives only limited scope for reducing this uncertainty through a suitable choice of time intervals. The γ rays measured using JUROGAM can provide additional selection of the Pt nuclei of interest, allowing this problem to be circumvented. Fig. 7.2 shows the energy spectrum of γ rays detected in coincidence with a recoil that was followed within 15 ms by a decay of any energy, i.e., any recoil associated with the decays shown in Fig. 7.1. The strongest γ-ray transitions for the isotopes $^{168-170}$Pt have already been identified using the recoil decay tagging method [Joss06, King98]. As an example, the case of ^{169}Pt is presented, which has its strongest γ-ray transition at an energy of 545 keV.

In order to check that a γ ray belongs to the right isotope a two-dimensional matrix was created: each time that an α decay was detected within 15 ms from a recoil in the same DSSD strip, the γ ray in coincidence with that recoil was incremented on one axis in an E_α-E_γ matrix, see Fig. 7.3. By selecting around an α peak and projecting on the γ axis is possible to separate nuclei that have

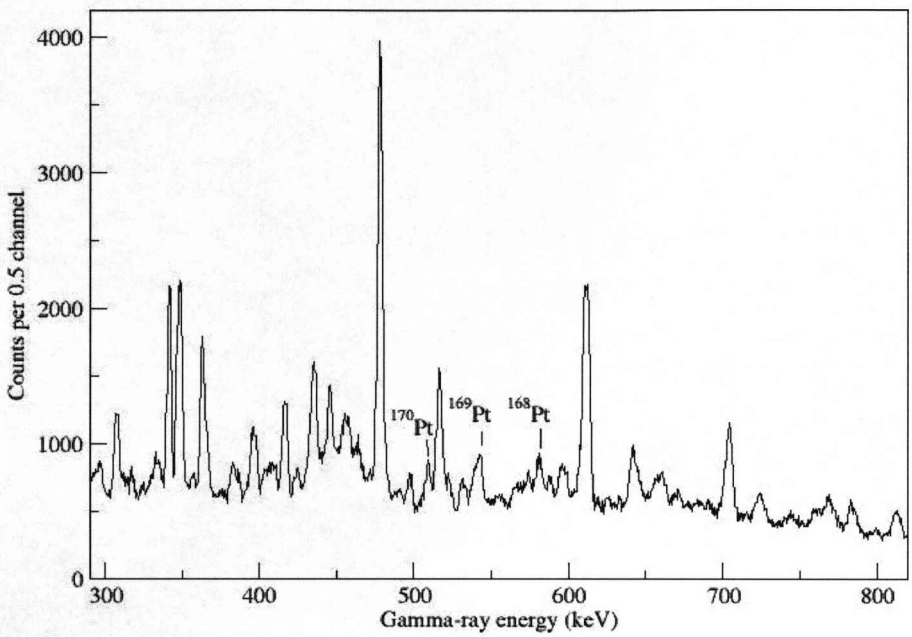

Figure 7.2: Energy spectrum of γ rays detected in coincidence with recoils that are followed within 15 ms by a decay signal in the same DSSD pixel. The energies of the strongest transitions in ^{168,169,170}Pt are indicated. The most intense γ-ray peaks in this spectrum belong to $^{167-169}$Os [Joss01, Joss02]

similar γ-ray transitions. This happens in the case of ^{167}Os, which has one of its stongest γ-ray transitions at 543 keV ([Joss01]) which is very close to the 545 keV γ-ray transition of ^{169}Pt.

Fig. 7.4 shows γ-rays in coincidence with a recoil which is followed within 15 ms by a decay in the energy range of ^{169}Pt α. The inset of Fig. 7.4 shows the strongest peak at 545 keV that was used as a selection criterion to identify ^{169}Pt.

Fig. 7.5 shows the energy spectrum of α decays obtained by applying the same conditions as for Fig. 7.1 plus the additional condition that a γ ray in the energy

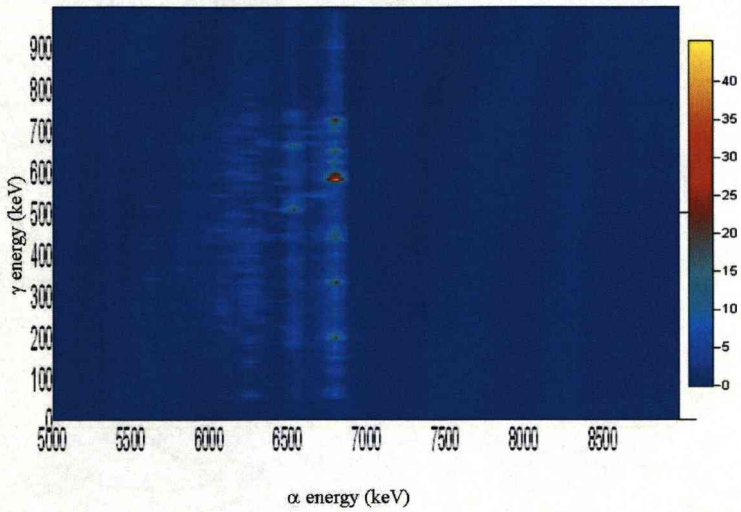

Figure 7.3: Two dimentional matrix showing E_α-E_γ with the requirement that the recoil is followed within 15 ms by a decay in the same DSSD pixel.

range 539 – 553 keV is measured in JUROGAM in association with the implanted ion. It is clear from a comparison of Figs. 7.1 and 7.5 that although the γ-ray gate leads to a significant reduction in statistics, the ^{169}Pt peak is much cleaner. This allowed the number of ^{169}Pt nuclei to be determined with greater accuracy. The peak corresponding to the α decay of ^{167}Os is also enhanced in this spectrum, having a 543 keV γ ray as one of its strongest transitions which also falls within the applied energy gate [Joss01].

Fig. 7.6 shows the spectrum of ^{165}Os decays following within 250 ms the ^{169}Pt α decays selected from the full energy peak in Fig. 7.5. The ^{165}Os α-decay peak at 6.2 MeV is clearly visible [Page96], with a continuum extending to lower energy arising from escaping α particles. The counts below 1 MeV are assigned as β decays of ^{165}Os. Note that it was not possible to use the number of these β particles to extract a reliable branching ratio because the efficiency for β-particle detection is not well known.

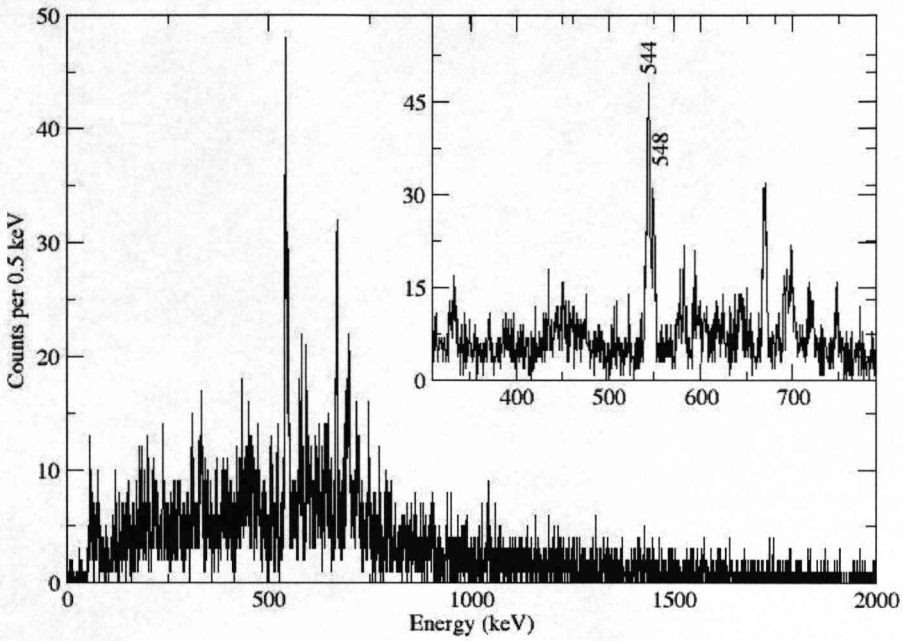

Figure 7.4: γ-ray energy spectrum in prompt coincidence with a recoils that are followed within 15 ms by a decay signal in the same DSSD pixel. The inset shows the region of this spectrum around the γ-decay used to select the ^{169}Pt peak.

7.3 Results

The α-decay branching ratio of ^{165}Os deduced from the fraction of ^{169}Pt α decays that are followed by a ^{165}Os α decay is presented in Table 7.1, together with corresponding values for ^{164,166}Os deduced in this work using the same method. The resulting branching ratios for $^{164-165-166}$Os agree with the literature values but have improved precision.

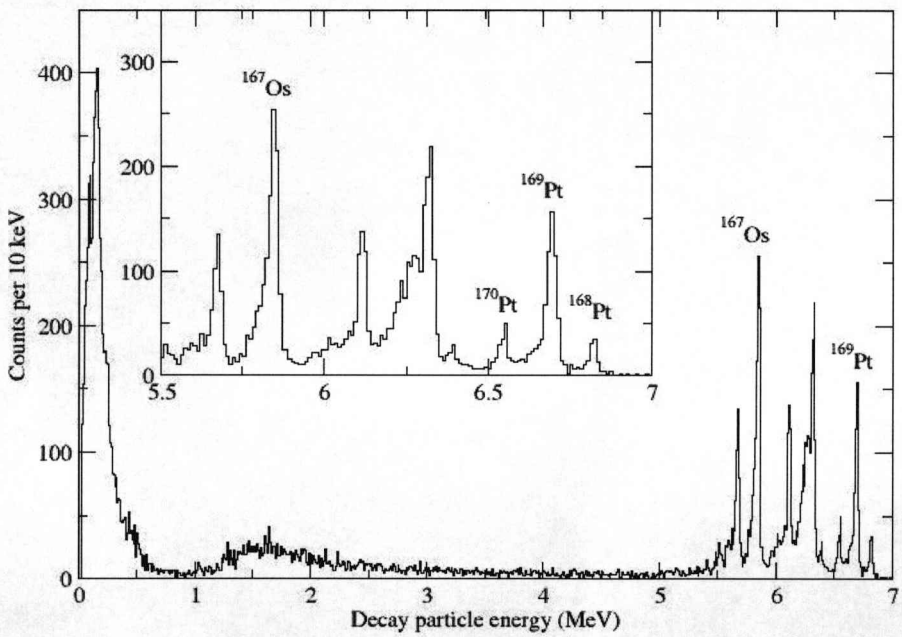

Figure 7.5: As 7.1, but with the additional requirement that the ion is measured in prompt coincidence with a 545 keV γ ray observed in the JUROGAM array. This γ-ray energy corresponds to a known strong transition assigned to ^{169}Pt [Joss06].

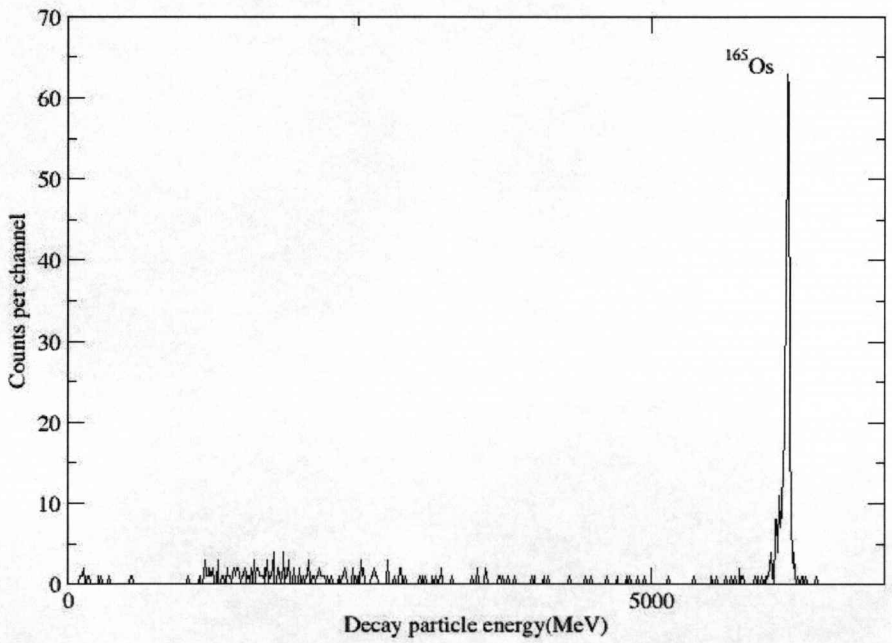

Figure 7.6: Energy spectrum of ^{165}Os decays following α decays in the ^{169}Pt peak in 7.5 within 250 ms.

nuclide	γ-ray gate	branching ratio	literature value	δ^2(keV)
^{164}Os	575 – 587 keV	96 ± 5 %	~95 % [Bing96]	86 ± 7
^{165}Os	539 – 553 keV	88 ± 5 %	100 ± 40 % [Hof81]	79 ± 4
^{166}Os	503 – 513 keV	84 ± 4 %	72 ± 13 % [Page96]	121 ± 8

Table 7.1: Alpha-decay branching ratios deduced for $^{164-166}$Os compared with literature values. The γ-ray energy gates applied in the present work to select the parent Pt α emitters and the reduced α-decay widths calculated using the method of Rasmussen [Ras59] are also given. The reduced width for ^{165}Os was calculated using the α-decay branching ratio of 90 ± 2 % deduced from the 348 MeV data.

Chapter 8

Summary and Future Prospects

8.1 Summary

In the past 20 years many studies have been performed in the region of proton radioactivity in between Z = 50 and Z = 82 shell closures. In this work several measurements allow new limits to nuclear boundaries to be established. In particular the discovery of ^{161}Os marks it among the most distant known from the line of maximum nuclear β stability. Through a complementary set of measurements presented in this work it has been shown that a $\nu f_{7/2}$ state forms its ground state, even though interactions between the $h_{9/2}$ neutrons and $h_{11/2}$ protons could be expected to come close to inverting the order of the neutron orbitals. In an attempt to explain this, Hartree-Fock calculations of the energy difference between $\nu h_{9/2}$ and $\nu f_{7/2}$ orbitals for N = 82 isotones using three commonly used Skyrme parameterisations were performed with the addition to each of these Skyrme forces of a tensor term. The agreement between experimental values and the calculations with the tensor component indicate that this inter-nucleon force should be taken into account for nuclei in this mass region near the proton drip line.

To compare our results for ^{161}Os with those of heavier osmium isotopes improved α-decay branching ratio for Os isotopes were needed. An experiment was per-

formed at JYFL during which prompt γ rays were detected at the target position and provided a selection criterion for the $^{168-170}$Pt nuclei. This technique enabled the problem of the background from higher-energy α decays in the spectrum to be circumvented. The resulting branching ratios for $^{164-165-166}$Os agree with the literature values but have improved precision. New experimental results for the proton decay of ^{155}Ta have been obtained in the present work. The ^{155}Ta nuclei were populated through the α decay of ^{159}Re discovered in this work and these short-lived radioactivities have allowed clean correlations to be obtained. The measured decay properties are compatible with the decays of $\pi h_{11/2}$ states in both nuclides and provide excellent agreement with the systematic behaviour of nuclei in this region.

8.2 Future Prospects

For the future, there appears to be every prospect of observing the α decays of what is expected to be the lightest α-emitting osmium isotope, ^{160}Os. During the analysis of these data no evidence for the ^{160}Os α decays could be found, but a dedicate experiment at the optimum beam energy might have a better chance of observing it. The ^{160}Os α decays would populate the ground state of ^{156}W, which would in turn β decay, mainly feeding the ground state of ^{156}Ta. The half-life of ^{156}W could then be deduced from the time differences between the ^{160}Os α decays and the ^{156}Ta proton decays, in an analogous way to that used in the present work in Chapter 5 to measure the half-life of ^{157}W. The case of ^{160}Os is particularly interesting because of the possibility of observing α decays from both the ground state and the excited $[\nu f_{7/2} h_{9/2}]8^+$ state, as seen in its lighter isotones [Page96]. This would allow the excitation energy of the 8^+ state to be deduced, providing further insight into the interactions between the $h_{9/2}$ neutrons and $h_{11/2}$ protons. Figure 8.1 shows the excitation energy of 8^+ states in the even-Z isotones from

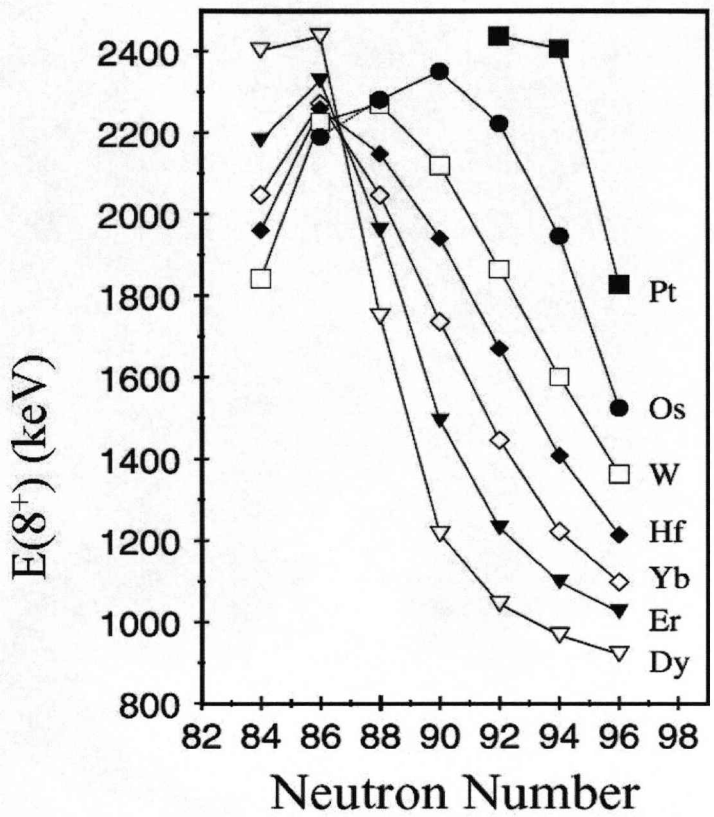

Figure 8.1: The 8^+ state excitation energy in the even-even isotones from $_{66}$Dy to $_{78}$Pt, taken from [Joss05].

$_{66}$Dy to $_{78}$Pt as a function of neutron number. For $N \geq 88$ the 8^+ state is found to exhibit lower excitation energies for lower-Z nuclei. At $N \leq 86$, an inversion in the trend occurs and the 8^+ excitation energy gets higher for the lower-Z isotones. Again the inversion has been interpreted (see ref. [Zhang]) as being caused by a lowering of the $h_{9/2}$ neutron state due to an increasingly attractive interaction between the $h_{11/2}$ proton and $h_{9/2}$ neutron states as more protons are added in the $h_{11/2}$ state.

The nucleus ^{158}Re could also represent a step further for the investigations performed in this work. From the trend in the systematic of proton separation energy

shown in fig.6.1 an increase of $\sim$ 500keV in energy for ^{158}Re compared to ^{159}Re could be expected. Joss *et al.* in ref. [DJoss06] compared the measured half-life for the proton decay of ^{159}Re with the result of WKB calculations for different possible proton orbitals and the half-life of the expected $\pi d_{3/2}$ ground state of ^{158}Re is expected to be only $\sim$10 ns. It is suggested that if there were a proton-emitting $\pi h_{11/2}$ state in ^{158}Re, the effect of the angular momentum barrier may be sufficient to increase the half-life to $\sim \mu$s in spite of the increase in decay energy. It is clear that this would be an extremely challenging experiment because the production rate would be even lower than that for ^{159}Re.

To push further the limit of knowledge of nuclear structure new detectors and methods need to be introduced. A detection system for charged particles to address this issue, the Light Ion Spectrometer Array (LISA) has been developed and will be installed at the target position of the RITU separator, see fig. 8.3. Charged particle emission dominates in this region, therefore LISA is intended to

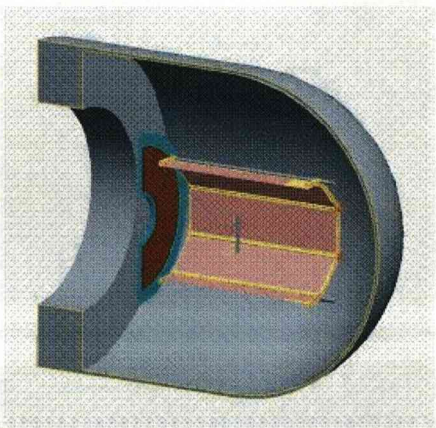

Figure 8.2: Schematic of the LISA spectrometer inside the target chamber in front of RITU. The hexagonal barrel shape and an anular detector perpendicular to the beam axis are shown.

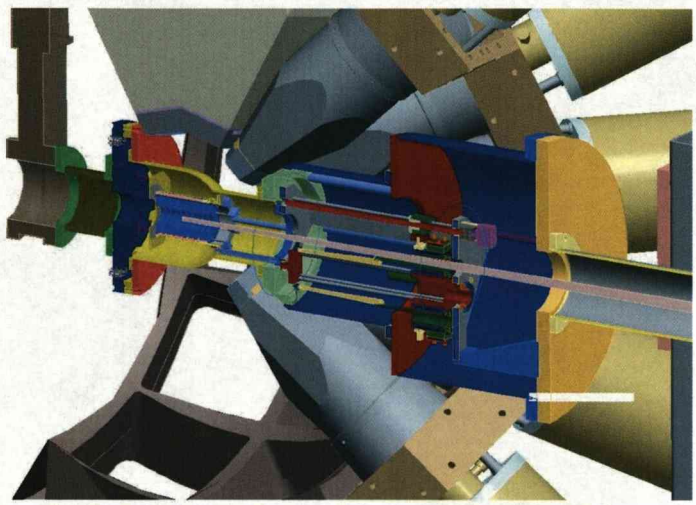

Figure 8.3: Schematic view of the area around the target at JYFL including the LISA detector.

measure the energies of protons and α particles at the target position of RITU. LISA will also be able to measure low-energy (<4 MeV) protons with good enough resolution in order to act as a spectrometer to measure the energies of very fast proton decays ($t_{1/2}$<ns) and the barrel shape (see Fig.8.2) of the detector will allow in-flight lifetime measurements for fast proton decays. LISA will be used in conjunction with GREAT and JUROGAM to study fast proton emission from a range of nuclei beyond the proton drip line. This will allow our knowledge of the limits of nuclear existence to be pushed even further from the line of maximum β stability.

Bibliography

[And04] A. N. Andreyev *et al.*, Nucl. Instrum. Methods Phys. Res. A **533**, 422 (2004).

[Bart82] J. Bartel *et al.*, Nucl. Phys. A **386**, 79 (1982).

[Batchelder] J.C. Batchelder *et al.*, Phys. Rev. C **57**, R1042 (1998).

[Beaus92] C.W. Beausang *et al.*, Nucl. Instrum. Meth. Phys. Res. A **313**, 37 (1992).

[BG] F.D. Becchetti and G.W. Greenlees, Phys. Rev. **182**, 1190 (1969).

[Bing96] C.R. Bingham *et al.*, Phys. Rev. C **54**, R20 (1996).

[Beau92] C.W. Beausang *et al.*, Nucl. Instrum. Meth.Phys. Res. A **313**, 37 (1992).

[Bingam] C.R. Bingham *et al.*, Phys. Rev. C **59**, R2984 (1999).

[Bla08] B. Blank, M.J.G. Borge, Progress in Particle and Nuclear Physics **60**, 403 (2008).

[Bohr40] N. Bohr, Physical Review **58**, 654 (1940)

[Bonn07] L. Bonneau *et al.*,Phys. Rev. C **76**, 024320 (2007).

[Cast00] R.F. Casten, "'Nuclear Structure from a simple perspective"',Oxford University Press Inc. (2000).

[Chab98] E. Chabanat *et al.*, Nucl. Phys. A **635**, 231 (1998).

[Col07] G. Coló *et al.*, Phys. Lett. B **646**, 227 (2007).

[Cond28] E. U. Condon and R. W. Gurney, Nature **122**, 439 (1928).

[Cullen98] D.M. Cullen *et al.*, Phys. Rev. C **58**, (1998) 846.

[Dav92] C.N. Davids *et al.*, Nucl. Instrum. Methods Phys. Res. B **70**, 358 (1992).

[Dav97] C.N. Davids *et al.*, Phys. Rev. C **55**, 2255 (1997).

[Delion] D.S. Delion, R.J. Liotta and R. Wyss, Phys. Rev. Lett. **96**, 072501 (2006).

[Ding] K.Y. Ding *et al.*,Phys. Rev. C **64**, (2001) 034315.

[DJoss06] D.T. Joss *et al.*, Phys. Lett. B **641**, 34 (2006).

[Enge66] H.A. Enge "'Introduction to Nuclear Physics"',Addison-Wesley Reading, 1966.

[EPaul95] E.S. Paul *et al.*, Phys. Rev. C **51**, 78 (1995).

[ESuc] E.B. Suckling and P.D. Stevenson, private comunication.

[Faest] T. Faestermann *et al.*, Phys. Lett. B **137**, 23 (1984).

[Fermi34] E. Fermi, Z. Phys. **88**, 161 (1934).

[Foin82] C. Foin *et al.*, Z. Phys. A **305**, 81 (1982).

[Gall58] C.J. Gallagher, Jr. and S. A. Moszkowski, Phys. Rev. **111**, 5, 1282 (1958).

[Gamow28] G. Gamow, Z. Phys. **51**, 204 (1928).

[Geiger11] H. Geiger and J.M. Nuttal, Phil. Mag. **22**, 613 (1911).

[Ghio88] A. Ghiorso *et al.*, Nucl. Instrum. Meth. Phys. Res. A **269**, 192 (1988).

[Gilli] A. Gillitzer *et al.*, Z. Phys. A **326**, 107 (1987).

[Gint03] T. N. Ginter *et al.*, Phys. Rev. C **68**, 034330 (2003).

[Gold60] V.I. Goldansky, Nucl. Phys. **19**, 482 (1960).

[grain] P. Rahkila, Nucl. Instr. and Meth. A **595**, 637 (2008).

[Gurvitz] S.A. Gurvitz and G. Kalbermann, Phys. Rev. Lett. **59**, 262 (1987).

[Hadinia] B. Hadinia *et al.*, Phys. Rev. C **76**, 044312 (2007).

[Haxel49] O. Haxel, J.H.D. Jensen and H.E. Suess, Phys. Rev. **75**, 1766 (1949).

[Hel82] H. Helppi *et al.*, Phys. Lett. B **115**, 11 (1982).

[Hof79] S. Hofmann *et al.*, Z. Phys. A **291**, 53 (1979).

[Hof81] S. Hofmann *et al.*, Z. Phys. A **299**, 281 (1981).

[Hof89] S. Hofmann et al., Z. Phys. A **333**, 107 (1989).

[Hofmann89] S. Hofmann, Particle Emission From Nuclei (CRC Press, Boca Raton, FL, 1989), Vol. 2, p. 25.

[Igo58] G. Igo Phys. Rev. Lett., 1 (1958) 71.

[Irvine97] R.J. Irvine *et al.*, Phys. Rev. C **55**, R1621 (1997).

[Joss01] D.T. Joss *et al.*, Nucl. Phys. A **689**, 631 (2001).

[Joss02] D.T. Joss *et al.*, Phys. Rev. C **66**, 054311 (2002).

[Joss04] D.T. Joss *et al.*, Phys. Rev. C **70**, 017302 (2004).

[Joss05] D.T. Joss *et al.*, Journal of Phys. G **31**, 1593 (2005).

[Joss06] D.T. Joss *et al.*, Phys. Rev. C **74**, 014302 (2006).

[Kett01] H. Kettunen *et al.*, Acta. Phys. Pol. B **32**, 989 (2001).

[Kett04] H. Kettunen *et al.*, Phys. Rev. C **69**, 054323 (2004).

[King98] S.L. King *et al.*, Phys. Lett. B **443**, 82 (1998).

[King00] S.L. King *et al.*, Phys. Rev. C **62**, 067301 (2000).

[Klein79] P. Kleinheinz *et al.*, Z. Phys. A **290**, 279 (1979).

[KLiv93] K. Livingston *et al.*, Phys. Rev. C **48**, R2151 (1993).

[Kran88] K.S. Krane *Introductory nuclear physics*, Wiley New York 1988.

[lamb40] W.E. Lamb, Physical Review **58**, 696 (1940).

[Lawson] R.D. Lawson, Z. Phys. A **303**, 51 (1981).

[Lei95] M. Leino, Nucl. Instrum. Meth. Phys. Res. B **99**, 653 (1995).

[Lei97] M. Leino, Nucl. Instrum. Meth. Phys. Res. B **126**, 320 (1997).

[Lennard90] W.N. Lennard *et al.*, Nucl. Intrum. Methods. Phys. Res. B **45** 281 (1990).

[Liv93] K. Livingston *et al.*, Phys. Lett. B. **312**, 46 (1993).

[Mah00] H. Mahmud *et al.*, Phys. Rev. C **62**, 057303 (2000).

[Mahmud] H. Mahmud *et al.*, Phys. Rev. C **62**, 057303 (2000).

[Mahmud02] H. Mahmud *et al.*, Eur. Phys. Journal A **15**, 85 (2002).

[Mayer49] M.G. Mayer, Phys. Rev. **75**, 1969 (1949).

[McNei89] J.H. McNeill *et al.* , Phys. Rev. Lett. **63**, 860 (1989).

[McNei89Z] J.H. McNeill *et al.*, Z. Phys. A **332**, 105 (1989).

[McNei93] J.H. McNeill *et al.*, Z. Phys. A **344**, 369 (1993).

[Meyer75] S.L. Meyer, Data Analyis for Scientist and Engineers, Wiley Series in Probability and Mathematical Statistics, John Wiley & Sons, Inc.(1975).

[Meissner] F. Meissner *et al.*, Z. Phys. A **339** 315 (1991).

[MNK] P. Möller *et al.*, Atomic Data and Nuclear Data Tables **66**, 131 (1997).

[Moll95] P. Möller *et al.*, Atomic Data and Nuclear Data Tables **59**, 185 (1995).

[Nord49] L.W. Nordheim, Phys. Rev. **75**, 12(1949).

[Nord50] L.W. Nordheim, Phys. Rev. **78**, 294(1950).

[Ots01] T. Otsuka *et al.*, Phys. Rev. Lett. **87**, 082582 (2001).

[Ots05] T. Otsuka *et al.*, Phys. Rev. Lett. **95**, 232502 (2005).

[Page92] R.D. Page *et al.*, Phys. Rev. Lett. **68**, 1287 (1992).

[Page94] R.D. Page *et al.*, Phys. Rev. Lett. **73**, 3066 (1994).

[Page96] R.D. Page *et al.*, Phys. Rev. C **53** 660 (1996).

[Page03] R.D. Page *et al.*, Nucl. Instrum. Meth. Phys. Res. B **204**, 634 (2003).

[Per57] I. Perlman and J.O. Rasmussen, Alpha Radiactivity, Handbuch der Physik, Band XLII edited by S. Flügge, Springer-Verlag, Berlin- Göttingen-Heidelberg (1957), 109.

[Piip79] M. Piiparinen *et al.*, Z. Phys. A **300**, 133 (1981).

[Piip81] M. Piiparinen *et al.*, Z. Phys. A **290**, 337 (1979).

[Poli] G.L. Poli *et al.*, Phys. Rev. C **59**, R2979 (1999).

[Ras59] J.O. Rasmussen, Physical Review **113** 1593 (1959).

[Ras66] J.O. Rasmussen, Alpha-, Beta- and Gamma-Ray Spectroscopy, Siegbahn, K., Ed., North-Holland, Amsterdam, (1966), 701.

[Robinson] A.P. Robinson *et al.*, Phys. Rev. C **68**, 054301 (2003).

[RPage92] R.D. Page *et al.*, Phys. Rev. Lett. **68** 1287 (1992).

[RPage94] R.D. Page *et al.*, Phys. Rev. Lett. **72**, 1798 (1994).

[Rein95] P.G. Reinhard and H. Flocard, Nucl. Phys. A **584**, 467 (1995).

[Rudolph] D. Rudolph *et al.*, Phys. Rev. Lett. **80**, 3018 (1998).

[Rytz91] A. Rytz, Atomic Data and Nuclear Data Tables **47**, 205 (1991).

[Saad95] A.F. Saad *et al.*, Z. Phys. A **351**, 247 (1995).

[Ship] G.Münzberg *et al.*, Nucl.Inst.Meth **161**, 65 (1979).

[Schmidt00] K.-H. Schmidt *et al.*, Eur. Phys. J. A **8**, 141 (2000).

[Schmidt84] K.-H. Schmidt *et al.*, Z. Phys. A **316** 19 (1984).

[Schrewe] U.J. Schrewe *et al.*, Phys. Rev. C **25** 3091 (1982).

[Sel93] P.J. Sellin*et al.*, Phys. Rev. C **47**, 1933 (1993).

[skp] J. Dobaczewski *et al.*, Nucl. Phys. A **422**, 103 (1984).

[Toth73] K.S. Toth, Phys. Rev. C **7**, 2010 (1973).

[Toth79] K.S. Toth, Phys. Rev. C **19**, 2 (1979).

[Toth83] K.S. Toth, Phys. Rev. C **27**, 889 (1983).

[Urban96] W. Urban, Phys. Rev. C **53**, 5 (1996).

[Urban02] W. Urban, Phys. Rev. C **66**, 044302 (2002).

[Uusi99] J. Uusitalo *et al.* Phys. Rev. C **59**, R2975 (1999).

[Vier88] K.S. Vierinen *et al.*, Phys. Rev. C **38**, R1509 (1988).

[Wei35] C.F.von Weizsäker, Z. Phys., **96**, 431 (1935).

[Woods54] R.D. Woods, D.S. Saxon, Phys. Rev., **95** 577 (1954).

[Woods97] P.J. Woods and C.N. Davids, Ann. Rev. Nucl. Part. Sci. **47**, 541 (1997).

[Woods04] P.J. Woods *et al.*, Phys. Rev. C **69**, 051302(R) (2004).

[Zhang] C.T. Zhang *et al.*, Phys. Rev. C **54**, R1 (1996).